Experimental Study of Ammonia/Hydrogen Non-premixed Flames using Raman spectroscopy

Onifade, Raheem A.

Award date:
2023

Technische Universiteit
Eindhoven
University of Technology

Department of Mechanical Engineering
Power & Flow research group

Masters Graduation Project

Experimental Study of Ammonia/Hydrogen Non-premixed Flames using Raman spectroscopy

Masters thesis

Author:
R.A. Onifade 1313266

Supervisors:
Dr. N.J. Dam
Dr. Ir. N.C.J Maes

Eindhoven, February 9, 2023

This report was made in accordance with the TU/e Code of Scientific Conduct for the Master thesis

Abstract

Scientists and engineers around the world have been doing extensive research on alternative carbon-free fuels that do not produce greenhouse effect gases. One of the few candidates is ammonia as it is a gas that consists of nitrogen and hydrogen. However, ammonia combustion is faced with certain challenges that need to be studied through immense research on its flame structure. To carry out this research, experimental data on the temperature and species concentration of ammonia flames are required. Non-intrusive laser diagnostic techniques are one of the methods used to measure temperature and species concentration in flames.

In this project, a laser diagnostic technique called Raman spectroscopy is employed to acquire experimental data on the temperature and molar fractions of laminar non-premixed ammonia/hydrogen/nitrogen flames. The experimental data are analyzed and errors in the temperature measurements are found to be within ±41 K. On the other hand, the molar fraction measurements are found only be qualitative due to the systematic errors in the calibration of the experimental setup used in this project.

Abbreviations

CCD Charged coupled device. 27, 30–32, 35, 36, 38, 39, 47, 51

CFD Computational fluid dynamics. 27, 65–67

DSLR Digital single-lens reflex. 46, 64

FWHM Full width at half maximum. 25, 26, 41

HVIS Holographic grating for the visible light spectrum. 35

laser Light Amplification by Stimulated Emission of Radiation. 16

LIF Laser-induced Fluorescence. 17, 18, 30, 51

Nd:YLF Neodymium-doped yttrium lithium fluoride. 5, 34, 58, 64

NIST National institute of standards and technology. 7, 40

QE Quantum efficiency. 31

SNR Signal-to-noise ratio. 31, 50, 52

SSAS Solid State Ammonia Synthesis. 9

STP Standard temperature and pressure. 26

Contents

Chapter 1

Introduction

Ammonia is seen as one of the carbon-free fuels that can replace fossil fuels, eventually reducing the amount of CO_2 emissions in the atmosphere. However, the challenges such as low burning velocity, high ignition energy, and high NOx emissions, facing ammonia combustion have made its usage difficult[73, 75, 76]. Although the addition of H_2 to the ammonia/air mixture has been experimentally proven to improve the combustion of ammonia, it also increases the amount of NOx emitted. Hence, a detailed study of NH_3/H_2 flames is necessary for the investigation of the species or products that cause the increase in NOx emissions. The knowledge of temperature across hydrogen-doped ammonia(NH_3) flames is also essential in examining how the production and destruction of major species are dependent on the temperature. As explained in subsequent chapters, the use of the existing mechanisms to numerically predict the concentration of major species and temperature in the flames is mostly qualitative. This is because there are large discrepancies in certain combustion parameters predicted using the mechanisms. Hence, the measurement of the temperature and concentrations of the species in the flames is vital in the improvement of these mechanisms.

The main goal of this project is to obtain and analyze experimental data on the temperature and species concentration of laminar non-premixed NH_3/H_2 flames using a minimally intrusive technique called Raman spectroscopy. The spontaneous Raman scattering of a Nd:YLF laser light (527 nm) is used to obtain the species concentration and temperature profile across the height of $NH_3/H_2/N_2$ diffusion flames. Additionally, how the increase in the concentration of NH_3 and H_2 fuel affects the temperature profiles is examined in this project.

Firstly, the characteristics of ammonia are discussed in chapter 2 to highlight the benefits of using ammonia as a fuel and the challenges facing its combustion process. In addition, a detailed review of NH_3 and NH_3/H_2 flame characteristics and an overview of the existing reaction mechanism models of ammonia combustion are presented in this chapter. Secondly, the principle of laser diagnostics is explained in chapter 3 since Raman spectroscopy is a laser diagnostics technique used to acquire experimental data. Additionally, the concept of Raman spectroscopy is briefly studied in chapter 3. Thirdly, the equations used to describe the Raman scattering process are studied in chapter 4. Then, the experimental setup used in this project is described in chapter 5. Afterward, the data analysis of the acquired experimental data is discussed in chapter 6. Then, the results obtained from the experiments are examined in chapter 7. Finally, outlined in chapter 8 are the conclusions drawn from this project and the recommendations for future research.

Chapter 2

Background of the project

2.1 Properties of ammonia

To understand the benefits of using ammonia as a fuel, its properties such as combustion characteristics, flammability, and corrosiveness need to be investigated. These properties also illustrate the various challenges facing ammonia combustion.

2.1.1 Combustion characteristics of ammonia

As seen in Figure 2.1a, liquid ammonia contains the highest hydrogen density per unit volume among all the hydrogen-based carriers compared in the research by Kojima et al [60]. This means that ammonia can be used as a fuel and as a storage medium for hydrogen-fuel transport. Figure 2.1a also shows that ammonia has a higher volumetric H_2 density than pure liquid hydrogen. This means ammonia requires a reduced amount of space, when compared to liquid hydrogen itself, to transport the same amount of energy, making it a better medium for hydrogen fuel storage and transport.

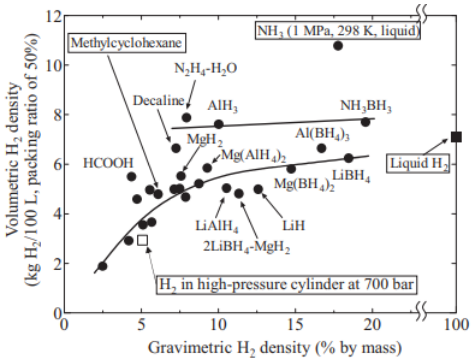

(a) Gravimetric and volumetric H_2 density for several hydrogen carrier [60].

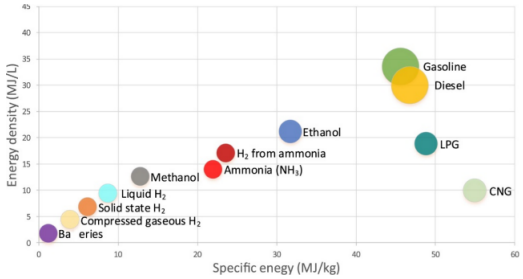

(b) Energy densities of several fuel types [76].

Figure 2.1: Comparison of ammonia to other hydrogen-based carriers and several conventional fuels.

On the other hand, Yapicioglu et al. [76] combined results from energy density measurements done by several researchers [19, 42, 43, 47] to generate the plot in figure 2.1b, including various fossil, and carbon-free fuels. While these conventional fuels are outside of the range of carbon-free fuels, it clearly shows that ammonia is the zero-CO_2 solution that has the highest energy density. However, ammonia combustion may be associated with high NOx emissions, which will be discussed in subsequent sections.

Table 2.1 illustrates a comparison of the combustion characteristics of ammonia, hydrogen, and

conventional hydrocarbons that are compiled from the reviews written by Valera-Medina et al. [72], Kobayashi et al. [75] and Yapicoglu et al. [76] on the current science and technology of ammonia combustion. Additionally, the boiling temperature and condensation pressure are obtained from the NIST database [81] to explain the liquefaction and storage of these fuels. Table 2.1 shows that the condensation pressure of hydrogen at room temperature is significantly higher than that of ammonia, making the liquefaction and storage of hydrogen more expensive [75]. Moreover, the storage equipment for propane can also be used for ammonia since both fuels have approximately equal condensation pressure at room temperature as shown in table 2.1, provided that the storage walls are not susceptible to ammonia corrosion.

Having discussed the benefits of ammonia as a stored fuel, other properties related to its combustion need to be looked at. By inspecting table 2.1, one can see that ammonia has a high minimum auto-ignition temperature and minimum auto-ignition energy. Table 2.1 also shows that the maximum laminar burning velocity of ammonia is significantly lower than those of hydrogen and hydrocarbons. The flammability range of ammonia is narrower than those of the other fuels in table 2.1, signifying that it has low flammability. The effect of these challenges facing ammonia combustion can be reduced by mixing ammonia fuel with other fuels like hydrogen. For example, Koike et al. [50] carried out experimental tests on an engine fueled by a mixture of 60% ammonia with 40% hydrogen. The researchers compared the results to benchmark experiments using regular gasoline. One of their experimental results demonstrated that the corresponding flame of the ammonia/hydrogen mixture became more stable because of an increase in the laminar burning velocity. Moreover, the burning velocity of the ammonia/hydrogen mixture was almost equivalent to that of the gasoline mixture.

fuel type	NH_3	H_2	CH_4	C_3H_8	CH_3OH
Boiling temperature at 1 atm (°C)	-33.4	-253	-161	-42.1	64.7
Condensation pressure (atm) at 25 °C	9.90	244.96	N/A	9.40	1
Lower heating value, LHV (MJ/kg)	18.6	120	50.0	46.4	19.5
Adiabatic flame temperature (°C)	1800	2110	1950	2000	1910
Maximum laminar burning velocity (m/s)	0.07	2.91	0.37	0.43	0.36
Minimum auto-ignition temperature (°C)	650	520	630	450	464
Flammability range (equivalence ratio)	0.63-1.40	0.10-7.1	0.50-1.7	0.51-2.5	-

Table 2.1: Thermal properties and fundamental combustion characteristics of ammonia, hydrogen, and hydrocarbon fuels [72, 75, 76]. The boiling temperature and condensation pressure of the fuels are obtained from the NIST database [81].

2.1.2 Corrosive nature of ammonia

In this project, experiments will be conducted in the Zero Emission Laboratory, which has several engine cells. Materials used for the construction of these test cells and fuel delivery systems need to be carefully selected as ammonia reacts with certain metals like copper, brass, and zinc, producing a greenish/blue chemical compound [72, 76]. Hence, ammonia is corrosive to alloys containing these metals. This means that non-corrosive materials that are compatible with ammonia need to replace these metal alloys to protect engine cells and fuel delivery systems. To that end, Cole-Parmer [66] created a compatibility database that is used to find materials such as stainless steel that are non-corrosive with ammonia, as shown in Table 4 of [72].

2.2 Ammonia synthesis

Ammonia is used for several purposes such as refrigeration agents, fertilizers, and as a raw

chemical material. However, Huang [35] estimates that about 85% of ammonia produced worldwide is used for crop production as a fertilizer. Since food production is an essential part of human society, several large-scale industrial processes have been developed for ammonia production. The two most common processes are shown in figure 2.2. The nitrogen gas needed for both processes is supplied using an air separation unit as shown in figure 2.2. The cryogenic air separation process is mostly used to split the gases that constitute air to obtain nitrogen. This is because it is the most efficient way of acquiring higher amounts (99.99%) of pure oxygen and nitrogen at a low economic cost [25].

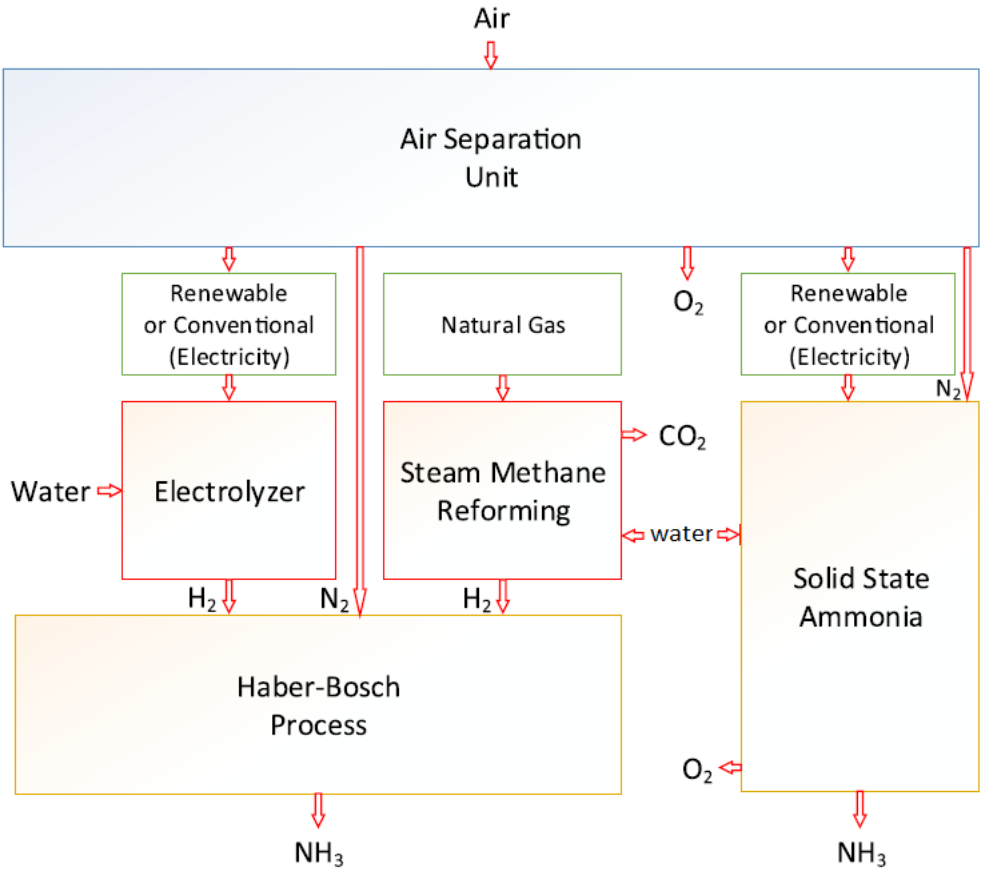

Figure 2.2: Two most common methods of ammonia production [76]. Both processes have renewable options for ammonia synthesis.

Since the source of the nitrogen has been explained, the two processes for ammonia production will be looked at. The most used process for ammonia production is the Haber-Bosch process. This technique is a thermo-catalytic process where nitrogen gas reacts with hydrogen gas in a ratio of 3:1 to produce ammonia [76]. It is also an exothermic process that occurs at a temperature and pressure range of 450 - 600°C and 100-250 bar, respectively.

$$3H_2 + N_2 \rightarrow 2NH_3 + 90.4\text{kJ/mol} \tag{2.1}$$

Figure 2.2 also shows that the hydrogen gas used in the Haber-Bosch process is synthesized by using either electrolysis of water or steam reforming of natural gas. The use of water electrolysis also circumvents the release of contaminants (COS and H_2S gas) caused by a catalyst such as sulfur used for hydrogen production through stream reforming [49]. However, only about 0.5% of

ammonia production worldwide currently use electrolysis of water for its hydrogen generation [55]. This is because the use of water electrolysis for industrial production of ammonia is still being developed to be economically as competitive as the steam reforming process [72].

Figure 2.2 also shows an electrochemical process where nitrogen, water, and electricity are used to yield ammonia. This process is called Solid State Ammonia Synthesis (SSAS). In this technique, an electrochemical cell consisting of a protonic solid-state electrolyte, an anode, and a cathode is used for the ammonia synthesis [45]. As shown in reaction 2.2, water vapor is passed over the anode to produce hydrogen ions (protons) and oxygen gas.

$$3H_2O \rightarrow 6H^+ + \frac{3}{2}O_2 + 6e^- \tag{2.2}$$

These protons then travel through the conductive electrolyte to the cathode where the half-cell reaction in equation 2.3 occurs. The resulting overall chemical reaction of both half-cell reactions is given in equation 2.4.

$$N_2 + 6H^+ + 6e^- \rightarrow 2NH_3 \tag{2.3}$$

$$3H_2O + N_2 \rightarrow 2NH_3 + \frac{3}{2}O_2 \tag{2.4}$$

Additionally, the SSAS process overcomes the thermodynamic limitation of high pressure and temperature as in the catalytic Haber-Bosch process because the hydrogen ions needed for ammonia synthesis are produced through the electrochemical process at lower temperatures [45]. However, a detailed cost analysis of the SSAS process needs to be investigated to provide an economic comparison with the Haber-Bosch process.

2.3 Fundamental flame characteristics

To study and comprehensively understand the flame structure, flame stability, and reaction mechanisms of NH_3/air and NH_3/H_2/air flames, the combustion parameters of these flames need to be investigated either experimentally or numerically. One of those parameters is the laminar burning velocity (or laminar flame speed), which is defined in Law's book [34] as the velocity at which an unstretched adiabatic flame propagates relative to the unburned gas mixture in a direction normal to the flame surface. The Markstein length (or Markstein number), which quantifies the sensitivity of the laminar burning velocity to the strain rate of the flame due to thermo-diffusive effects [34], is another essential parameter to be considered. Additionally, the blow-off limit that denotes the maximum burning velocity above which a premixed flame blows out of the combustion chamber [34], is another important parameter used to investigate the stability of NH_3/air flames. In this section, the dependence of these combustion parameters on equivalence ratio, pressure, and air temperature are examined for NH_3/air and NH_3/H_2/air flames. The potential of hydrogen as a carbon-free fuel to increase the burning velocity of ammonia combustion is also investigated.

Hayakawa et al [58] experimentally measured the laminar burning velocity and Markstein length of NH_3/air premixed flames at a pressure range of 0.1 - 0.5 MPa and equivalence ratio range of 0.7 - 1.3. High-speed schlieren imaging was used in this research to examine spherically premixed flames propagating in a constant volume chamber. Hayakawa et al [58] discovered that the laminar burning velocity has a maximum value at an equivalence ratio of 1.1 for all initial mixture pressures. However, this research showed that the laminar burning velocity decreases with an increase in the initial mixture pressure. Additionally, the Markstein length measured in [58] increases with increasing equivalence ratio.

Similar to results found in the previous research, Takizawa et al. [38], Pfahl et al. [24], Zakaznov et al. [11] and Ronney [17] all experimentally discovered the same trend of the laminar burning velocity and Markstein length dependence on equivalence ratio for NH_3/air premixed flames. The results of these research works are plotted on the same axes in the review paper by Kobayashi et al. [75] for comparison, as shown in Figure 2.3. The experimental results for the same initial

mixture pressure in the figure are approximately equal at the same equivalence ratio. As obtained from Figure 2.3, the maximum value of laminar burning velocity is about 7 cm/s, which is about 5 times lower than that of a CH_4/air premixed flame [34].

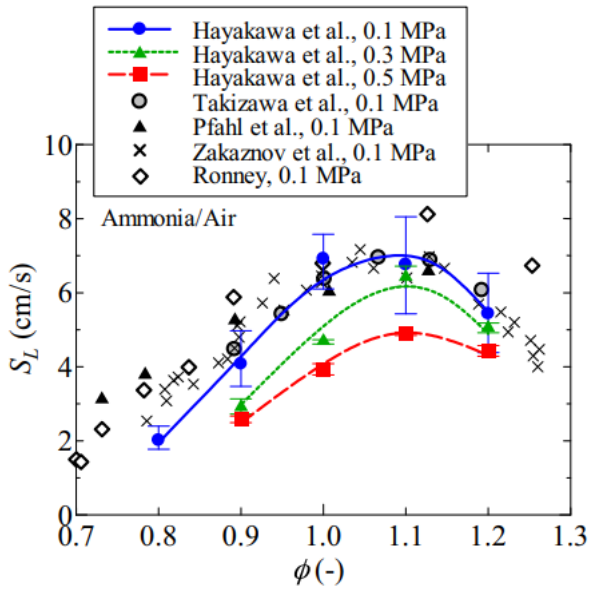

Figure 2.3: The dependence of the unstretched laminar burning velocity of ammonia/hydrogen premixed flames on the equivalence ratio. Kobayashi et al. [75] plotted on the experimental results of Hayakawa et al. [58], Takizawa et al. [38], Pfahl et al. [24], Zakaznov et al. [11] and Ronney [17] with the same abscissa and ordinate axes.

As mentioned in section 2.1.1, a carbon-free fuel such as ammonia is frequently mixed with hydrogen to improve its combustion with air. The potential of hydrogen, as a dopant fuel to enhance the characteristics of NH_3/air premixed flames, was investigated by Ichikawa et al. [59] and Lee et al. [44]. Experiments were carried out on outwardly-propagating spherical laminar premixed flames in [59] to measure unstretched laminar burning velocity and Markstein number using high-speed shadowgraphy imaging. In this research, the NH_3/H_2/air flames were investigated in test conditions that consisted of equivalence ratios of 0.60–1.67, hydrogen molar fractions of 0–0.5, and flame stretch rates (in terms of Karlovitz number) of 0–0.8 at normal pressure and temperature. Furthermore, the measured unstretched laminar burning velocity and Markstein number increase with an increase in hydrogen molar fraction, especially in fuel-rich conditions. This result shows that the addition of hydrogen improved the response of the premixed flames to stretch.

Similarly, Ichikawa et al. [59] experimentally measured the unstretched laminar burning velocity and Markstein length of spherically propagating NH_3/H_2/air flames. Unlike in [44], these flames were tested using high-speed schlieren imaging under test conditions consisting of pressures of 0.1-0.5 MPa, an equivalence ratio of 1, and a varied hydrogen molar fraction from 0 (NH_3/air flame) to 1 (H_2/air flame). It is also found in this study that the unstretched laminar burning velocity of the premixed flames increases with an increase in the hydrogen molar fraction. However, the measured Markstein length is found to have a non-monotonic relationship with hydrogen molar fraction. This result is different from the one found by Lee et al. [44] on how hydrogen addition influences the Markstein length. One can associate this difference with the varying pressure condition that is absent in [44], and further investigation needs to be done to confirm this.

Similar trends of the unstretched laminar burning velocity dependence on hydrogen molar fractions in NH_3/H_2/air premixed flames are found by other researchers [52, 54]. These trends

are plotted on the same axes in another review paper by Kobayashi et al. [75] for comparison, as shown in Figure 2.4. In addition, the figure shows that the unstretched laminar burning velocity of NH_3/H_2/air premixed flames, when compared to CH_4/air premixed flames, reaches the same order of magnitudes at a hydrogen molar fraction of 0.4.

Choi et al. [56] carried out experiments on non-premixed NH_3/H_2/air counterflow flames at elevated temperature and normal pressure to investigate the efficiency of hydrogen as a carbon-free fuel used to improve the stability of NH_3/air non-premixed flames. Results in this study show that hydrogen addition to the ammonia fuel enhances its flame stability by increasing the blow-off limit of the NH_3/H_2/air non-premixed flame. The researchers in this study also discovered that the blow-off limits and flame temperature increase with air temperature, signifying that the flames can be stabilized under practical conditions in a combustion chamber.

In conclusion, various experimental studies carried out on NH_3/H_2/air flames (premixed and non-premixed) have shown that mixing ammonia with hydrogen improves its flame stability. However, how this mixing influences the reaction mechanism of the combustion process used for numerical modeling is yet to be investigated. This will be examined extensively in the next section of this report.

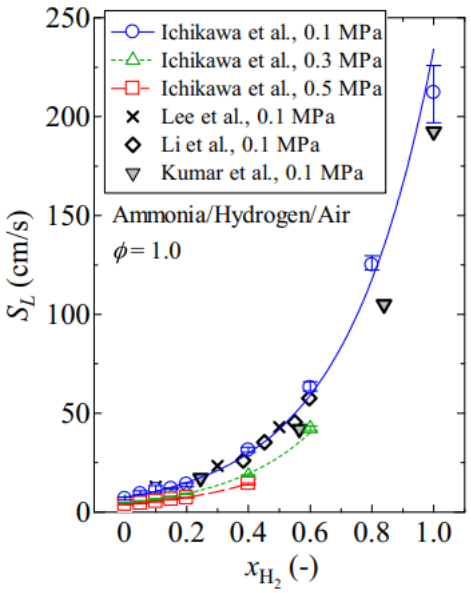

Figure 2.4: The influence of increasing hydrogen molar fraction added to the NH_3/air mixture on the unstretched laminar burning velocity of its premixed flame. The results were evaluated experimentally by Ichikawa et al. [59], Lee et al. [58], Li et al. [54], and Kumar et al. [52] at a mixture temperature of 298 K and plotted on the same abscissa and ordinate axes (retrieved with permission from [75]).

2.4 Reaction mechanisms

The prediction of the flame characteristics and stability of ammonia flames using computational tools requires a detailed understanding of its reaction mechanism, which are the multiple reactions occurring simultaneously in the combustion process. The chemical species that influence the production and removal of certain emissions such as NO_x can be identified using these reaction mechanisms. Several researchers have investigated NH_3/air flames and generated several models of its reaction mechanism.

To the best of the authors' knowledge, Miller and Bowman [18] presented the first comprehen-

sive reaction mechanism for ammonia oxidation through the ammonia combustion experiments carried out over a range of temperatures, equivalence ratios, and pressure. The study also showed that the measured concentration profile of major species is in good agreement with the concentration profile predicted by the proposed reaction mechanism. This mechanism signifies that the oxidation of NH_x free radicals results in the formation of NO. For example, the oxidation of the amidogen (NH_2) radical through nitroxyl (HNO) by a reaction sub-mechanism is shown below.

$$\begin{aligned} O + NH_2 &\rightleftharpoons HNO + H \\ HNO + M &\rightleftharpoons NO + H + M \\ HNO + OH &\rightleftharpoons NO + H_2O \\ HNO + NH_2 &\rightleftharpoons NO + NH_3 \end{aligned}$$

The proposed mechanism also shows the NH_x free radicals can react with NO to form molecular nitrogen(N_2), as shown below in reaction 2.5.

$$NH_2 + NO \rightleftharpoons N_2 + H_2O \tag{2.5}$$

Additionally, the thermal production and removal of NO by nitrogen atoms through the extended Zeldovich mechanism [28] are illustrated in the mechanism presented by Miller and Bowman [18] as shown below.

$$N + NO \rightleftharpoons N_2 + O \tag{2.6}$$
$$N + O_2 \rightleftharpoons NO + O \tag{2.7}$$
$$HNO + OH \rightleftharpoons NO + H_2O \tag{2.8}$$
$$NO + O \rightleftharpoons NO + H \tag{2.9}$$

Moreover, an extensive sensitivity analysis is carried out by Miller and Bowman [18] to find the reactions that significantly contribute to the amount of NO formed or removed. The formation of nitroxyl (HNO) via reaction 2.10 in the oxidation reaction sequence of NH radical and the nitrogen atom reactions 2.11 and 2.12 are found to be the main rate-controlling reactions in the production of NO.

$$NH + OH \rightleftharpoons HNO + H \tag{2.10}$$
$$N + O_2 \rightleftharpoons NO + O \tag{2.11}$$
$$N + OH \rightleftharpoons NO + H \tag{2.12}$$

The removal of NO to form molecular nitrogen is primarily controlled by reaction 2.13.

$$N + NO \rightleftharpoons N_2 + O \tag{2.13}$$

Lindstedt et al. [20] used the mechanism in [18] to experimentally develop a model mechanism for pure NH_3/air and NH_3/H_2/air combustion using a wide range of laminar flat premixed flames. Having done an extensive sensitivity analysis, the researchers discovered that reaction 2.10 in Miller and Bowman's mechanism becomes more significant in the formation of NO for pure ammonia flames as the fuel-based equivalence ratio increases. In addition, the researchers found that the extended Zeldovich mechanism [28] becomes more significant in the formation of NO in NH_3/H_2/air flames as the fuel-based equivalence ratio increases. Furthermore, the study showed the removal of NO through its conversion to molecular nitrogen (N_2) is mostly caused by the reaction 2.5 for pure NH_3/air and fuel-lean NH_3/H_2/air flames. Similarly, Lindstedt et al. [20] unearthed that NO removal is mostly caused by reaction 2.6 of the Zeldovich mechanism for stoichiometric and fuel-rich NH_3/H_2/air flames.

One of the several groups of researchers (Lee et al [44]) mentioned in section 2.3 used the model mechanisms proposed by Miller and Bowman [18], and Lindstedt et al. [20] to numerically predict the Markstein number and unstretched laminar burning velocity of premixed laminar NH_3/H_2/air flames. In addition, this group of researchers compared their predictions to the results they obtained experimentally. The predicted and measured parameters are seen to generally be in concurrence for all test conditions except for the large fuel-lean mixtures with large hydrogen concentrations. This exception supports the observation discovered by Mathieu and Petersen [61], where large discrepancies are found in the prediction of the ignition delay time by the mechanisms from literature due to unclear test conditions reported in the shock-tube experiments used to develop these model mechanisms. Thus, Mathieu and Petersen [61] examined ammonia combustion by carrying out shock-tube experiments at high temperatures (1560 – 2455 K) and pressure conditions of around 0.14, 1.1, and 3.0 MPa. These researchers also developed a new kinetic mechanism by improving the existing ones for ignition delay time predictions. The resulting mechanism model predicts the ignition delay time with high accuracy at elevated conditions that apply to many industrial purposes. A state-of-the-art NO_x sub-mechanism is also made available in [61] for combustion simulations of a wide range of other fuel mixtures containing hydrogen and hydrocarbons.

More detailed kinetic model mechanisms have been developed for the combustion of pure ammonia and ammonia-fueled mixtures with air in the recent decade. However, discussing each one of them will be too detailed for a review such as this report. Thus, Da Rocha et al. [73] compared the predicted shock-tube ignition delay time, laminar flame speed and NO_x concentration of NH_3/air and NH_3/H_2/air flames using 10 of these mechanisms [37, 39, 40, 46, 48, 61, 65, 69–71] from literature at a temperature of 298 K and pressure of 1 bar. In addition, Da Rocha et al. [73] compared these predicted values with the measured ones obtained experimentally by the researchers from literature.

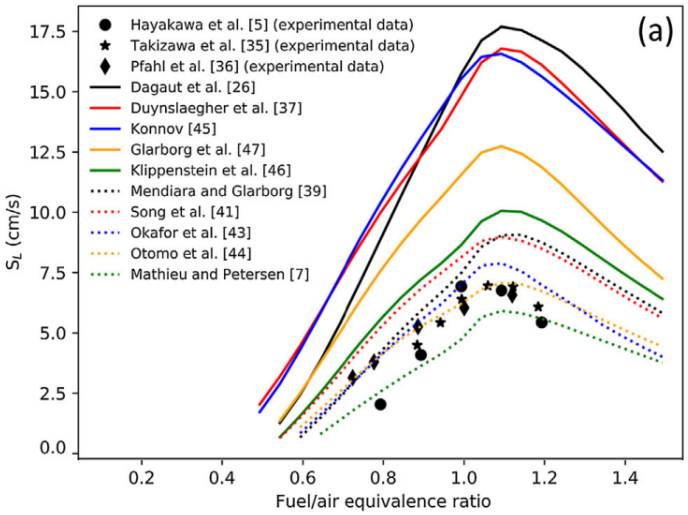

Figure 2.5: Comparison of the predicted laminar flame speed of NH_3/air premixed flames obtained using 10 model mechanisms with measured ones from experiments carried out by Hayakawa et al. [58], Takayawa et al. [38] and Pfahl et al. [24]. This plot is obtained from the numerical modeling done by Da rocha et al. [73].

For example, the predicted laminar flame speeds were obtained using all 10 mechanism models and measured ones from experiments carried out by Hayakawa et al. [58], Takizawa et al. [38] and Pfahl et al. [24]. These speeds are plotted against the equivalence ratio using the same axes, as shown in Figure 2.5. It is important to note that two of the three experiments carried out to obtain

the measured flame speeds have been discussed in section 2.3 of this report. Figure 2.5 also shows that the predicted flame speeds of all the mechanisms, except those of Mathieu and Petersen [61], Okafor et al. [70] and Otomo et al. [70] are higher than the ones measured experimentally. Although the mechanisms developed by Mendiara [40] and Glarborg [69] produce good flame speed predictions at fuel-lean and stoichiometric conditions, these mechanisms overestimated the flame speeds at fuel-rich conditions. The researchers also discovered that the scattered ignition delay times and NO_x concentrations in NH_3/air flames are predicted by the mechanism models, similar to the predicted flame speeds in Figure 2.5.

In conclusion, the discrepancies signify that the mechanisms of NH_3/air and NH_3/H_2/air combustion still need to be improved to make the simulation of these flames less difficult, as concluded by Da rocha et al. [73]. However, the predictions made by all the mechanisms showed qualitatively, that the addition of hydrogen to the NH_3/air flames improved its combustive behavior by increasing the flame speed and reducing the ignition delay time. Although this finding is in agreement with the results discovered by Koyabashi et al. [75] in Figure 2.4, Da rocha et al. [73] also discovered that the hydrogen addition increases the NO_x concentration in the NH_3/air flames.

In this project, quantitative data comprising the temperature and molar fractions of major species along the symmetric axis of laminar non-premixed H_2 and $NH_3/H_2/N_2$ flames are obtained experimentally using a laser diagnostics technique called *Raman spectroscopy*. The measured molar fractions in this data can be used to improve the subgroup of reactions in the existing model mechanisms that give rise to the major species. In addition, this data can be compared to the flame temperatures predicted by the existing model mechanisms in a bid to know which of their sub-reactions cause an underestimation or overestimation of temperature.

Chapter 3

Methodology

In this chapter, the approach used to acquire quantitative data on $NH_3/H_2/N_2$ flames is discussed. Firstly, the categorization of flames is explained to illustrate the type of flames measured in this project. Secondly, the principle of laser diagnostics is briefly studied before finally introducing the concept of Raman spectroscopy, which is the measurement technique used in this project.

3.1 Classification of flames

Fluid flows are categorized into laminar and turbulent flows based on the interaction between the fluid layers. These flow regimes are identified using a dimensionless parameter called the Reynolds number (Re) which is expressed as:

$$Re = \frac{UL}{\nu} \tag{3.1}$$

where U is the mean velocity in m/s, L is the characteristic length scale in m, and ν is the kinematic viscosity of the fluid in m^2/s. Although fluid flows with low Reynolds numbers (Re <2300) are usually classified as laminar, the transition of the flow regimes to turbulence does not always occur at the same Reynolds number. This is because the choice of U and L in Equation 3.1 depends on the geometric domain in which the fluid moves. For example, L is defined as the diameter of the pipe for flows in circular pipes. However, this transition from laminar to turbulence is seen by investigating how the fluid structures in the flow interact with one another.

In laminar flows, the adjacent fluid layers slide smoothly past each other with minimal interaction, making the flow steady. Hence, these flows' local velocities and densities do not change rapidly over time, making measurements in this flow regime easier to obtain. Regarding combustion, the laminar flames are generated using the laminar flow of fuel and oxidizer at low gas velocity. These flames are found in small-scale applications such as gas cookers and candles. In turbulent flows, there are large vortices of varied sizes interacting with each other, causing the flows to be chaotic. These interactions make the local velocities and density of the flow fluctuate rapidly with time. Unlike laminar flows, these flow fluctuations called eddies are what make measurements in turbulent flows difficult to acquire. Nonetheless, turbulence enhances combustion by improving the mixing of the fuel and oxidizer through the eddies. The resulting flame produced by turbulent flows is called a turbulent flame. One can find such flames in large-scale applications like internal combustion engines, jet engines, and blast furnaces.

Flames can also be divided into two categories based on how the reactants of the combustion process are transported to the expected region where oxidation occurs. Premixed flames are generated when the fuel and oxidizer are mixed before they get to the reaction zone where oxidation takes place. One advantage of premixing is low pollutant emissions because there is always an oxidizer around the fuel for complete combustion, provided that system contains enough oxygen. However, the fuel-oxidizer mixture can be explosive, resulting in sudden ignition before it reaches the intended reaction zone. Hence, non-premixed flames are introduced in many practical combustors to ensure safety. In this case, the fuel and oxidizer are transported as separate streams to the reaction zone for combustion. The non-premixed flame generated is largely controlled by the diffusion of both streams since it is a slower process compared to the oxidation of fuel at the

reaction zone. Moreover, the diffusion process is essential for mixing the reactants necessary for combustion. This is why non-premixed flames are historically called diffusion flames.

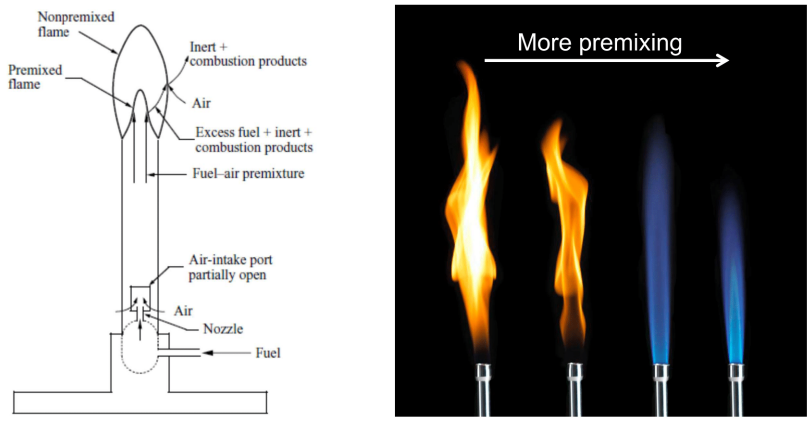

Figure 3.1: Schematic representation of premixed and non-premixed flame generated using a Bunsen burner [79]. More premixing of fuel and air decreases the amount of soot in the flame.

Another potential setback in non-premixed flames is incomplete combustion of the fuel. This arises due to little or no presence of the oxidizer in certain regions of the flame. In the case of hydrocarbon fuels, incomplete combustion causes the partially decomposed fuel species to react with each other to produce unwanted particles called soot. Figure 3.1 illustrates the production of the soot particles in the yellow region of the first flames generated by the Bunsen burner. As more premixing of the fuel and air occurs, one can see in Figure 3.1 that the amount of soot produced reduces to a point where it is absent.

In this project, the focus is on laminar diffusion flames generated using hydrogen, ammonia, nitrogen, and air. The temperature profile and the concentration of the chemical species in the flame need to be measured to provide quantitative data that can be used to verify the accuracy of ammonia/hydrogen reaction mechanisms. To do this, a diagnostic technique that has little or no interaction with the flame should be employed. One viable candidate is laser diagnostics because its techniques minimally intrude chemical processes such as oxidation [26].

3.2 Laser diagnostics

The interaction of light and matter is the basis on which Laser diagnostic techniques for chemical processes operate. These techniques can be used to detect major and minor chemical species and temperature in a flame with minimal disturbance [63]. A highly directional, coherent, and monochromatic light generated by a laser is used to probe the region of interest for measurements. The laser emits many photons and the energy of each photon is expressed using Planck's equation [21]:

$$E = h\nu = \frac{hc}{\lambda} = hc\bar{\nu} \tag{3.2}$$

where h is Planck's constant ($6.626 \cdot 10^{-34}$ Js), ν is the frequency in Hz, c is the speed of light in cm/s, λ is the wavelength in cm and $\bar{\nu}$ is wavenumber in cm^{-1}. Individual molecules and atoms interact with these photons by exchange of energy through absorption, emission, or light scattering. Using the energy conversion principle, the absorbed or emitted photon is expressed in

Equation 3.3 as a function of the higher energy state, E', and lower energy state, E'' of the atoms and molecules.

$$E' - E'' = hc\bar{\nu} \tag{3.3}$$

However, it is vital to note that not every wavelength of light is absorbed or emitted by a specific atom or molecule. The reason is that the energy states of a particular atom or molecule are quantized into discrete levels [62]. Moreover, the characteristic nature of the energy levels for every atom or molecule is utilized in Laser diagnostics to identify the species present in chemical processes such as combustion.

One Laser diagnostics technique for species identification is Laser-induced Fluorescence (LIF). It is called a resonant method because a laser producing photon energy that matches the transition from a lower energy level to a higher energy level of molecules of a distinct species is used. A deviation from thermal equilibrium, caused by the excitation of the molecules, results in the spontaneous emission of another wavelength of light (fluorescence). This is because the excited molecules restore thermal equilibrium by relaxing to a lower energy level via light radiation. One advantage of the LIF method is the detection of a single species with little or no interference from other species present. However, the excited molecules in LIF, in addition to fluorescence, lose energy through interactions with their environment. This makes LIF measurements difficult to quantify because the knowledge of these non-radiative interactions is complicated [77]. To circumvent this setback, Raman scattering can be employed because environmental interactions in this technique are minimal. Additionally, it makes the simultaneous detection of multiple major species possible.

3.3 Rayleigh and Raman scattering

Absorption, spontaneous emission, and fluorescence are known to happen if the photon energy of light matches an allowed transition between two energy levels of an atom or molecule. As a result, these processes are said to be resonant. However, higher-order phenomena can occur when the light is not resonant with the molecules or atoms in the interacting medium. Rayleigh and Raman scattering are examples of this non-resonant process that can occur at almost any wavelength of incident light [62]. In LIF, the excited molecules stay at a higher energy level for a limited time before relaxing to a lower energy level through fluorescence. On the other hand, Rayleigh and Raman scattering are instantaneous processes involving the destruction of a photon incident on a molecule and the creation of another photon that occurs simultaneously [77].

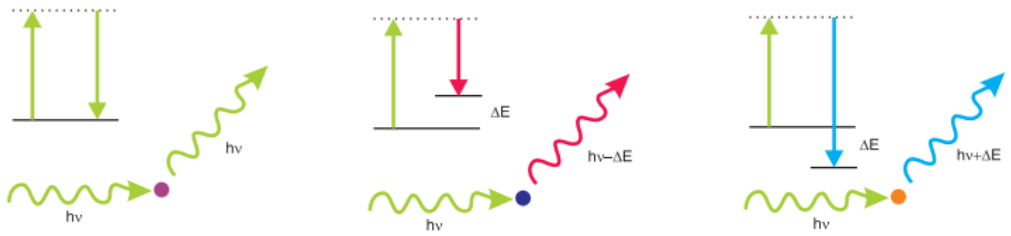

(a) Rayleigh **(b)** Stokes Raman **(c)** Anti-stokes Raman

Figure 3.2: Schematic diagram of Rayleigh and Raman scattering. Left image shows the scattered photon of equal energy as the incident photon in Rayleigh scattering. The scattered photon in the middle and right image are of lesser (Stokes) or higher (Anti-stokes) energy compared to incident photon in Raman scattering.(From [77], with permission)

If the scattered photon depicted in Figure 3.2a has the same energy as the incident photon, the scattering phenomenon is elastic and called Rayleigh scattering. Since there is no energy lost or

gained by the scattering molecule or atom, Rayleigh scattering is not chemical species-specific. Additionally, it is used for density measurements because its intensity is proportional to density in a flow with constant chemical composition [63]. On the other hand, light scattering is said to be inelastic if the scattered photon, as shown in Figure 3.2b and Figure 3.2c, has a different energy than the incident photon. This process is called Raman scattering. In this case, there is an exchange of energy between the incident photon and the scattering molecule or atom. Hence, it is chemical species-specific because each type of atom or molecule has a specific spacing of discrete energy levels. The energy exchange can be described mathematically using Equation 3.4:

$$E_i + h\nu_{inc} = E_f + h\nu_{scat} \tag{3.4}$$

where the subscripts i and f denote the initial and final energy levels of the scattering molecule and *inc* and *scat* denote incident and scattered photons. Equation 3.4 is derived by applying the principle of energy conversation on the two-photon processes in Figure 3.2. When the scattered light has a lower photon energy(longer wavelength) than the incident light, the two-photon event is called *Stokes Raman scattering*. The so-called *Anti-Stokes Raman scattering* occurs when the photon energy of the scattering light is higher than that of the incident light.

Given that Raman scattering is a linear process, its intensity is directly proportional to the concentration of the scattered molecule. Although Raman scattered light intensities are much weaker and less efficient than typical LIF measurements [77]. However, Raman scattering can be used to obtain temperature in a particular flow medium. Firstly, this is because the Stokes Raman intensities are a representation of the population distribution of the scattering molecules at the initial energy levels, as shown in Figure 3.2b. Secondly, the population distribution around the energy levels is a function of temperature, as discussed in chapter 4. Moreover, the weak intensity of Raman signals can be solved by accumulating many pulses of the signals. Laser-induced Fluorescence by other minor species and Laser-induced incandescence of particles can also interfere with the Raman signals [63]. To minimize the interference, Raman scattered light is captured in a series of short pulses where the exposure time of the detector coincides with the time at which the pulsed laser is triggered. The minimization is achieved because Raman scattered photons are only received by the detector during the short pulse duration, leaving LIF and Laser-induced incandescence signals that have longer lifetimes. Time gating is the name used to describe the laser and detector synchronization and the technique is called Time-gated Raman spectroscopy [78].

In this project, a pulsed Laser is used to probe the center line of NH_3/H_2 diffusion flames. The time-gated Raman scattered light is captured to obtain the measured temperature and molar fraction of major species such as H_2, O_2, H_2O, N_2 and, NH_3 in the flames.

Chapter 4

Spectroscopy

As explained in the previous chapter, the wavelengths of the Raman scattered light are like a fingerprint containing the information about scattering molecules present in the probed area of interest. Owing to this fact, the temperature and molar fractions of these molecules can be determined, provided that their relationship with the wavelengths are known. In this chapter, the parameters required to describe the Raman scattering process are explained. Additionally, the functional dependence of the intensity of Raman scattered photons on these parameters are mathematically outlined for spectral simulations of Raman scattering processes attributed to different species.

4.1 Molecular energy levels

It has been established in chapter 3 that the energy of molecules is quantized. This energy only has specific and discrete values which are called energy levels. It is also important to note that the energy levels are very specific to each kind of molecule. For example, the energy levels of molecular oxygen, O_2 are different from those of molecular hydrogen, H_2. The quantization of these molecular energy levels are derived from the quantum-mechanical description, which describes molecules as a collection of negatively charged electrons and positively charged nuclei. Moreover, the position of the electrons and nuclei are stated in terms of a probabilistic function of electric charge distributions. This is in contrast to classical mechanics that uses the exact location of objects to illustrates their motion. Hence, a parameter called the *wave function* is used to represent the likelihood that the electrons and nuclei exist in a particular space at given time. The evolution and structure of this wave function is demonstrated by an equation of motion called the *Schrödinger equation*, which needs to be solved to fully understand the interaction of light with molecules [77]. The solution of the Schrödinger equation is not discussed because it is beyond the scope of this research project. Nevertheless, It is vital to note that molecular properties, including energy levels, are derivatives of the features associated with the wave function.

Molecules are considered a multi-particle system that consists of at least two atoms. Hence, this system has multiple degrees of freedom that are attributed to rigid body translation of the molecule as a whole, three rigid rotations and internal vibration of its nuclear frame, and electronic distribution of the molecule. Since the rigid translation is independent of the internal structure of the molecule, the total internal energy can be evaluated using the other three contributions to degrees of freedom as follows:

$$E = T_e + T_v + T_r \tag{4.1}$$

where T_e, T_v and T_r are the electronic, vibrational and rotational energy contributions respectively. Equation 4.1 implements the so-called *Born-Oppenheimer approximation* that assumes the electrons adapt instantaneously to changes in the structure of the nuclear framework [21]. This approximation is made due to the small mass of the electrons surrounding the nuclei. Consequently, It makes the electronic energy independent of the internal vibrations and rotations of the nuclear framework. Additionally, these contributions usually vary in order of magnitude such that $T_e \gg T_v \gg T_r$. As a result, each contribution to the internal energy is examined as a separate entity for diatomic molecules.

4.1.1 Electronic energy levels

The electronic energy levels, T_e depend on the distribution of electrons in a molecule. There are no analytical expressions for T_e due to the complex nature of the corresponding Schrödinger equation that is to be solved. For this reason, the values of T_e for a particular kind of molecule are either obtained from experiments or numerical solutions of the Schrödinger equation. For qualitative description, these energy levels are denoted using molecular term symbols, which briefly indicate some symmetry properties of the molecule. The general notation for diatomic molecules is given as follows:

$$\textbf{name}^{2S+1}\Lambda^{\pm}_{u/g}$$

where **name** is written using a single letter such as X for the electronic ground states (lowest possible electronic energy) and S signifies the total spin of the electronic configuration. For example, $X^3\Sigma_g^-$ and $A^2\Sigma^+$ are the electronic ground state of molecular oxygen and first electronically excited state of OH-radical, respectively [21].

4.1.2 Vibrational energy levels

The electronic states of a particular kind of molecule can also be presented graphically using the potential energy curve as shown in Figure 4.1. This curve depicts the potential energy of a diatomic molecule as function of the inter-nuclear distance between its two atoms. Hence, the curve represents the electric force field that drives the vibrational motion of the two nuclei in a diatomic molecule.

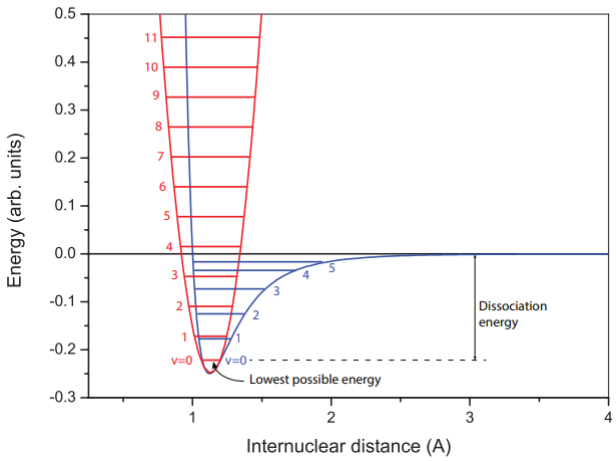

Figure 4.1: A comparison of the real potential energy of a hypothetical potential energy curve (blue) and the harmonic oscillator approximation (red) near the minimum potential energy. The blue curve has a finite number of vibrational energy levels while there are infinitely many energy levels on the red curve (retrieved with permission from [77]).

As seen in Figure 4.1, the potential energy curve has a parabolic shape at inter-nuclear distances very close to the equilibrium value, r_e where the electronic potential energy is minimum. At this range of inter-nuclear distances, the potential energy of the molecule is similar to that of the well-known classical system of two particles connected by a Hooke's law spring. Thus, the actual potential energy curve can be approximated with a best-fit parabola called the *Harmonic oscillator approximation* [62], as shown in Figure 4.1. In addition, the parabolic fit can be expressed mathematically as in Equation 4.2:

$$V(r) = \frac{1}{2} q_s (r - r_e)^2 \tag{4.2}$$

where q_s and r_e are the spring constant and equilibrium inter-nuclear distance, respectively. However, the vibrational energies of diatomic molecules have discrete values, as mentioned earlier in this chapter. Hence, harmonic oscillator approximation is simplified into an analytic expression:

$$T_v = \omega_e (v + \frac{1}{2}) \quad with \quad v = 0, 1, 2, 3, ... \tag{4.3}$$

in which T_v is the vibrational energy of the molecule in cm^{-1}, ω_e is the molecule-specific *vibrational constant* in cm^{-1}, and v is the *vibrational quantum number*. The value of ω_e can be expressed as a measure of the curvature of the potential curve near the minimum:

$$\omega_e = 0.01 \frac{\sqrt{q_s/\mu}}{2\pi c} \tag{4.4}$$

where μ is the reduced mass of the two nuclei in kg and c is the speed of light in ms^{-1}. The constant factor, 0.01 is used in Equation 4.4 to ensure the vibrational constant, ω_e is in cm^{-1}.

By evaluating $T_{v+1} - T_v$, the energy difference between two adjacent vibrational energy levels in the Harmonic oscillator approximation is to found to be equivalent to the vibrational constant, ω_e. This means the spacing of the vibrational energy levels associated with best-fit parabola is constant and independent of the vibrational quantum number, v. An implication of this result is evident in the red curve plotted in Figure 4.1 where there are infinitely many vibrational energy levels in the Harmonic oscillator approximation. However, the real potential energy curve plotted as the blue curve in Figure 4.1 has a finite number of vibrational energy levels. This results from a broader curvature of the real potential energy curve at higher energy levels, which consequently causes a decrease in the effective spring constant, q_s. Thus, the harmonic oscillation approximation in Equation 4.3 is refined to a more accurate approximation by adding higher order anharmonics [62]:

$$T_v = \omega_e (v + \frac{1}{2}) + \omega_e x_e (v + \frac{1}{2})^2 + \omega_e y_e (v + \frac{1}{2})^3 + ..., \tag{4.5}$$

in which all the constants are positive, and $\omega_e \gg \omega_e x_e \gg \omega_e y_e$.

4.1.3 Rotational energy levels

The rotational energy of a diatomic molecule can be approximately evaluated by modelling the molecule as a rigid body with three principal axes of rotation. The molecule is assumed to rotate as a whole in this *rigid body approximation*, and the principal moment of inertia with respect to the principal axes can be expressed as:

$$I = \sum_j m_j r_j^2 \tag{4.6}$$

where m_j is the mass of each atom in the molecule, and r_j is the distance from the principal axis. Using Equation 4.6, It can be derived that the moment of inertia around the internuclear axis of the diatomic molecule is zero. Additionally, the moment of inertias around the remaining two principal axes, which are perpendicular to internuclear axis, are equal and non-zero. Hence, The rotational energy of the diatomic molecule is related to only one moment of inertia, and can be defined using the quantum mechanical picture as:

$$T_r = BJ(J+1) \quad with \quad J = 0, 1, 2, 3, ... \tag{4.7}$$

in which J is the rotational quantum number, and the rotational constant, B is defined as in Equation 4.8.

$$B[\text{cm}^{-1}] = \frac{0.01h}{8\pi^2 cI} \tag{4.8}$$

It is important to note that the Planck constant, h, speed of light, c and moment of inertia, I in Equation 4.8 are in SI units.

As the diatomic molecule rotates, the centrifugal forces exerted on its atomic cores stretches the connecting bond, which in turn results in an increase in moment of inertia and a decrease in rotational constant, B. Furthermore, the periodic stretching and compression due to vibration give rise to a decrease in rotational constant, B as the vibrational amplitude increases [62]. This is because stretching and compression causes the moment of inertia to increase since the distance is a squared term in Equation 4.6. By accounting for the dependence on vibration and centrifugal stretching, the rigid rotor approximation can be improved by adding a higher order term as follows:

$$T_r = [B_e - \alpha_e(v + \frac{1}{2})]J(J+1) - D_e J^2(J+1)^2 + ... \tag{4.9}$$

where the vibrational quantum number,v and two new constants, α_e and D_e are included in the first term. The subscript, e in Equation 4.9 indicate that all the constants depend on the electronic state that the molecule resides in.

The correct values of the constants in Equation 4.9 and Equation 4.5 can be found in literature for a specific kind of molecules. Using these values and the corresponding energy, T_e associated with the electronic state, All possible transitions can be calculated. Nevertheless, not all those transitions are certain to occur.

4.1.4 Selection rules

The probability that a possible energy transition would take place through light-matter interaction is another outcome of the quantum-mechanical description [21]. This probability depends on the details of the wave functions of the energy states involved in the transition [77]. The transitions that actually occur are named *allowed transitions*, which obey certain restrictions called *selection rules* [62]. The transitions that do not follow the selection rules are called *forbidden transitions*. In ro-vibrational Raman scattering of diatomic molecules, selection rules for changes in vibrational quantum number, v and rotational quantum number, J for allowed transitions are expressed as follows [62]:

$$\Delta v = \pm 1 \tag{4.10}$$

$$\Delta J = 0, \pm 2 \tag{4.11}$$

where $\Delta v = +1$ denote Stokes Raman scattering, and $\Delta v = -1$ signify anti-Stokes Raman scattering. In literature, the $\Delta J = 0$, $\Delta J = +2$, $\Delta J = -2$ transitions are collectively referred to as the Q,S and O branches of Raman spectra, respectively.

4.2 Boltzmann distribution

Although the selection rules predict transitions that are likely to occur, the amount of scattered photons still depends on the number of molecules present at each energy level. Thus, an efficient estimation of the population distribution of molecules over the available energy levels is required. For this reason, the so-called *Boltzmann statistics* is used to accurately predict the average number of molecules per available energy state, which only holds when the molecules are at thermal equilibrium [62]. Using Boltzmann statistics, the average number of molecules, N in a particular energy state specified by quantum number (e, v, J), at given temperature, T is expressed as:

$$N(e,v,J) = \frac{g_{evJ} g_I \exp\{-E(e,v,J)/(k_B T)\}}{Z(T)} N_0 \tag{4.12}$$

$$\text{with} \quad Z(T) = \sum_{evJ} g_{evJ} g_I \exp\{-E(e,v,J)/(k_B T)\} \tag{4.13}$$

in which N_0 is the total number of molecules (or number density), k_B is the Boltzmann constant, and $Z(T)$ is a normalization factor called the *partition function*, which guarantees that $\sum_{evJ} N(e,v,J) = N_0$. The degeneracy factors, g_{evJ} and g_I of each energy level represents the number of individual quantum states that have exactly the same energy [77]. The factor, g_{evJ} of diatomic molecules is only dependent on the rotational quantum number, J and is evaluated as $g_{evJ} = 2J + 1$. In homonuclear diatomics, the second factor, g_I is a function of the nuclear spin, I and is expressed as $f_I(2I + 1)$. The product (g_{nuc}) of f_I and g_{evJ} for the diatomic molecules investigated in this project is enumerated in Appendix B. In the case of heteronuclear diatomics, the value of g_I is a constant, which is expressed as $g_I = 1$. The population ratio between two energy levels can easily be calculated using Equation 4.12 because the temperature-dependent partition function cancels:

$$\frac{N'}{N''} = \frac{g'}{g''}\exp\{-\frac{\Delta E}{k_B T}\} \tag{4.14}$$

where the two degeneracy factors are combined as g and $\Delta E = E(e',v',J') - E(e'',v'',J'')$. Hence, the temperature can be determined if the population ratio between two energy states are known.

Since the electronic, vibrational and rotational energies are independent in the Born-Oppenheimer approximation, the population over their states can be computed separately. For example, the population of the vibrational quantum states is given by:

$$N(v) = \frac{\exp\{-E(e,v,J)/(k_B T)\}}{Z_v(T)} N_0 \tag{4.15}$$

$$\text{with} \quad Z_v(T) = \sum_v \exp\{-E_v/(k_B T)\} \tag{4.16}$$

where $Z_v(T)$ is the partition function related to the vibrational energy state. Similarly, the population of the electronic and rotational quantum states can be worked out in the same manner.

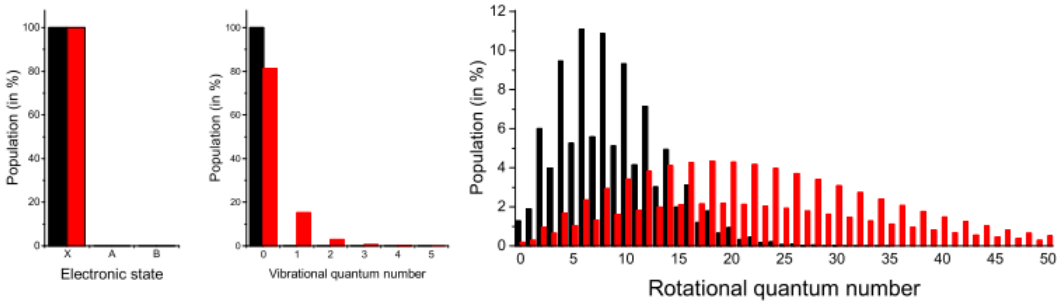

Figure 4.2: The Boltzmann statistically-derived population distribution of molecular nitrogen, N_2 over the electronic (left), vibrational (middle) and rotational (right) quantum states at room temperature (black) of 300 K, and at a typical flame temperature (red) of 2000 K (retrieved with permission from [77]).

The Boltzmann distribution of molecular nitrogen, N_2 over the energy states at room temperature (300 K) and at a typical flame temperature (2000 K) is plotted in Figure 4.2. Although the nitrogen molecules remain in the electronic ground states at both temperatures, there is a population redistribution over the vibrational and rotational energy states at the higher temperature. Moreover, Figure 4.2 shows that the nitrogen molecules, which populate the lowest vibrational energy states at room temperature, occupy higher vibrational energy states at 2000 K. A similar trend in the right view of Figure 4.2 where the population distribution at 2000 K has wider range of rotational energy states than that of the molecules in thermal equilibrium at 300 K.

To sum up, the Boltzmann distribution can be used the determine the energy states that are populated at a given temperature, the probable energy transitions can be evaluated with the aid of the selection rules. However, there is an additional factor that influences the number of photons scattered by molecules. This species-dependent parameter is called the *scattering cross-section*.

4.3 Scattering cross-section

The efficiency of light scattering is often described in terms of a parameter called the *scattering cross-section*. This is defined as an effective surface area of the molecule when it interacts with the incident light in a scattering process [23]. In scattering experiments, the light detectors are usually placed at some angular position relative to the direction of the incident light. Hence, the differential cross-section, $\frac{d\sigma}{d\Omega}$ with respect to the solid angle, Ω is measured for a specific molecule. In addition, the (differential) cross section is not only species-dependent but also depends on the polarization of the incident and scattered light. When light is pictured as an electromagnetic wave, the direction of the electric field that oscillates with time is defined as the *polarization* of light [62]. In light scattering, this polarization causes the electron cloud of a molecule to oscillate relative to the heavier nuclear core [21]. As a result, a periodic dipole moment is induced, which in turn brings about the scattering processes. The quantum mechanical theory that provides the detailed description of how the polarization of light influences the scattering cross-section is beyond the scope of this research project. However, it can be found in the different books on Raman spectroscopy [21, 27, 62]. The inferences of this theory are discussed instead in this section of this report. firstly, the so-called *Placzek model* used to describe this theory shows that the induced dipole moment can be split into three components. One of the components is responsible for Rayleigh scattering while the other two components give rise to Stokes and anti-Stokes Raman scattering [27]. Secondly, these scattering processes scale with a molecule-specific constant called *polarizability*.

The differential cross-section for diatomic molecules are derived using the *Placzek approximation* as a variable that is dependent on the polarization of the incident and scattered light [9]. The polarization is evaluated relative to the *scatter plane*, which is defined as the plane in which the directions of the incident and scattered light intersect. When the incident and scattered light are polarized parallel and perpendicular, respectively, to the scatter plane, the differential cross-section, $\frac{d\sigma}{d\Omega}$ can be denoted as

$$\frac{d\sigma^{\parallel\perp}_{imn}}{d\Omega}(\nu_{imn}) = (2\pi)^4\nu^4_{imn}(2J_n+1)\cdot\left[\frac{3}{45}\begin{pmatrix} J_n & 2 & J_m \\ 0 & 0 & 0 \end{pmatrix}^2 |\langle m|\gamma|n\rangle|^2\right] \tag{4.17}$$

and, when the incident and scattered light are both polarized perpendicular to the scatter plane, the differential cross-section, $\frac{d\sigma}{d\Omega}$ can be expressed as:

$$\frac{d\sigma^{\perp\perp}_{imn}}{d\Omega}(\nu_{imn}) = (2\pi)^4\nu^4_{imn}(2J_n+1)\cdot\left[\begin{pmatrix} J_n & 0 & J_m \\ 0 & 0 & 0 \end{pmatrix}^2 |\langle m|\alpha|n\rangle|^2 + \frac{4}{45}\begin{pmatrix} J_n & 2 & J_m \\ 0 & 0 & 0 \end{pmatrix}^2 |\langle m|\gamma|n\rangle|^2\right] \tag{4.18}$$

where m and n represent the initial and finial energy states of the molecule, ν_{imn} is the frequency of the scattered photons, and the matrices are the Wigner 3-j symbols [6]. The $|\langle m|\alpha|n\rangle|$ and $|\langle m|\gamma|n\rangle|$ are the reduced matrices of the mean polarizabilty and polarizability anisotropy respectively in Eqautions 4.19 and 4.20 using the eigenfunctions, $\langle m|$ and $|n\rangle$ of the radial parts of the Hamiltonian.

$$|\langle m|\alpha|n\rangle| = \begin{cases} \alpha_0^2 & \text{when } v_m = v_n \\ \frac{h}{8\pi^2\mu\omega_e}\alpha'^2 \cdot (v_m + 1) & \text{when } v_m + 1 = v_n \\ \frac{h}{8\pi^2\mu\omega_e}\alpha'^2 \cdot v_m & \text{when } v_m - 1 = v_n \end{cases} \tag{4.19}$$

$$|\langle m|\gamma|n\rangle| = \begin{cases} \gamma_0^2 & \text{when } v_m = v_n \\ \frac{h}{8\pi^2\mu\omega_e}\gamma'^2 \cdot (v_m + 1) & \text{when } v_m + 1 = v_n \\ \frac{h}{8\pi^2\mu\omega_e}\gamma'^2 \cdot v_m & \text{when } v_m - 1 = v_n \end{cases} \tag{4.20}$$

In the above equations, α_0 symbolizes the mean polarizability, and its derivative is α'. The polarizability anisotropy is represented as γ_0, and its derivative is γ'. Furthermore, these equations demonstrate that Rayliegh scattering is an outcome of the static terms (α_0 and γ_0) and Stokes Raman ($v_m + 1 = v_n$) and anti-Stokes Raman scattering ($v_m - 1 = v_n$) are contributions of only the derivatives (α' and γ'). Thus, the Rayleigh signal are stronger than the Raman signals because the static terms are generally three order of magnitudes bigger than the derivatives [53].

4.4 Line broadening

Thus far, the energy conservation in Equation 3.4 has been considered under an assumption that the incident and scattered photons have an infinitely narrow wavelength range. This means their energies are approximately unique to one wavelength value (monochromatic). However, the wavelength range of the incident and scattered photons actually have a finite line-width. This phenomenon called *line broadening*, occurs due to the measurement equipment and other fundamental processes [5]. The dominant causes of line broadening in Raman spectroscopy are discussed in this section of the thesis.

When the source of light is moving at a non-zero speed relative to an observer, the perceived frequency by that observer is different from the actual frequency of light [62]. This *Doppler effect* give rise to the different frequency expressed as:

$$\nu = \nu_0(1 - v/c) \tag{4.21}$$

where ν_0 is the frequency of light in the rest frame of the source, v is the velocity of light source relative to the observer, and c is the speed of light. It is vital to note that v is taken as positive if the source and observer move away from each other.

The velocity of the molecules with mass m in a gas at thermal equilibrium can be evaluated using the *Maxwell distribution*:

$$f(\overrightarrow{v})d^3v = Cexp\left[-\frac{\frac{1}{2}m(\overrightarrow{v} - \overrightarrow{v_0})^2}{k_BT}\right]d^3v \tag{4.22}$$

in which $f(\overrightarrow{v})$ denotes the probability of the finding molecules with a velocity in the 3D interval, $[\overrightarrow{v}, \overrightarrow{v} + d\overrightarrow{v}]$. The normalized proportionality constant is represented as C, and $\overrightarrow{v_0}$ is a possible macroscopic flow velocity. Since the perceived frequency ν, varies linearly with the relative velocity, v, the resulting broadening acquires a similar functional term as the Maxwell distribution. Hence, the distribution of the perceived frequencies leads to a *Gaussian or Doppler lineshape function*:

$$\phi(\nu) = \frac{2}{\Delta\nu_D}\left(\frac{\ln 2}{\pi}\right)^{1/2} exp\left\{-4\ \ln(2) \cdot \left(\frac{\nu - \nu_0}{\Delta\nu_D}\right)^2\right\} \tag{4.23}$$

in which the Doppler linewidth (FWHM), $\Delta\nu_D$ is given by:

$$\Delta\nu_D = \nu_0\left(\frac{8k_BT\ln(2)}{mc^2}\right)^{1/2} \quad . \tag{4.24}$$

The center frequency of the Gaussian profile is denoted as ν_0. Equation 4.24 signifies that the Doppler linewidth is molecule-specific because it depends on molecular mass, m. In addition, it increases with the temperature of the gas.

Pressure broadening is another type of line broadening caused by molecular collisions in gases. For instance, measurements can be performed on a gas at STP, where its density is about $2.5 \cdot 10^{25}$ molecules/m^3 and each molecule undergoes about 10^9 collisions per second with molecules [77]. These collisions give rise to an exchange of internal energies between the molecules. Consequently, the energy levels of the molecules in a gas fluctuate around an average, thereby resulting in an ill-defined position of the energy levels. The lineshape due to molecular collision was first described by the Dutch physicist, Hendrik Lorentz and the resulting shape called the *Lorentzian profile* is expressed as [21]:

$$g(\nu) = \frac{\Delta\nu_c}{2\pi} \frac{1}{(\nu - \nu_0)^2 + (\Delta\nu_c/2)^2} \tag{4.25}$$

in which the center frequency and Lorentzian linewidth (FWHM) are denoted by ν_0 and $\Delta\nu_c$, respectively. Moreover, the Lorentzian linewidth varies linearly with pressure [62].

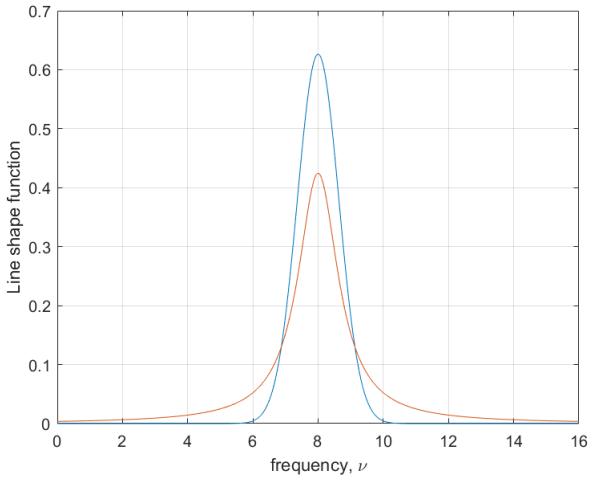

Figure 4.3: Comparison of the Lorentzian and Gaussian lineshapes plotted with the same linewidth (FWHM). These profiles are normalized.

As seen in Figure 4.3, the Lorentzian profile has broader wings than that of the Gaussian distribution derived using the same linewidth (FWHM). Since both profiles in Figure 4.3 are normalised, the Lorentzian profile has a lower maximum point as compared to the Gaussian profile. This ensures the areas under both lineshapes are equivalent.

A more practical cause of line broadening is one due to the measurement equipment and settings. One source of this so-called *instrumental broadening* is the wavelength range of the photons produced by the laser. Each value in the wavelength range would be scattered by the molecules in accordance with Equation 3.4 at slightly different wavelengths. Insufficient resolution of the spectrograph can be another origin of instrumental broadening because it makes the measured spectra broader than it actually is. Regrettably, there is no general lineshape that describes the instrumental broadening related to the measurement equipment [77]. A pragmatic approach is usually employed by implementing a lineshape that best fit the instrumental broadening profile, as it is done in chapter 6 of this report.

Having described all the processes that affect the wavelength of the scattered photons, the intensity of the scattered photons can be quantified in relation to the all parameters stated in this chapter.

4.5 Quantification of Raman signals

The intensity of the Raman scattered light can be expressed as [7]:

$$I_{ram}(\nu) = \sum_{i,m,n} \frac{d\sigma_{imn}}{d\Omega}(\nu_{imn}) \cdot F_{imn}(\nu - \nu_{imn}) \cdot N_{im} \cdot I_0, \tag{4.26}$$

in which $\frac{d\sigma_{imn}}{d\Omega}(\nu_{imn})$ denote the differential scattering cross-section of species i and the quantum states are represented by m and n. The Raman broadening lineshape, number density of molecules at initial quantum state m and intensity of the incident light are symbolized as $F_{imn}(\nu - \nu_{imn})$, N_{im} and I_0 respectively. One essential note is that the intensity evaluated in Equation 4.26 is a function of the wavelength of the scattered photon. However, the Raman intensities are captured using an intensified CCD camera at the different pixel positions. Therefore, Equation 4.26 is converted by Sepman et al. [53] to a pixel-dependent relation written as:

$$I_s(p) = C \cdot \sum_{i,m,n} \left[\frac{d\sigma_{imn}}{d\Omega}(\nu_{imn}) \cdot \epsilon(\nu_{imn}) \cdot \Phi(\nu_r(p) - \nu_{imn}) \cdot \Delta\nu_r(p) \cdot \frac{g_{im} \cdot e^{-\frac{hcE_{im}}{K_B T}}}{Z_i(T)} \cdot \frac{X_i}{T} \right] + I_{bg}(p) \tag{4.27}$$

in which $\epsilon(\nu_{imn})$ is the wavelength-dependent spectral sensitivity of the detection system, $\Phi(\nu_r(p) - \nu_{imn})$ is the lineshape function that estimates to the instrumental broadening, $\nu_r(p)$ is the frequency of the scattered light recorded at p^{th} pixel ($\Delta\nu_r(p) = \nu_r(p+1) - \nu_r(p)$), E_{im} denotes the energy of the initial quantum state and the non-Raman background signal is represented by $I_{bg}(p)$. In the derivation of Equation 4.27, the broadening caused by Raman scattering is neglected using the assumptions that the Raman signals are weak and the detection system has a low resolution [53]. Additionally, the ideal gas law and Boltzmann distribution is used to relate to the number density N_{im} to the molar fraction X_i of species i and temperature, T.

The constants and parameters of the experimental set-up such as incident light intensity of the laser, captured solid angle, distance from the source and length of sampling volume, are included in the coefficient, C labelled the *calibration constant*. By inspecting Equation 4.27, one can see that the calibration constant is independent of the species present in gas mixture. However, Hessels [67] discovered that the calibration constant, C of the experimental setup used in this project varies with the type of scattering molecules. This discovery was made while measuring the Raman spectra obtained from the interaction between a green laser and methane flames using the same detection system utilized in this project. To investigate this contradiction, Hessels [67] compared the actual wavelength-dependent sensitivity that was measured to the sensitivity values specified by the manufacturers of the detection system, which comprises the wavelength-dependent efficiency of spectrograph and CCD camera. As a result, spectral sensitivity obtained from the manufacturers was found to be different from the actual sensitivity measured. This means that the calibration constant, C also incorporates the difference between the sensitivity values specified by the manufacturers and the sensitivity values measured. Therefore, the calibration constant of every species is determined separately in gas mixtures of known composition (molar fractions) and temperature.

In this project, the calibration constants for N_2, O_2 and H_2O are determined using the Raman measurements in air at room temperature (294 K). The molar fractions of N_2 and O_2 in air at this temperature are assumed to be 0.7810 and 0.2095 respectively. These values are obtained from the known composition of N_2 and O_2 in air at room temperature. Additionally, the molar fraction of H_2O are calculated using the relative humidity measured in the air at this temperature. On the other hand, the calibration constants for NH_3 and H_2 are evaluated using the Raman measurements in a gas mixture of ammonia and hydrogen. To compute the molar fractions of NH_3 and H_2, the fluid flow of this mixture is simulated with the aid of a CFD software package called ANSYS. The determination of the calibration constants is thoroughly explained in Appendix A for all the species of interest.

4.6 Polyatomic molecules

Up until now, the analysis of the Raman scattering processes has been illustrated using the quantum-mechanical description of diatomic molecules. Conversely, there are polyatomic molecules such as H_2O and NH_3 present in the flames investigated in this project. In this section, the examination of these molecules will be discussed.

One major hurdle in the illustration of polyatomic molecule is the determination of their energy levels. This is a consequence of the fact that the different contributions to the internal energy can no longer be treated as separate entities. Additionally, the existence of multiple bonds between the individual atoms give rise to multiple vibrational energies characterized by different quantum numbers. Polyatomic molecules can also have multiple rotational energies attributed to different moments of inertia with respect to the principal axes.

For example, NH_3 is a symmetric top molecules with two distinct moments of inertia, one of which is associated with two of the three principal axes of rotation [62]. Hence, NH_3 possesses two unique rotational energies with two quantum numbers (J,K) and their corresponding rotational constants.

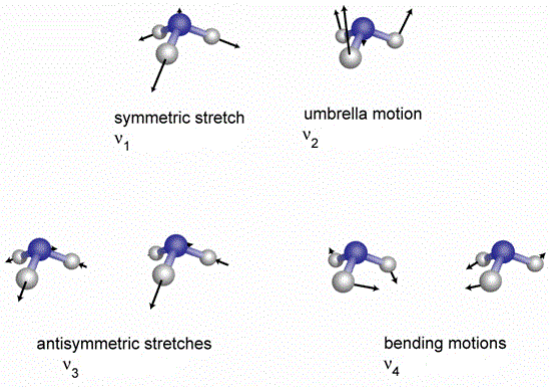

Figure 4.4: Schematic representation of the fundamental vibrational modes of ammonia. The asymmetric stretching (ν_3) and bending (ν_4) modes are double degenerate (retrieved with permission from [33]). All these modes of vibration are Raman active.

There are six fundamental modes of vibration for ammonia [62], as shown in Figure 4.4. Although all these modes are Raman-active, they are not all detected in Raman experiments. The symmetric stretching (ν_1) and bending (ν_2) modes occur when the three hydrogen atoms move simultaneously in the same direction relative to the nitrogen atom. Alternatively, the movement of hydrogen atoms in opposite directions are evident in the asymmetric stretching (ν_3) and bending (ν_4) modes, which are double degenerate. Another vital information in Table 4.1 is the occurrence of two infrared absorption frequencies for the two symmetric modes and two Raman frequencies for the symmetric bending mode of vibration. This is a consequence of a phenomenon called *inversion doubling*, which illustrates the existence of two equilibrium positions for the nitrogen (N) atom at both sides of the plane formed by the three hydrogen (H) atoms of an ammonia molecule [2].

As depicted in Table 4.1, the asymmetric modes of vibration are not visible in Raman experiments because the strength of their intensities are weak [2]. Although it has a medium Raman strength, the symmetric bending (ν_2) mode is not used in this project for the molar fraction determination of NH_3 because its Raman intensities cancel out the when the signal in one polarization configuration is subtracted from the other configuration. This reason for this subtraction is discussed in subsequent chapters. On the other hand, the symmetric stretching (ν_1) mode has a very strong and polarized Raman strength. Thus, the Raman scattering light is only seen at a frequency of 3334.2 cm^{-1} in this research.

Vibration	Infrared frequency (cm^{-1})	Raman frequency (cm^{-1})	Description	Raman strength
ν_1	3335.9 3337.5	3334.2	symmetric stretch	very strong and polarized
ν_2	931.58 968.08	934.0 964.3	symmetric bending	medium
ν_3	3414	-	asymmetric stretch (degenerate)	-
ν_4	1627.5	-	asymmetric bending (degenerate)	-

Table 4.1: Properties of the fundamental vibrational modes of ammonia [2].

Since the contributions to the internal energy of symmetric molecules are inseparable, Equation 4.27 cannot be used to simulate the ro-vibrational Raman spectra of ammonia [2]. Hence, a coarser approach is implemented for quantification of ammonia as it was done by Fuest et al. [57] for acetylene. The working principle of this crude estimation is based on *Placzek's double harmonic approximation* of the potential function and polarizability [27]. This approximation assumes the vibrational bond to be the main cause of the apparent Raman shift, thereby neglecting the rotational energy levels of the molecule. One derivative of this approximation is the temperature-dependent Raman cross-section given as follows:

$$\frac{d\sigma}{d\Omega} = \frac{h(\nu_0 - \nu_R)^4(\alpha'^2 + \frac{4}{45}\gamma'^2)}{8mc^4\nu_R(1 - e^{-h\omega_e/k_BT})}, \tag{4.28}$$

in which ν_0 is the frequency of the incident photon and ω_e is the bond-specific equilibrium frequency that is equal to 3334.2 cm^{-1} for the visible vibrational band of ammonia in this project. Given that this cross-section is proportional to Raman signals, the molar fraction of ammonia can be expressed at a particular temperature using Equation 4.28 as:

$$X = \frac{S_Q(T)}{S_Q(T_0)} \cdot \frac{(1 - e^{-h\omega_e/k_BT})}{(1 - e^{-h\omega_e/k_BT_0})} \cdot \frac{T}{T_0} \cdot X_0, \tag{4.29}$$

where $S_Q(T)$ is the integrated Raman signal at temperature, T and $S_Q(T_0)$ is the integrated Raman signal at a known reference temperate, T_0. The corresponding reference molar fraction is denoted as X_0.

Although H_2O is a polyatomic molecule, its Raman spectra can be simulated using Equation 4.27 and the compiled tables obtained from the experimental analysis performed by Avira et al. [29, 30]. This is possible because the tables contain the information (internal energy levels, possible transitions, scattering cross sections and the partition function) needed to model the Raman spectra of water molecules.

Now, all the equations required to quantify Raman scattering data have been provided. How this data from experiments were obtained will be described in the next chapter.

Chapter 5

Experimental setup

The experiment setup used in this project is discussed in this chapter. The factors affecting the selection of the optical equipment are first outlined in the detail. Secondly, the burner system used to light the flames are illustrated. Then, the laser set-up used to probe these flames is explained as well as the detection system used to record the resulting Raman signals. Finally, the experimental procedure implemented to accurately obtain quantitative data is described.

5.1 Factors influencing the selection of optical equipment

Raman experiments are carried using four major components: spectrograph, laser, notch filter, and CCD detector. The laser emits photons that are scattered by the molecules investigated, whereas the optical filter removes the Rayleigh scattered light. Then, the Raman scattered light left is dispersed into a range of wavelengths (colors) at different angles by the spectrograph, before it is captured at separate locations on the CCD detector. To obtain optimum experimental data, these components need to be carefully selected based on factors affecting their performance.

Following the discussion in section 4.3, one can infer that the Raman cross-sections for scattered light, expressed in Equation 4.17 and 4.18, scale with frequency to the fourth power. This means the signal strength of light scattered by short-wavelength (high-frequency) lasers is higher than that of light scattered by long-wavelength lasers. However, there is a high tendency for the occurence of Laser-induced Fluorescence (LIF) if a short-wavelength laser is used [78]. This is because short-wavelength lasers emit high-energy photons that can be resonant with an allowed transitions for one of the species in the medium. Moreover, the fluorescent signals, which are significantly more efficient, may bury the Raman signals caused by other species in the medium. On the contrary, long-wavelength lasers generate higher amount of heat that may change the properties of the probed medium through vaporization of some species or temperature increase [97]. This interference by long-wavelength lasers implies that there is a deviation from the minimal intrusiveness of laser-based diagnostics. Additionally, the sensitivity of the CCD detectors are generally low at longer wavelengths of light [97].

	shorter wavelength $\longleftarrow$	longer wavelength $\longrightarrow$
Raman signal strength	✓	×
fluorescence	×	✓
Heat	✓	×
Detector sensitivity	✓	×

Table 5.1: Factors influencing the wavelength selection of the laser used in Raman experiments. The checkmark symbol (✓) signifies positive effect while the cross symbol (×) denotes a negative effect.

To sum up, the wavelength of the laser needs to be optimally selected for Raman measurements in a way that the negative effect of the three factors shown in Table 5.1 are as minimal as possible.

The most commonly used laser wavelengths in Raman experiments are 785 nm (near infrared) and 532 nm (green), which offer high signal strength, little to no fluorescence and minimal heat for a wide range of species [97].

The CCD image sensor is basically a one- or two-dimensional array of photosensitive capacitors that convert incident light to electric charges [77]. Each of these capacitors are picture elements called *pixels*, which collect charges proportional to the intensity of incident light. Furthermore, the Quantum efficiency (QE) is the parameter used to quantify effectiveness of the light-to-charge conversion, and the CCD detectors, manufactured in recent times, have reached QEs of $70 - 90\%$ [77]. The Signal-to-noise ratio (SNR) of CCD detector is another parameter that is important in Raman experiments. It is a measure of how distinct the Raman signals are from the detector noise [62]. CCD detectors with high SNRs are selected to ensure the Raman signals are not dwarfed by the detector noise.

The entrance slit and grating mirror are the two vital components of a spectrograph that influences its performance. Raman scattered photons enter the spectrograph through the entrance slit before they are sorted into different wavelengths by the grating mirror. The width of this slit is the variable that influences the resolution of the Raman spectra. Better resolution is achieved when the entrance slit width is reduced. This means the use of a narrower entrance slits results in more resolved Raman spectra and vice versa [97]. Unfortunately, less signal is received by the spectrograph as the entrance slit becomes narrower. Thus, an optimum width of the entrance slit is selected such that adequate Raman signals are detected and resolution is sufficient to capture the details of the Raman spectra.

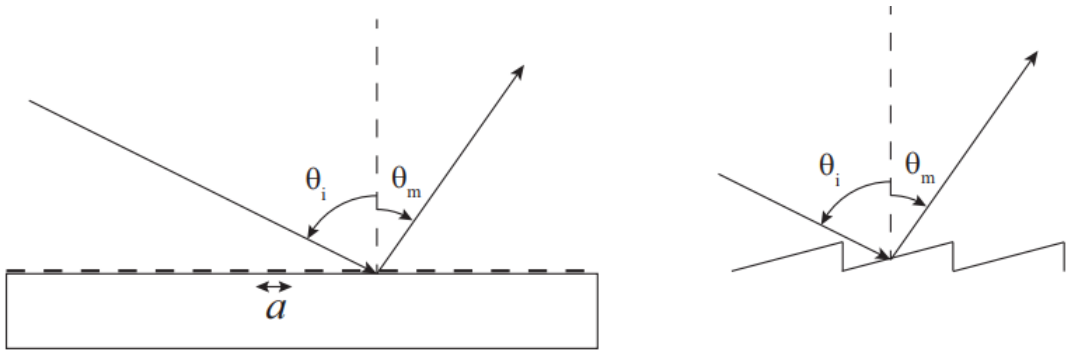

Figure 5.1: Definition of the incidence and reflection angles on a reflection grating. A surface detail of a blazed grating is shown to the right (retrieved with permission from [77]).

As pictorially represented in Figure 5.1, the grating mirror is essentially a group of small mirrors formed by creating shallow scratches (*grooves*) on a large reflective surface. These grooves can be made on a flat but a sawtooth-like pattern is used in more advanced designs called *blazed gratings*. Monochromatic light is reflected into distinct directions by each of the small mirrors when it strikes the grating mirror. Then, the combination of all these reflected rays of light will create an angle at which constructive interference occurs [31]. This illustration of constructive interference is a phenomenon called *diffraction*, and the direction of the diffracted light is given by the *grating equation* [31] in terms of the incidence angle, θ_i and reflection angle, θ_m:

$$\pm\, mG\lambda = \sin\theta_m - \sin\theta_i, \tag{5.1}$$

where $G = 1/a$ is the groove density expressed in "grooves/mm", a is the groove distance, and λ is the wavelength of the diffracted light. The integer, m is the *diffraction order* of the grating mirror, which has a value of 0 for a regular mirror with no grooves. Equation 5.1 implies that the reflection angle (θ_m) will increases if there is an increment in groove density (G) for constant value of θ_i. Hence, grating mirrors with higher groove density give rise to high-resolution measurements

because every wavelength of light is further apart from each other. A consequence of this advantage is the reduced wavelength range of light captured by the CCD detector. This is because some of the Raman scattered light will be diffracted at a reflection angle (θ_m) that is beyond the width of CCD detector depending on their wavelengths. To circumvent this problem, the wavelength range can be altered by rotating the grating mirror about its axis, thus changing θ_i. This allows for the variation of spectral range in Raman experiments. Conclusively, grating mirrors with low G are used to capture full Raman spectra that holds the information of all possible species present in a medium. However, grating mirrors with high G are utilized to obtain more detailed spectra within a small wavelength range that is attributed to one or two species.

In conclusion, the variables that should be addressed while choosing optical equipment have been taken into consideration. The selected optical apparatus can now be discussed in detail. Before doing that, the co-flow burner system is discussed in the next section of this chapter.

5.2 Burner system

An existing coflow burner setup that was created by Oliveira [51] and subsequently optimized for Raman spectroscopy by Doddema [74] is used for the experiments in this project. This burner is used to create laminar non-premixed $NH_3/H_2/N_2$ flames that are symmetric around the axis of the fuel stream. Moreover, Hessels [67] previously utilized this setup for the quantitative analysis of the flames generated by hydrocarbon-based fuels. As shown in Figure 5.2a, the coflow burner setup comprises a burner in which the fuel and oxidizer are delivered, a high-pressure vessel, and a chimney through which the exhaust gases leave.

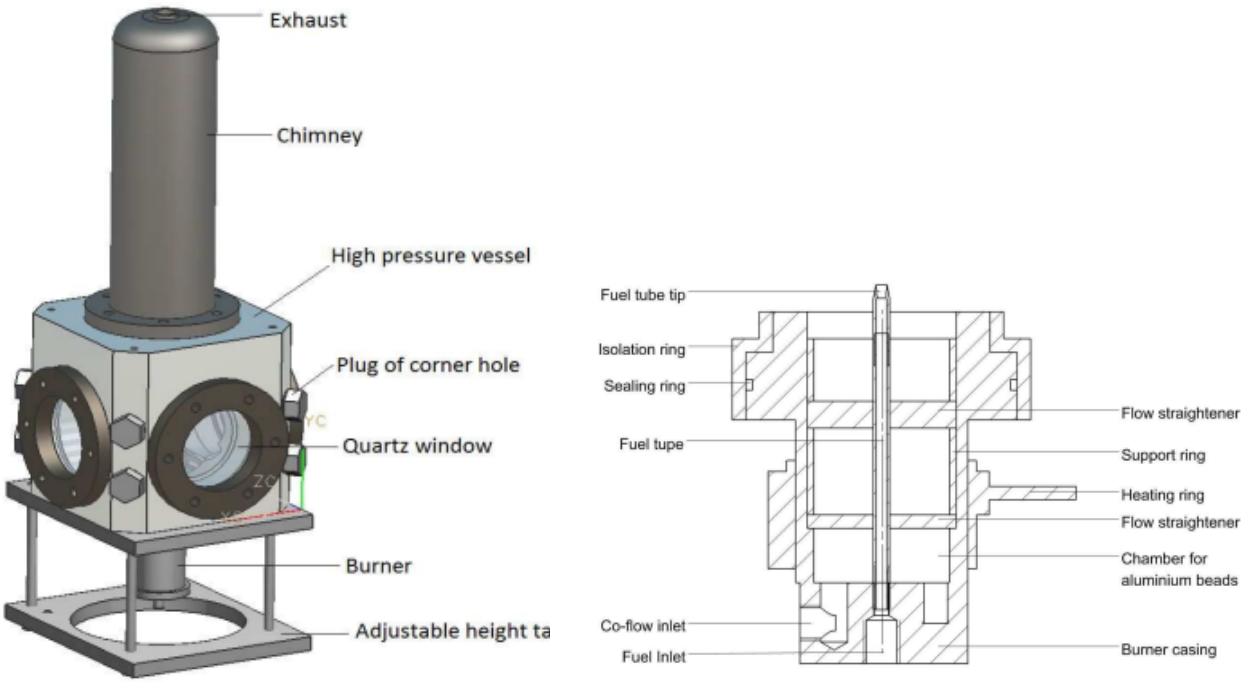

(a) Burner vessel **(b)** 2D cross-section of burner

Figure 5.2: Detailed assembly of computer-aided design of burner setup and schematic layout of the burner. The coflow enters from the side and, in order to produce a uniform flow profile, flows first through a bed of aluminum beads before passing through a perforated plate [51].

The 2D cross-section of the burner is depicted in Figure 5.2b, shows that the fuel and coflow enter the high-pressure vesssel as separate flows. Additionally, there are a pair of flow straighteners in the burner to generate a uniform profile of coflow. The inner and outer diameters of the fuel tube are 4 mm and 6 mm, respectively. The high-pressure vessel is a steel compartment that has a 200-mm cubic shape, and cylindrical tunnels with a diameter of 100 mm are drilled on three of its sides. Quartz windows are inserted into these holes to provide optical access to the vessel.

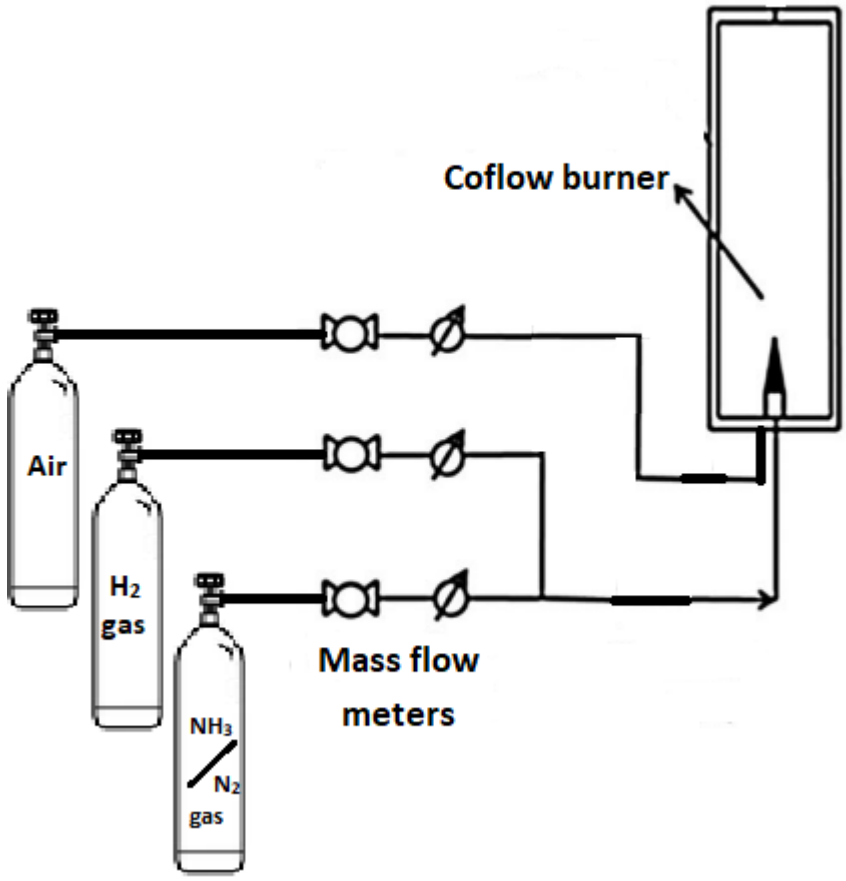

Figure 5.3: Schematic illustration of how the gas bottles to the coflow burner system using stainless steel tubing. The flow rates of the gases are controlled using Bronkhorst EL-FLOW Select mass flow meters [85].

At the preparation phase of this project, an ammonia/hydrogen gas mixture, stored in a gas bottle, was initially planned for use as fuel. Unfortunately, the gas manufacturing company (Linde Gas Benelux) made an error and instead produced and shipped a gas bottle containing an ammonia/nitrogen gas mixture. This mistake could not be reversed because the gas bottle arrived very late during the period of the eight months dedicated to this project . To rectify this problem, the ammonia and hydrogen gases are transported to the coflow burner by using a blend of the ammonia/nitrogen gas mixture (containing 4.457% NH_3) delivered and pure hydrogen gas, as shown symbolically in Figure 5.3. The flow rates of the fuel blend and coflow (air) are controlled using Bronkhorst EL-FLOW Select mass flow meters [85], calibrated on a Bronkhorst mass flow meter calibration setup. However, the mass flow meters, designed for methane (CH_4)

and Dimethylether (C_2H_6O) gases, are employed to control the flowrates of the hydrogen gas and ammonia/nitrogen gas mixture, respectively. For this reason, conversion factors are calculated using Bronkhorst FLUIDAT® software [84] and used convert readings on those mass flow meters to the equivalent flow rates of ammonia/nitrogen gas mixture and hydrogen gas.

5.3 Optical setup

a Photonics Industries DM20-527 Nd:YLF laser is used for the Raman experiments in this project because it produces adequate signal strength and its photon energy is non-resonant to most of the species that can induce fluorescence. This laser produces green light at 527 nm, which has an average power of 30 W at 3 kHz repetition rate and a pulse duration of 170 ns at 1 kHz repetition rate [92]. In addition, the exiting laser beam is polarized vertically at a 100:1 ratio. Because of the long pulse duration of this laser, the energy density is quite low. As a result, the laser beam can be focused down a narrow probe volume without ionizing the air in the burner vessel. To enable the rotation of this polarization, the laser light first passes through a Thorlabs half-wave plate [95]. By performing a 45° rotation of this wave-plate, it can quickly switch the optical set-up between configurations where the laser beam is parallel and perpendicular to the scatter plane defined in section 4.3. However, the efficiency of this half wave-plate somewhat reduced when used to change the polarization of a 527-nm light because it is optimized for 532 nm, but there were no 527-nm half-wave plates available. Secondly, the beam is redirected with the aid of two 45° HR 532-nm mirrors before it goes through an uncoated lens with a 1000-mm focal length. The beam is focused at the flame location using this lens. Then, another 45° HR 532-nm mirror is used to redirect the beam towards the fuel tube inlet. Afterwards, the laser beam enters the burner vessel through a Thorlabs WL11050-C10 523 - 532-nm anti-reflection window [96] installed at the bottom of the fuel tube. Finally, a beam dump is employed to capture the laser beam leaving the burner vessel through the exhaust. A block diagram of this beam pathway is provided in Figure 5.4, which implies that Raman signals can be detected along the symmetry axis of the flame in one measurement.

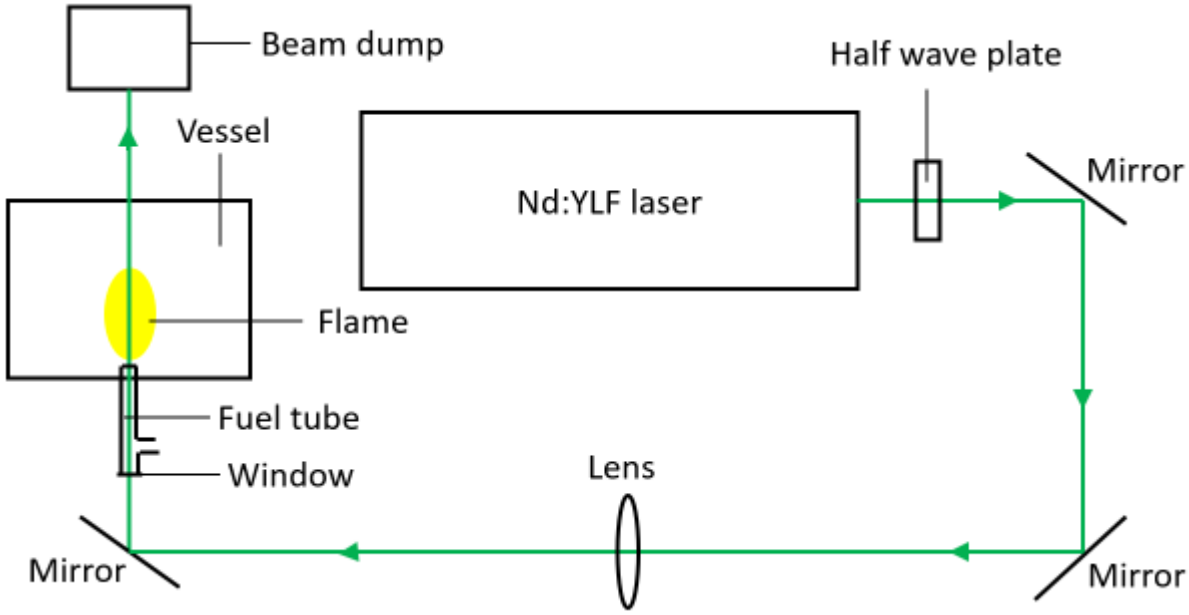

Figure 5.4: A schematic layout of the laser beam pathway. The mirrors and half-wave plate are optimized for 532-nm light, and the lens is uncoated. The bottom window of the fuel tube is anti-reflective.

A Princeton Instruments Acton SP-500i spectrograph [93], with a 500-mm focal length is positioned perpendicular to the direction of the laser beam and aligned with one of the quartz windows of the burner vessel in order to collect and disperse the scattered light. There are three different grating mirrors in this spectrograph: two 500-nm blazed gratings with groove densities (G) of 300 and 1200 grooves/mm and a HVIS holographic grating mirror with a 2400-grooves/mm groove density. The 1200-grooves/mm grating mirror is utilized for all the Raman experiments in this project because it gave rise to the best spectral sensitivity. Additionally, a Nikon f/2 camera lens with a 105-mm focal length [89] is placed on the entrance slit of the spectrograph to focus the flame location on the entrance slit. An Edmund Optics OD4 532 nm notch filter with a FWHM of 26.6 nm [86] is fitted to this camera lens, and it used to block Rayleigh scattering. The width of the entrance slit is set approximately to 100 μm and oriented parallel to the path of the laser beam. This optimum width is chosen because it results in sufficiently resolved Raman spectra with adequate signal strength.

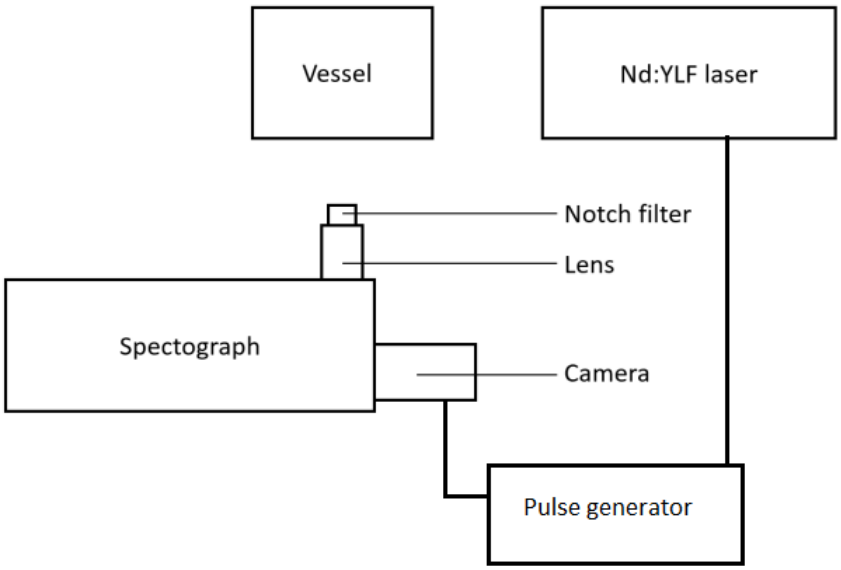

Figure 5.5: A schematic view of the detection system. The pulse generator used to synchronize the camera and laser.

An intensified 1024×1024-pixels CCD camera (Princeton Instruments PI-MAX 3, Filmless UniGen II intensifier) [94] is installed at the exit plane of the spectrograph and utilized for detecting and recording Raman scattered light. In addition, a pulse generator (Standford research systems model DG535) [68] is employed to synchronize the CCD camera and laser. This synchronization is performed to capture time-gated Raman signals at a width of 200 ns. These signals are received by a computer connected to the camera in the form of an intensity matrix that is later post-processed. The arrangement and positions of all the equipment in the optical setup is visualized in Figure 5.6.

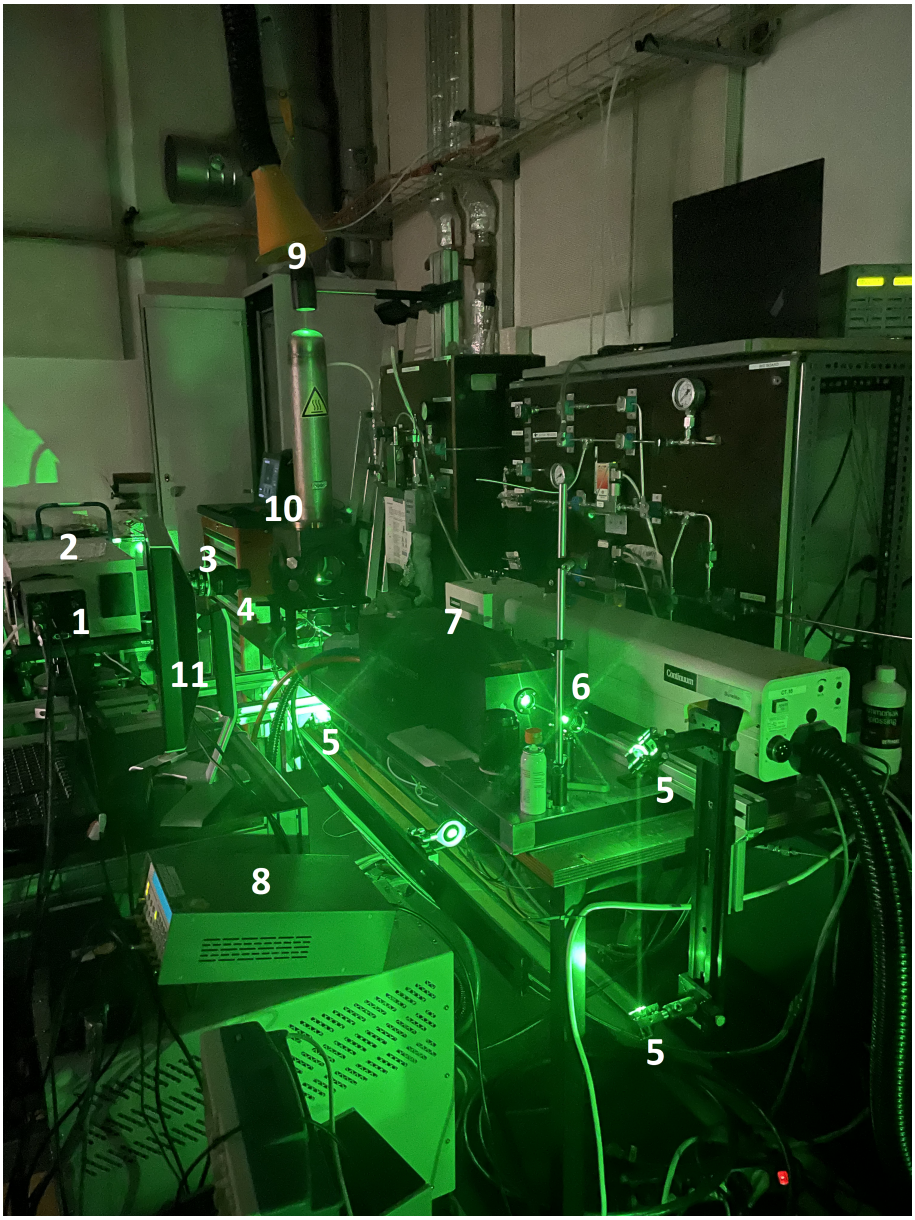

Figure 5.6: An image of the optical setup and burner vessel (10). The components of the optical setup are labelled with numbers: 1 intensified CCD camera, 2 spectograph, 3 Nikon camera lens, 4 Notch filter, 5 45 °mirrors, 6 half-wave plate, 7 laser, 8 pulse generator, 9 beam dump. The computer used to visualize the recorded spectra is indicated as number 11. The green illumination all over the setup is provided by stray light from the laser beam.

5.4 Experimental Procedure

Certain measures are implemented to ensure accurate acquisition of measurement data and minimization of many disturbances that could contribute systematic errors in measurement. Firstly, the laser beam is aligned to the centre of the entrance slit before every measurement is performed. This is done while the slit is opened completely and the spectrograph is in mirror mode. Afterwards, the entrance slit width is reduced to the optimum value of 100 μm. To describe the next procedure, the two polarization configurations used in this project are defined as follows:

- *perpendicular-perpendicular* configuration denotes the laser and Raman scattered light both polarized perpendicular to the scatter plane.
- *parallel-perpendicular* configuration signifies the laser and Raman scattered light polarized parallel and perpendicular to the scatter plane, respectively.

The Raman measurements are taken in both polarization configurations and the recorded signal in the parallel-perpendicular configuration is subtracted from that of the perpendicular-perpendicular configuration. This subtraction is used to remove the non-background signal seen in the Raman spectra measured in this project. Moreover, it also reduced the amount of the Raman signal detected. Hence, the quantification of this reduced signal is determined by using a different formulation of the differential cross-section in Equation 4.27. Since the differential cross-section is the only parameter in the signal quantification dependent on polarization, its expression for the reduced signal is equivalent to the difference between the polarization-dependent differential cross-sections given by Equations 4.17 and 4.18, which is expressed below:

$$\frac{d\sigma_{imn}^{\perp\perp-\parallel\perp}}{d\Omega}(\nu_{imn}) = (2\pi)^4 \nu_{imn}^4 (2J_n+1) \cdot \left[\begin{pmatrix} J_n & 0 & J_m \\ 0 & 0 & 0 \end{pmatrix}^2 |\langle m|\alpha|n\rangle|^2 + \frac{1}{45} \begin{pmatrix} J_n & 2 & J_m \\ 0 & 0 & 0 \end{pmatrix}^2 |\langle m|\gamma|n\rangle|^2 \right] \quad (5.2)$$

where the parameter, $\frac{d\sigma_{imn}^{\perp\perp-\parallel\perp}}{d\Omega}(\nu_{imn})$ is the differential cross-section used for the quantification of the reduced signal.

Additionally, the Raman spectra of nitrogen in air at room temperature is measured with perpendicular-perpendicular configuration on each measurement day to account for variations in the efficiency of the setup, and the results are used to adjust the calibration coefficient, C in Equation 4.27. Finally, the flame is ignited for at least 30 minutes before Raman measurements are carried out to ensure that thermal equilibrium is reached and the flow constituting the fuel, oxidizer and gas byproducts attained stability.

To sum up, these steps are taken in the outlined order to obtain the measured Raman spectra that further undergo post-processing. The methods applied to post-process the Raman spectra are discussed in the next chapter.

Chapter 6

Data analysis

The first topic covered in this chapter relates to the techniques used for post-processing the Raman spectra measured in this project. Then, the method for determining the molar fractions and temperatures from the observed Raman spectra is then described. Finally, the estimation of the errors in the ascertained temperatures and molar fractions is examined.

6.1 Image processing

Since the vertical position of the image recorded by the intensified CCD camera is given in pixels, a height calibration is needed to obtain the equivalent position in millimeters (mm). This is performed by taking image of a stainless steel ruler positioned above fuel tube tip of the burner shown in Figure 5.2. As illustrated in Figure 6.1, the resulting image is captured using the grating of the spectrograph in mirror mode and the maximum size of the entrance slit. Accordingly, the rows of the intensity matrix visualized in this image represent the pixel position along the vertical direction. Hence, the pixel-to-millimeters relation is determined by dividing the difference in the pixel positions of the 1-cm (10-mm) and 2-cm (20-mm) lines on the ruler by the corresponding height difference of 10 mm. The outcome of this calculation is a height difference of 0.0268 mm between two adjacent pixels along the vertical direction. Hence, the height resolution of the images captured by the intensified CCD camera is equal to 0.0268 mm. Using this value, the the pixel-to-millimeters relation can be expressed as:

$$h(p) = h_1 + 0.0268(p - 1) \tag{6.1}$$

where h_1 corresponds to the millimeter equivalence of the bottom row of the image intensity matrix of the ruler. This parameter(h_1) also denotes the height difference between the fuel tube tip and bottom edge of the spectrograph's entrance slit. The parameter, p is pixel position of the p_{th} row of the intensity matrix.

In addition to the wavelength-dependent sensitivity mentioned in chapter 4, CCD cameras possess a pixel-to-pixel sensitivity variations. A so-called flat field correction is applied to the raw images recorded by the camera to account for these variations. This correction is carried out by utilizing an image obtained from the projection of the same amount of light on every pixel to rectify the signal variance between the pixels. The corrected image, $S_{\text{polarised}}$ is evaluated using Equation 6.2:

$$S_{\text{polarised}} = \frac{R_{\perp\perp} - R_{\parallel\perp}}{F - D} \cdot \bar{l}, \tag{6.2}$$

where F is the flat-field image, D is the dark frame and $\bar{l}$ is the image-averaged pixel value of $(F - D)$. The dark frame is an image captured with the same exposure time and gain settings as the flat-field image, but without incident light hitting the CCD. The flat-field image is determined in this project by sweeping the Rayleigh line of air across every pixel of the intensified CCD. This sweep is executed while the spectrograph is operated in a scanning mode where the grating mirror is rotated slowly at a constant speed of 30 nm/min from a center wavelength of 510 nm to 540 nm, and the notch filter is detached from the camera lens. This rotation at constant speed assumes that the same amount of light (Rayleigh line of air) projected on each pixel is

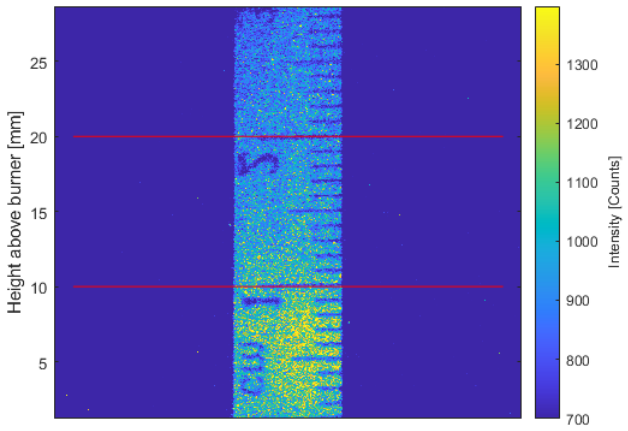

Figure 6.1: The image of the ruler placed above fuel tube tip. The intensities of this image are illustrated using pseudo-colors. The red lines represent pixel positions of the 1-cm (10-mm) and 2-cm (20-mm) lines on the ruler.

equal. The images recorded using the perpendicular-perpendicular and parallel-perpendicular polarization configuration are denoted by $R_{\perp\perp}$ and $R_{\parallel\perp}$, respectively. In Equation 6.2, $R_{\parallel\perp}$ image is subtracted from $R_{\perp\perp}$ to remove most of non-polarized background signal, thereby leaving an image comprising the polarized Raman signal and random noise.

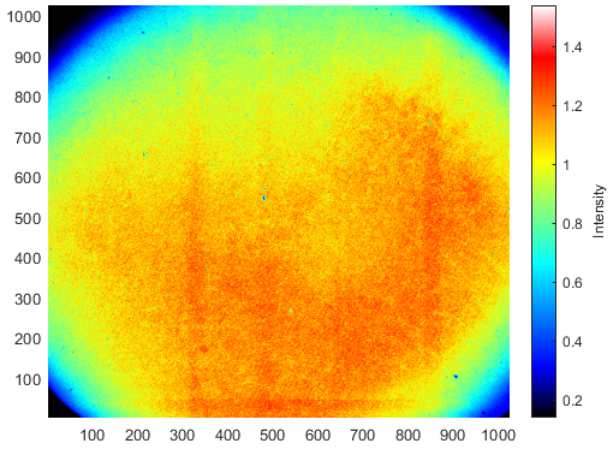

Figure 6.2: Flat-field image ($\frac{F-D}{m}$) obtained by sweeping of the Rayleigh line of air over the CCD with a constant speed of 30 nm/min from a center wavelength of 510 nm to 540 nm.

The averaged background-corrected flat-field image ($\frac{F-D}{m}$) is visualized in Figure 6.2. The low intensities at the four corners of this image are caused by the circular shape of the camera lens used to focus the flame location on the CCD. Additionally, there are some low-intensity (blue) dots in Figure 6.2 signifying dead pixels that are not responsive to incident light.

To remove the outliers in the measured Raman signals, a Hampel filter is applied on the recorded images. This filter is a generalisation of the common median filter with an additional tuning parameter, t and it can expressed as follows [64]:

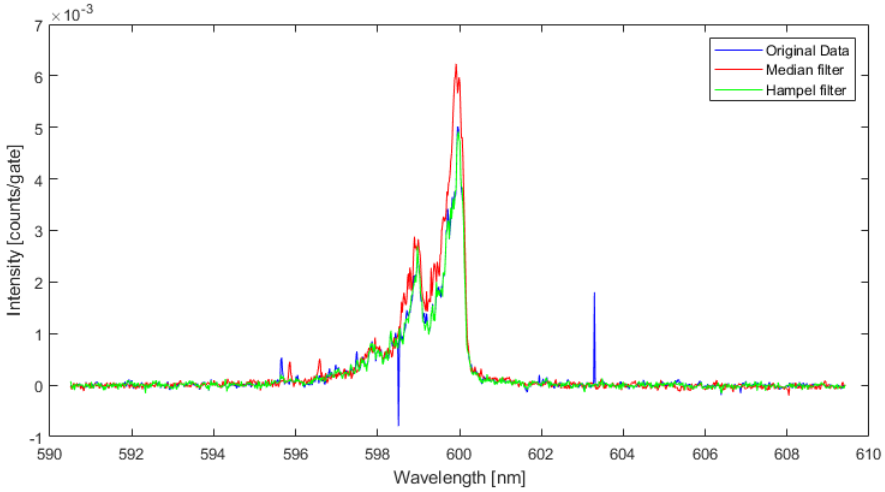

Figure 6.3: The effect of the median filter and Hampel filter (t=3) on one of the measured Raman spectrum of nitrogen. This image infers that the hampel filter only removes the outliers, whereas the median filter modifies almost all the values of the Raman signal.

$$y_k = \begin{cases} x_k & \text{when } |x_k - m_k| \leq t \cdot s_k \\ m_k & \text{when } |x_k - m_k| \geq t \cdot s_k \end{cases} \tag{6.3}$$

in which y_k is the filtered image, x_k is the raw value of the image intensity of a pixel, m_k is the median value of intensity in a specific window around that pixel and s_k is the estimate of the standard deviation in the window based on the median absolute deviation. An optimum window containing nine intensity values, with x_k at center, is used for the Hampel filter in this project. The aggressiveness of this filter is determined by the value of the parameter t, with $t = 0$ indicating a true median filter and $t = \infty$ indicating no filtering of the data. By varying this parameter, a Hampel filter with value of $t = 3$ is found to be minimally aggressive because it removes the outliers without significantly changing the original signal. For example, the aggressiveness of this filter on one of the Raman spectrum of nitrogen measured in this project is illustrated in Figure 6.3. The median filter ($t = 0$) is also implemented on the same spectrum in this figure, which demonstrates that the median filter considerably modifies the original data.

To decrease noise, the spectral images are averaged over rows of 10 pixels in the spatial dimension representing the height above the fuel tube tip. Although this binning decreases the height resolution from a value of 0.0268 mm to 0.268 mm, it also lessens the impact of noise on the Raman signal. This noise reduction technique is widely utilized for Raman spectroscopy [32, 36, 53, 57].

In conclusion, the result of all these corrections is an image consisting a background signal of pure random noise and the polarized Raman signal of the species present in the flames.

6.2 Model fitting

To determine the temperature and molar fractions, the simulated spectra derived using the equations discussed in chapter 4 are fitted on the measured spectra. This fitting is performed with codes written in MATLAB. Firstly, the partition function of all possible energy states of the investigated molecules are acquired from the NIST database [81]. Then, the molecular constants of these states, listed in Appendix B, are implemented in equations 4.1, 4.5, and 4.9. However, a limited number of these states are considered for the simulation of the Raman spectra. This limitation is used by considering only the populated energy states that significantly affect the

simulated spectra. As a result, the computational time taken to find the simulated spectra that best fits to the measured spectra, is reduced. To determine this limit, Hessels [67] investigated all possible energy states by evaluating how influential their population ratios, defined with respect to most populated state, are on the temperature determined using Equation 4.14. Since it is the maximum probable temperature in the flame studied in this project, 2000 K is used as the reference temperature for this investigation. As a consequence, Hessels [67] discovered the energy states with population ratios of more than 10^{-5} considerably influence the simulated spectra. Thus, this set of the energy states are taken into account in this project when fitting the simulated spectra.

Furthermore, the probable transitions are computed for Stokes ro-vibrational Raman scattering employing the selection rules outlined in equations 4.10 and 4.11. Using equations 4.17 and 4.18, the scattering cross sections for these transitions are calculated. Hence, the Raman spectrum of a species (or combination of species) at any temperature for a specific wavelength range can be simulated by combining these cross sections with the parameters of the detection system and adding up the contributions of the individual transitions. Additionally, the algorithm developed by Klaus [87] is applied for the calculation of the Wigner 3-j symbols in equations 4.17 and 4.18. A linear equation ($I_{bg}(p) = a \cdot p + b$) is then used to estimate the background signal, as executed by Sepman et al [53].

To work out the instrumental broadening function (Equation 4.21) of the experimental setup, a Gaussian distribution is fitted on the Rayleigh line of air using the 527-nm laser. The fitting is done on the Rayleigh line at a given height above burner. An example of this is illustrated in Figure 6.4a at height of 24.86 mm and the corresponding FWHM of the Gaussian fit is 0.1772 nm. The width (FWHM) variation along the captured height is visualized in Figure 6.4b, which indicates that the Rayleigh line has a minimum width of 0.16757 nm at 15.48-mm height. This minimum position represents the point where the laser beam is most focused by the lens in the optical setup, provided that the entrance slit width is along its height. This condition is placed as the increase in slit width broadens the Rayleigh of air and vice-versa. From the ruler image provided in fig. 6.1, we can see that the entrance slit width is approximately constant along its height. It is also evident from Figure 6.4b that the width increases as one moves further away from this minimum position.

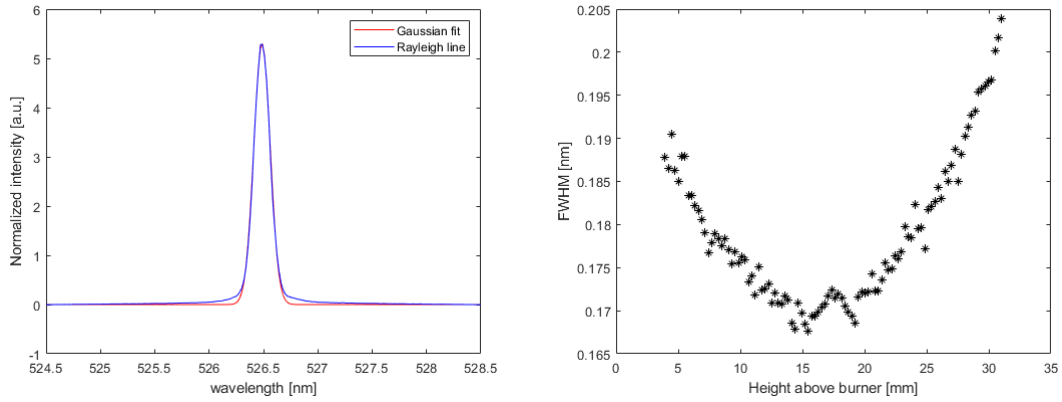

(a) Gaussian fit at height of 24.86 mm.

(b) Width variation of the Rayleigh line

Figure 6.4: Gaussian fit of the Rayleigh line of air by the 527-nm laser. The variation of its width (FWHM) approximately possesses a parabolic shape with a minimum width of 0.16757 nm at 15.48-mm height.

The measured and simulated spectra are analyzed to identify the parameters that affect their shape and size. By doing this analysis, one will recognize the fitting variables needed for the temperature and molar fractions determination. The Raman intensity expressed in Equation 4.27

can also be written as:

$$I_s(p) = C \sum_i f_i(p,T) \cdot \frac{X_i}{T} + I_{bg}(p) \tag{6.4}$$

where $f_i(p,T)$ consists of the polarization-dependent cross-section of species i, the instrumental broadening and efficiencies of the experimental setup, and the Boltzmann distribution of the species i over its energy levels. The parameter $f_i(p,T)$ solely varies with pixel position p and temperature T since the instrumental broadening lineshape, and the efficiencies of the experimental setup are known. The Raman spectra in each wavelength range can be assumed to be the consequence of only the species causing Raman scattering if the wavelength ranges of the Raman spectra attributed to each species are further apart. Hence, the Raman intensity $I_s^i(p)$, in the wavelength range associated with one species, can be expressed as:

$$I_s^i(p) = C f_i(p,T) \cdot \frac{X_i}{T} + I_{bg}^i(p) \tag{6.5}$$

where $I_{bg}^i(p)$ denotes the background signal in this wavelength range. The intensity expression in Equation 6.5 can be rearranged and divided by its maximum value, which results to:

$$\frac{I_s^i(p) - I_{bg}^i(p)}{I_{max} - I_{bg}^i(p^{max})} = \frac{f_i(p,T)}{f_i(p^{max},T)} \tag{6.6}$$

in which p^{max} is the pixel position where the Raman intensity is maximum, and I_{max} is the maximum Raman intensity. The expression at the right side of Equation 6.6 is simply another function of p and T. Hence, this expression can be given by $\varphi_i(p,T)$. Then, Equation 6.6 can be rearranged to the equation below:

$$\frac{I_s^i(p)}{I_{max}} = \frac{I_{bg}^i(p)}{I_{max}} + \varphi_i(p,T)\left[1 - \frac{I_{bg}^i(p)}{I_{max}}\right] \tag{6.7}$$

where the normalized Raman intensity in the wavelength range corresponding to species i is represented by $\frac{I_s^i(p)}{I_{max}}$. From Equation 6.7, we can be deduced that temperature T and the variables a and b in the linear approximation of the background signal are the fitting parameters for the normalized Raman spectra measured and simulated. This inference is in line with the finding that the shape of the Raman spectra, which is a function of temperature T, represents the Boltzmann distribution of the molecules over their original quantum states. As a result, the calibration constant C and molar fraction X_i only determine the size of the non-normalized Raman spectra.

The algorithms used execute the model fitting can now be implemented in MATLAB since all the parameters needed have been obtained. Two distinct least-squares fitting programs, each using the built-in **fmincon** function of MATLAB [88], were utilized to compute the temperature and molar fractions. The parameters, a and b in the linear approximation of background signal as well as temperature, T were the variables fitted for evaluating the temperature. The intensities of the simulation and the experiment are both normalized, and the residue $(\sum (|I_{\text{measured}} - I_{\text{simulated}}|)^2)$ is calculated from these spectra. When this residue reaches a local minimum, the fitting program stops. The main script of this fitting program is written in Appendix D. As an example, two results obtained utilizing this fitting program are visualized in Figure 6.5. The Raman scattered light associated with the energy transition from the vibrational ground state ($\nu'' = 0$) are detected for the determined temperature of 609 K, as shown in this Figure. However, Raman scattered light due to additional energy transitions from higher vibrational states ($\nu'' = 1$, $\nu'' = 2$) are detected for the 1497 K determined temperature. These transitions are called *hot bands* [62]. As discussed in chapter 3, Stokes Raman scattering is a measure of population distribution of molecules in the initial energy levels of the Raman transitions. As a result, Figure 6.5 infers that the nitrogen molecules only populate the vibrational ground state at temperature, T =609 K. Another inference is that higher vibrational states as well as the vibrational ground states of nitrogen molecules are populated at temperature, T =1497 K.

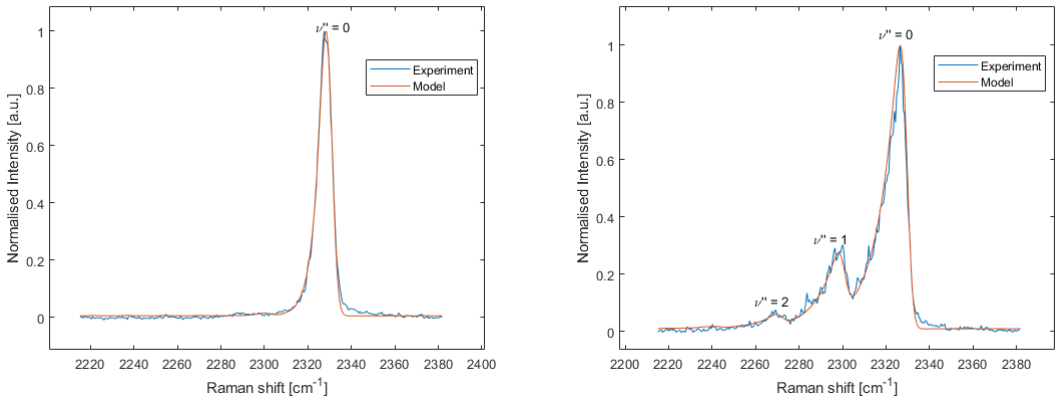

(a) **(b)**

Figure 6.5

The fitting program for the molar fraction determination is nearly identical to that of the temperature determination. This difference is that the molar fraction, X_i is the optimization parameter and the temperature, T is held constant. However, the residue is still defined in the same way without normalizing the spectra.

The molar fraction of NH_3 is computed employing a simple integration method based on Placzek's double harmonic approximation given by Equation 4.28. For this method, the background signal is determined by averaging the signals over two wavelength ranges close to the left and right sides of the Raman spectra of ammonia. This average signal is used a flat background offset and it is subtracted from the measured signal. Then, the resulting signal is integrated over another wavelength range that closely bounds its distinct peak. An example of this method is graphically illustrated in one of the measured signals discussed in chapter 7.

The local temperature and molar fractions of the major species present in a flame can be determined using the established code. However, a plethora of input variables and choices can affect the precision and accuracy of this evaluation. The estimation of these uncertainties are explained in the next section.

6.3 Error estimation

The uncertainties of the resulting temperature and molar fractions can be categorized into *systematic* and *random* errors. Systematic errors arise from the input of incorrect parameters such as calibration errors and they determine the accuracy of measurements, which describes how far the measured values are from the "true" value. Although these errors can be easily corrected if detected, they are difficult to notice because the "true" values are usually unknown [22]. Random errors are the effects of noise in the measurements and they are a determinant of how precise a set of repeated measurements is around the "true" value. This variation usually has a normal distribution. Additionally, Random errors are easy to detect but they can not be corrected for. However, its influence can be reduced by taking more repeated measurements. Unfortunately, the number of repeated measurements taken in this project is constrained because it takes long time (about 20 minutes) to perform each individual measurement. As a result, the so-called Monte-Carlo approach [3] is applied to solve this problem.

The Monte-Carlo approach is based on the idea that it is possible to simulate an experimental data if the measured experimental data (signal) is a summation of a best fitted curve and noise with a known distribution. This approach is executed by adding a collection of pseudo-random numbers selected at random from the specified probability distribution of the noise to the curve that best fits to the measured signal. An example of how this procedure works is visualized in Figure 6.6

for the case of temperature determination using a Raman spectrum of nitrogen measured in this project. In Figure 6.6a, the difference between the measured spectrum and the fitted spectrum is first calculated and represented as the noise in the signal. Then, the noise is plotted using an histogram in Figure 6.6b and its variation is fitted to normal distribution. Thirdly, artificial noise is produced using this distribution. Finally, this noise is added to the simulated spectrum to create a new measured spectrum plotted in Figure 6.6d, which mimics a repetition of the same measurement. Finally, a new temperature is determined by evaluating another curve that best fits this spectrum.

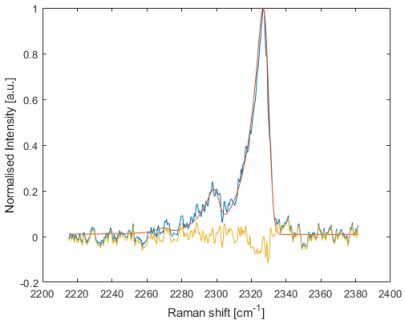

(a) Measured spectrum of N_2 (blue), the fitted spectrum (red) at determined temperature of 1330 K and the noise (difference) in yellow.

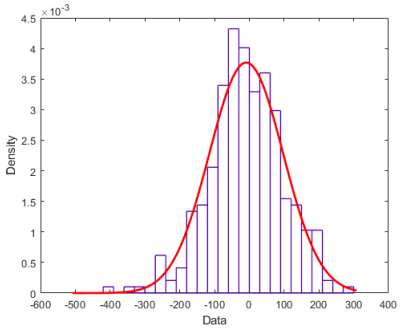

(b) Probability distribution of the noise(bars). A normal distribution(red curve) is fitted and it has a mean μ of -8.8106 and a standard deviation of 105.8106.

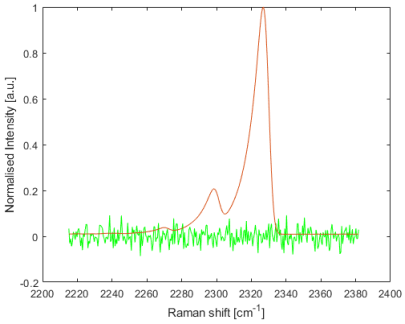

(c) The fitted spectrum of Figure 6.6a in red and the pseudo-random noise signal(green) determined from the fitted normal distribution in Figure 6.6b.

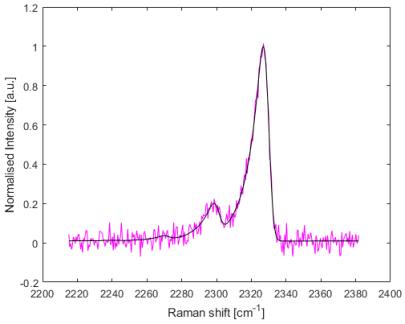

(d) The combined signal from Figure 6.6c in purple and the fitted spectrum of this new signal in black. The determined fitted temperature from this signal is 1314 K

Figure 6.6: An illustration of a Monte Carlo simulation used to estimate the error in a computed temperature. It can be seen that the generated spectrum has a slightly different temperature than the measured spectra. This difference(16 K) is about 1.2% of the computed temperature(1330 K).

By using the Monte-Carlo method, an infinite number of "experimental" data can be generated and used to quantify the precision of the temperature and molar fractions determined using the measured signals. For instance, Hessels [67], Stephenson and Blint [14] employed the Monte-Carlo method in their Raman experiments on hydrocarbon-based flames and found the variation in temperature measurements to be within a standard deviation of ±50 K. It is vital to note the precision of the temperature determination affects that of the molar fraction determination because the evaluated temperatures are also used to work out the molar fractions. As a result, the precision of the molar fractions is made up of both the inherent precision of molar fractions and the precision of the temperatures. In Appendix C, a thorough explanation of how the random errors are calculated from Monte-Carlo simulations is examined.

The results of various Raman experiments on non-premixed $NH_3/H_2/N_2$ and H_2 flames are discussed in the next chapter. To assess the precision of these findings, 25 Monte Carlo spectra of each spectrum are generated, and the standard deviation of the findings from these 25 spectra is computed.

Chapter 7

Experimental results

In this chapter, the results of two sets of measurements are discussed. Before measuring the Raman signals of the flames, their visible emissions are investigated. This is done to find the molecules that cause the luminosity of the diffusion flames. Then, the analysis of the temperature and molar fractions measured using Raman spectroscopy is explained. Finally, an investigation is executed to determine the influence of the molecular hydrogen(H_2) and ammonia(NH_3) flow rates on the temperature profile of the flames over their symmetry axis.

7.1 Flame luminosity

It was initially hypothesized that the hydrogen diffusion flames would not be luminous in the visible spectrum(380 - 750 nm). This postulation is birthed from the absence of carbon atoms in the fuel blend ($NH_2/H_2/N_2$), which prevents the occurrence of chemiluminescence caused by CH^*(431.5 nm), $C_2{}^*$(436-563 nm), $CO_2{}^*$(340-650 nm broadband) radicals in hydrocarbon flames [12]. However, this hypothesis is disproved because the first hydrogen flame ignited was visible to the human eye. To understand why this happened, the luminosity of H_2 and $NH_2/H_2/N_2$ flames is investigated in this project.

For this study, two diffusion flames are lit; one with 0.9321 normal liters per minute(ln/min) H_2 fuel and another with a fuel blend containing 0.0112 ln/min NH_3, 0.2400 ln/min N_2 and 0.9321 ln/min H_2. Both flames are ignited using a 30-ln/min co-flow of air. As a result, a laminar H_2 diffusion flame and a laminar $NH_3/H_2/N_2$ diffusion flame are produced with the same amount of H_2 fuel. The laser is turned off for this investigation since the visible emission of the flames is of interest, not Raman scattering. Firstly, images of these flames are taken with a DSLR(Nikon D7500) camera [91] that is focused at the flame location using a Nikon (AF Nikkor 50mm f/1.4D) lens [90]. Shown in Figures 7.1 and 7.2 are the images captured with an exposure time of 167 ms and f/1.4 aperture size.

At the exposure time of 167 ms, the wavelength(color) variations in the flames are captured without overexposing the image sensor of DSLR camera to relatively high intensities. To separate the short and long wavelengths, the images depicted in Figures 7.1 and 7.2 are filtered with the aid of Andover short-pass [83] and long-pass [82] filters, both with a cutoff wavelength of 550 nm. The result of this filtering for the H_2 flame is visualized in Figures 7.1b and 7.1c, and that of the $NH_3/H_2/N_2$ flame is illustrated in Figures 7.2b and 7.2c.

As displayed in Figure 7.1a, the unfiltered image of the H_2 flame comprises two color regions: the top red region and the purple region with comparatively high intensities at its curved edges. From filtered images pictured in Figures 7.1b and 7.1c, one can infer that the purple region of the H_2 flame is a combination of the blue and red-orange emissions. These filtered images also confirm that the top region of the H_2 flame only emits red-orange light.

Unlike the H_2 flame, there is an inner flame structure within the outer structure of the $NH_3/H_2/N_2$ flame, as displayed in Figure 7.2. As a result of filtering, One can deduce from Figure 7.2b that the inner flame structure gives off short wavelengths of light that appear green at its top region and blue everywhere else. Additionally, this inner flame structure emits red-orange light, as depicted in Figure 7.2c. On the other hand, the outer flame structure effuses long and

(a) **(b)** **(c)**

Figure 7.1: Digital photographs of the flame luminosity in a laminar H_2 diffusion flame. The pictures are taken with an exposure time of 167 ms and f/1.4 aperture size. Image (a) is unfiltered, while images (b) and (c) are filtered with short-pass and long-pass filters, respectively. The cutoff wavelength of both filters is 550 nm.

short wavelengths of light that have a regional distribution similar to the H_2 flame, as illustrated in Figures 7.2b and 7.2c.

The emission spectra of the flames are measured is to investigate the molecules that cause the light emissions in visible spectrum. This is executed using the detection system described in section 5.3 but with the laser still turned off. Hence, light emitted along the symmetry axis of the flames are studied. The 300-grooves/mm grating of the spectrograph is and an entrance slit with a 100-μm width is employed for this measurement. The measurements are taken over a spectral range of 410-740 nm that is divided into six wavelength intervals of equal length. Additionally, the measured emission spectra are averaged over the height of the flames and they are captured with multiple gates of 200-ms width.

The measured emission spectrum of the H_2 diffusion flame is visually represented in Figure 7.3a. This spectrum is compared to the one measured by Schefer et al. [41] for a laminar premixed H_2 jet flame and the spectrum measured by these researchers are depicted in Figure 7.3b. By inspection within the spectral range of 410-740 nm, it is evident that both spectra are roughly identical. The difference is the decreasing intensities of the emission spectra of the H_2 diffusion flame at wavelengths near the infrared region, which increases in the case of the spectra measured by Schefer et al. [41]. This difference is due to the decrease in sensitivity of the intensified CCD camera at wavelengths close to the infrared region. Nonetheless, the similarities seen in Figures 7.3a and 7.3b infers that the H_2 diffusion flame shown in Figure 7.1 emits the same wavelengths of light in the visible spectrum as the premixed H_2 jet flame studied by Schefer et al. [41].

In addition, Schefer et al. [41] discovered that the emission spectra of the premixed H_2 jet flame in the wavelength range from 600 to about 900 nm are spontaneous emissions caused by rovibrational transitions of excited water molecules [1]. Hence, the red emission along the symmetry axis of the H_2 diffusion flame in Figure 7.1 is due to excited water molecules. In their literature study, Schefer et al. [41] also discovered that the broad blue emission(blue continuum) in Figure 7.3b are a result of reactions involving OH and H radicals. However, these researchers concluded that further work needs to be done to identify the specific reactions that give rise to the blue continuum. This is because Schefer et al. [41] found a lot of discrepancies in different research studies on the cause of the blue continuum. For this reason, the blue emission in both the H_2 flame studied in this section and that of Schefer et al. [41] requires further investigation to determine reactions responsible for its luminescence.

(a) **(b)** **(c)**

Figure 7.2: Digital photographs of the flame luminosity in a laminar $NH_3/H_2/N_2$ diffusion flame. The photographs are taken with an exposure time of 167 ms and an f/1.4 aperture size. Image (a) is unfiltered, while images (b) and (c) are filtered with short-pass and long-pass filters, respectively. The cutoff wavelength of both filters is 550 nm.

As illustrated in Figure 7.3a, a distinct low-intensity peak at 590.21 nm is found in the emission spectrum of the H_2 diffusion flame. This peak is also visible on the emission spectrum of the premixed H_2 jet flame in Figure 7.3b. However, it is almost unnoticeable due to the significantly high intensities in the infrared region. Moreover, this peak is the spectrally unresolved combination of the so-called *sodium D-lines* transitions at 589.592- and 588.995-nm wavelengths [4, 8]. Although these transitions are experimentally known to give off a bright yellow light, their low intensities in the emission spectrum make them invisible in long-wavelength emissions of the H_2 flame in Figure 7.1c. However, their existence implies that there are sodium impurities either in the H_2 fuel, co-flow of air, or both gases used to ignite the premixed and diffusion H_2 flames.

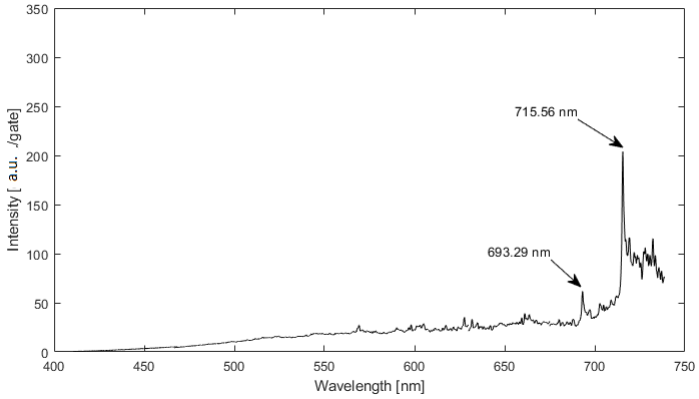

Figure 7.4: Spontaneous emission spectra of the $NH_3/H_2/N_2$ diffusion flame visualized in Figure 7.2. A spectral range(685 - 740 nm) of the water spectra in Figure 7.3 is identified in this spectra.

Visualized in Figure 7.4 is the measured emission spectrum of the $NH_3/H_2/N_2$ diffusion flame. In this spectrum, one can see a spectral range(approximately from 685 to 740 nm) of the

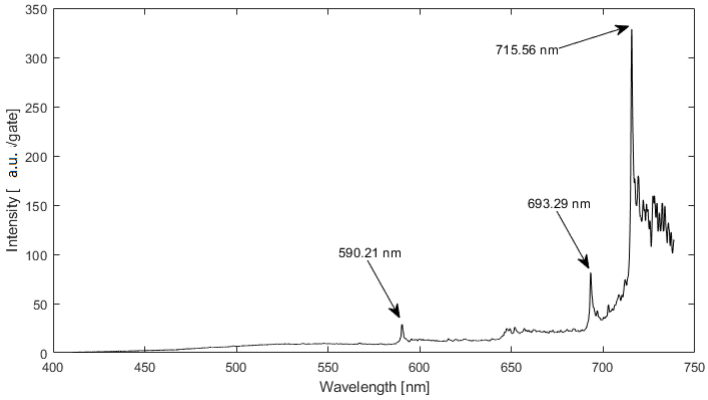

(a)

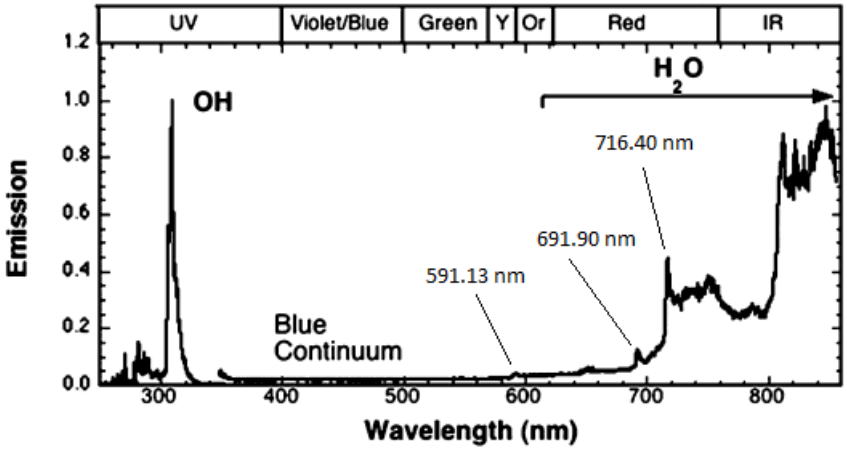

(b)

Figure 7.3: Spontaneous emission spectra of two H_2 flames. Figure (a) is the emission spectra of the H_2 diffusion flame pictured in Figure 7.1 and Figure (b) is the emission spectra of a premixed H_2 jet flame measured by Schefer et al. [41]. Note that spectrum (b) in the visible and infrared regions are scaled by a factor of 6.5 with respect to the OH spectrum in the Ultraviolet wavelength range. Additionally, the value difference between the peaks depicted in (a) and (b) is due to the different spectral resolutions of the spectrograph gratings used to measure them.

rovibrational transitions of excited water molecules occurring in the H_2 diffusion flame. This means that the red-orange light emitted by the $NH_3/H_2/N_2$ flame in Figure 7.2c is significantly due to excited water molecules present in the flame. However, the sources of the blue and green light emissions in $NH_3/H_2/N_2$ flame could not be discovered in this project. Hence, further research is needed for the discovery of these sources.

Conclusively, the H_2 and $NH_3/H_2/N_2$ diffusion flame luminosity is found to be partly due to the presence of excited water molecules. This result is promising as the thorough understanding of the flames' emission spectra could lead to the development of techniques used to measure the molar fractions of species such as NH_3 in laminar ammonia flames, like in the research carried out by Zhu et al. [80].

7.2 Temperature and molar fraction determination

After studying the luminosity of the flames, the laser is turned on for the Raman measurements of the $NH_3/H_2/N_2$ diffusion flames. Unfortunately, the stray light coming from the laser beam is found to be significantly reflected by the walls of the fuel tube. This resulted in high intensities of laser light at the fuel tube tip, which, as a consequence, dwarfed the weak Raman signals at that flame region. For this reason, the spectrograph is raised to the position where the distance between the bottom edge of the entrance slit and fuel tube tip is 3.95 mm. Thus, the value of parameter, h_1 in Equation 6.1 is equal to 3.95 mm. However, the new height level of the spectrograph implies that no measurement is taken at the flame region with close to the fuel tube tip.

A fuel blend comprising 0.3982 ln/min H_2, 0.0112 ln/min NH_3 and 0.2400 ln/min N_2 is utilized to lit the laminar $NH_3/H_2/N_2$ diffusion flame investigated in this section. This fuel mixture is selected because it is produced the largest flame that can be captured within the height of the entrance slit. The Raman scattered light is recorded with the two polarization configurations defined in section 5.4 and the images of the laser passing through the diffusion flame are shown in Figure 7.5 for both configurations. In these images, the Rayleigh line of air is visible in the perpendicular-perpendicular configuration and only a weak illumination of dust particles above the flame is noticeable.

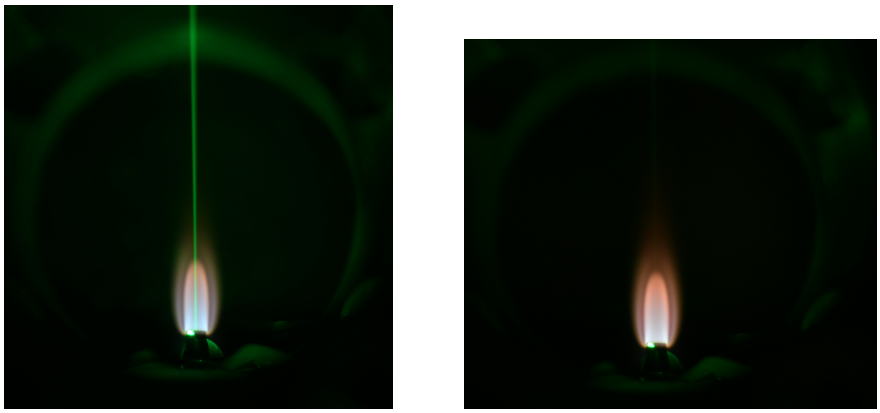

(a) Perpendicular-perpendicular configuration

(b) Parallel-perpendicular configuration

Figure 7.5: The two polarization configurations used to record the Raman signals.

To identify major species that could potentially cause Raman scattering, a total of six Raman spectra, each with a wavelength range of 20 nm, are measured. The combination of these spectra is illustrated in Figures 7.6 and 7.7 for the two polarization configurations. The 1200-grooves/mm grating is rotated five times between two consecutive wavelength ranges to obtain this combination. Additionally, 10^6 shots(gates), each with 200-ns width, are accumulated to obtain Raman spectra with high Signal-to-noise ratio. In the perpendicular-perpendicular configuration, the lines associated with pure rotational H_2 Raman transitions and rovibrational H_2, N_2, NH_3 Raman transitions are detected, as shown in Figure 7.6. However, the Raman line of oxygen at 1556 cm^{-1} is not observed in the spectra measured in the two polarization configurations. This means that the oxygen in the co-flow of air is either completely used up as an oxidizer or exists in a negligibly small amounts along the symmetry axis of the diffusion flame.

In addition, the Raman scattering process in the perpendicular-perpendicular configuration is interfered with by broad background signals that span its entire spectral range. This background signal exists in the height interval of about 6-16 mm above the fuel tube tip. To investigate this interference, the laser is turned off and the flame luminosity is captured with the same gate width and spectrograph grating as the Raman measurement. However, the signal recorded in this

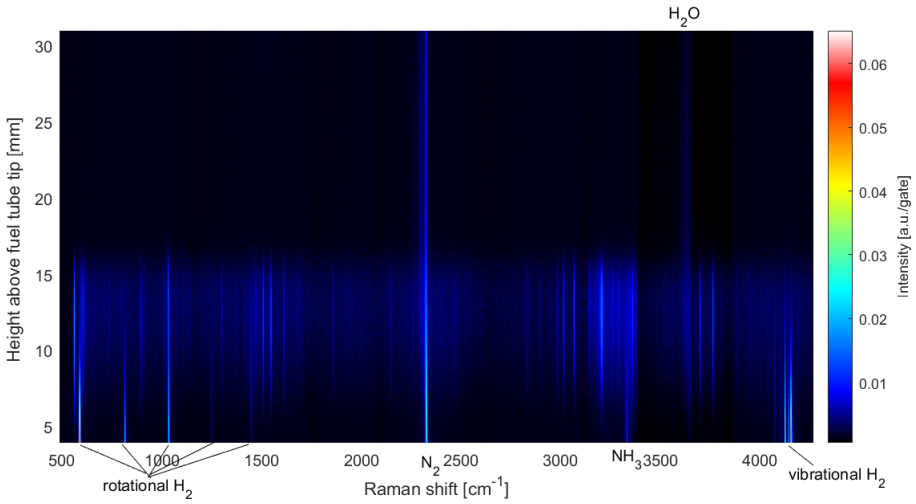

Figure 7.6: The Raman spectrum measured in perpendicular-perpendicular configuration. The Raman lines detected are: pure rotational H_2 lines at 588, 815, 1036, 1248 and 1448 cm^{-1}, N_2 line at 2328 cm^{-1}, NH_3 line at 3334 cm^{-1} and vibrational H_2 line at 4158 cm^{-1}.

investigation only contained CCD detector noise. Hence, the flame luminosity is ruled out as a source of the background signal. This means that the broad background signal originates the other laser-flame interactions such as Laser-induced Fluorescence (LIF) caused by one or more minor species in the flame. One of these potential species is Nitrogen dioxide(NO_2) as it is experimentally known to give off fluorescence at 526-nm excitation wavelength [10], which is the wavelength of the green laser used in this project. However, further research needs to be done to determine the exact species or group of species causing this LIF signal.

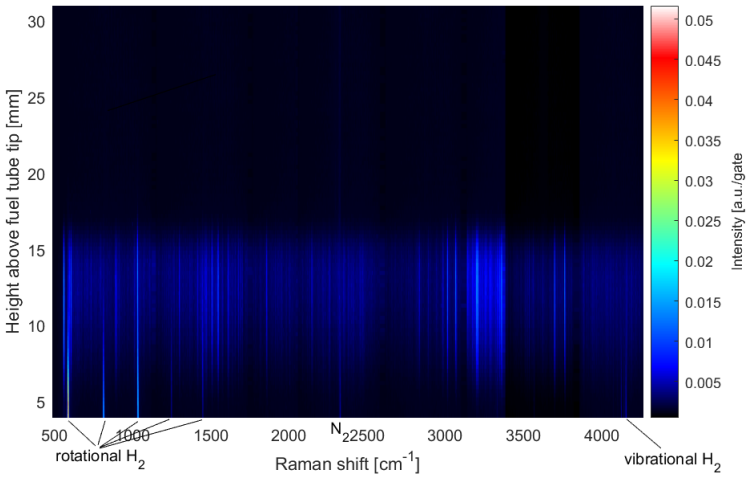

Figure 7.7: The Raman spectrum measured in parallel-perpendicular configuration. The broad background signal and pure rotational H_2 in the perpendicular-perpendicular configuration are also detected in these spectra.

For the parallel-perpendicular configuration, the broad background signals are detected in addition to the pure rotational H_2, vibrational N_2 and H_2 Raman lines, as depicted in Figure 7.7. By subtracting the measured spectra in this configuration from that of the perpendicular-

perpendicular configuration provided in Figure 7.6, the broad background signal and the pure rotational H_2 Raman lines (mostly) cancels out. This cancellation means that the broad background signal and the pure rotational H_2 Raman lines are not polarized. Additionally, this subtraction results in a decrease in the measured Raman signal. However, this reduction is accounted for by using the differential cross-section expressed in Equation 5.2. A visual representation of the reduced signal is illustrated in Figure 7.8.

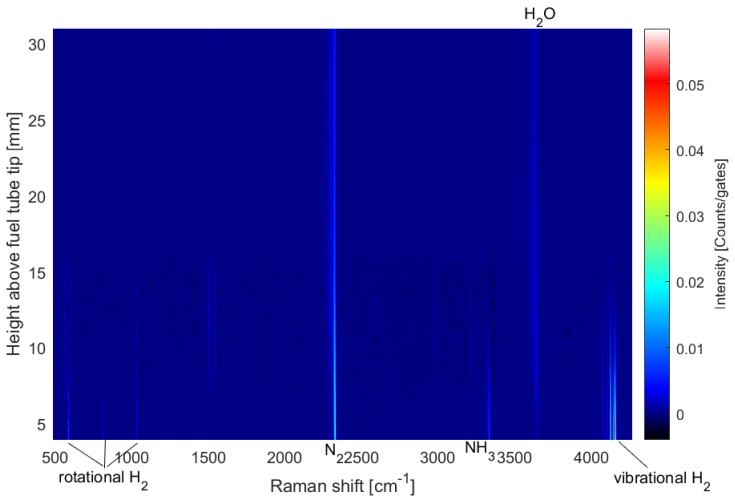

Figure 7.8: The Raman spectrum obtained from subtracting the Raman spectrum in parallel-perpendicular configuration from that of perpendicular-perpendicular configuration.

Having identified the molecules causing Stokes Raman scattering, the measured spectra are used to determine the temperature and molar fractions of molecules along the symmetric axis of the $NH_3/H_2/N_2$ diffusion flame. To evaluate the temperature, any of the identified molecules can be used in theory since $NH_3/H_2/N_2$ diffusion flame is in thermal equilibrium. However, the accuracy of each molecule-determined temperature would depend on the influence of noise on the least-square fitting procedure used to determine them. The Raman spectra of H_2O and NH_3 were found to have a significant amount of noise, making them poor candidates for the temperature determination. On the other hand, the Raman spectra of N_2 and vibrational H_2 sufficient Signal-to-noise ratios for temperature determination. However, the intensity of vibrational H_2 Raman lines diminishes as one moves up the flame due to the oxidation of the H_2 fuel. Hence, vibrational H_2 Raman lines are used to compute the temperature in the height range(4-11 mm above the fuel tube tip) where they are visible. In addition, the N_2 Raman lines are used to determine the temperature along the entire height of the symmetry axis. Two examples of the fitting of the measured and fitted spectra of N_2 and H_2 at different heights above the fuel tube are pictured in Figures 7.9a and 7.9b, respectively. The errors in N_2- and H_2-determined temperatures at these heights about 1.3% and 2.8% of their evaluated temperatures, respectively.

Depicted in Figure 7.10 is the N_2- and H_2-determined temperature profiles plotted on the same abscissa and ordinate axes. These profiles show that the evaluated temperatures follow a trend that oscillates around due to the influence of the random noise in the measured spectra. For this reason, the profiles are fitted to spline curves which describe their trends. By evaluating the temperature difference between these spline curves, the N_2-determined temperatures are found, on average, to be about 92 K greater than H_2-determined temperatures in the height regions where the vibrational H_2 are visible. Since this difference is in the order magnitude as the maximum errors(ΔT_{H_2} =30 K and ΔT_{N_2} =35 K) in N_2-determined and H_2-determined temperatures are in the same order of magnitude as this difference, it can be concluded that the Raman spectra of H_2 and N_2 roughly evaluate the same temperatures.

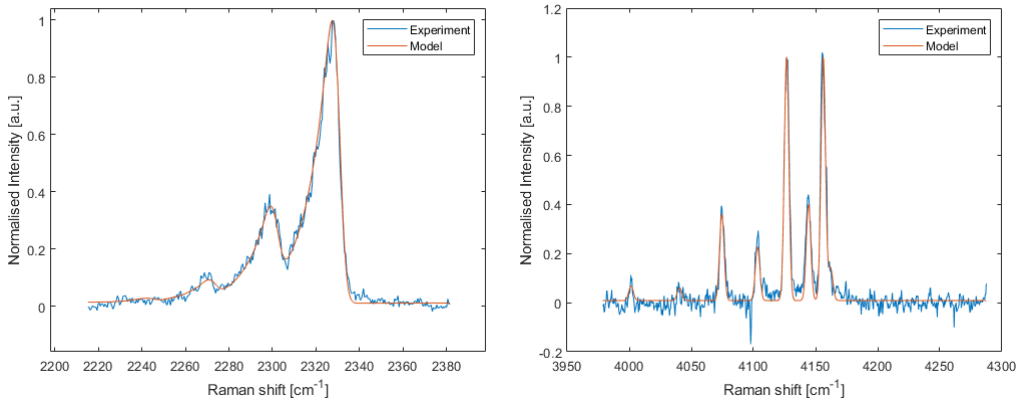

(a) $T_{N_2} = 1668 \pm 21$ K at height $h = 29.95$ mm **(b)** $T_{H_2} = 985 \pm 28$ K at height $h = 9.31$ mm

Figure 7.9: The model fits to the normalized Raman spectra of N_2 and H_2, and their determined temperature. The errors are 1.3% and 2.8% of the N_2- and H_2-determined temperatures, respectively.

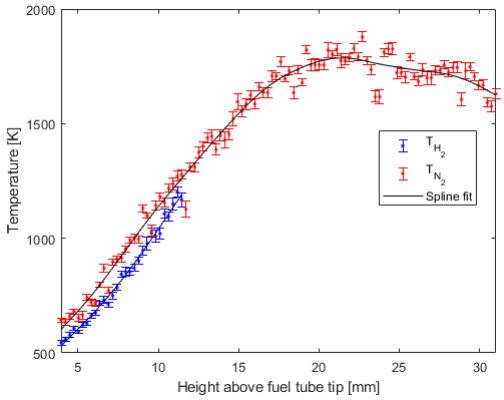

Figure 7.10: The temperature profiles obtained from the model fits to normalized N_2 and H_2 Raman spectra. The maximum error in the N_2- and H_2-determined temperatures are $\Delta T_{H_2} = 30$ K and $\Delta T_{N_2} = 35$ K. The temperatures are fitted to spline curves to show their trend. This average difference between the temperature profiles is 92 K at heights where H_2 Raman lines are detectable.

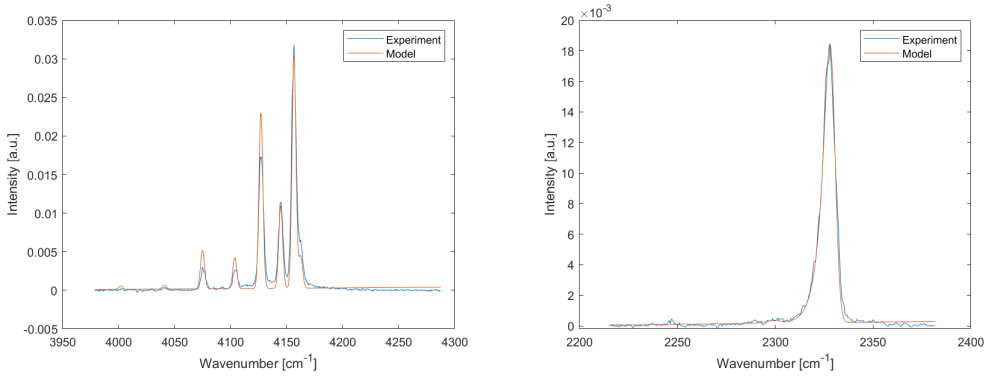

(a) $X_{H_2} = 0.5404 \pm 0.0040$ at h =5.29 mm using $T_{N_2} = 664$ K **(b)** $X_{N_2} = 0.5572 \pm 0.0033$ at $h = 5.29$ mm using $T_{H_2} = 621$ K

Figure 7.11: The model fits to the normalized Raman spectra showing the effectiveness of N_2 and H_2 Raman spectra in temperate determination.

To test the effectiveness of the determined temperatures, the N_2-determined temperature were used to the Raman spectra of H_2 for molar fraction evaluation and vice-versa. These evaluations were done at the height interval (4-11 mm above the fuel tube tip) where the nitrogen and hydrogen Raman lines are detectable. The findings of this calculation showed that the H_2-determined temperature produced the best fits that match the Raman spectra of nitrogen while the N_2-determined temperature gave poor fits to the Raman spectra of hydrogen at that height interval. Two examples of this discovery are illustrated in Figure 7.11 at 5.29-mm height above the fuel tube tip. As a result of this finding, we can infer that the H_2-determined temperatures for molar fraction determinations at the height interval close to the fuel tube. For this reason, the H_2-determined temperatures are used for evaluating the molar fractions at the height interval close to the fuel tube, and the N_2-determined temperatures are utilized for computing the molar fractions at the height positions where the H_2 Raman line are undetectable. For example, the model fits to the measured Raman spectra of H_2 and H_2O at height positions are provided in Figures 7.12a and 7.12b, respectively. Since these height positions are at two different height intervals, their corresponding measured spectra are fitted using temperatures determined from two different normalized Raman spectra(T_{H_2} for X_{H_2} and T_{N_2} For H_2O). For NH_3, its molar fraction is calculated using the derivative of Placzek's double harmonic approximation expressed in Equation 4.29. The intervals bounded by the green vertical lines in Figure 7.12c are used to evaluate the background offset of the ammonia Raman spectra, whereas the red ones indicate the integration boundaries of the ammonia signal.

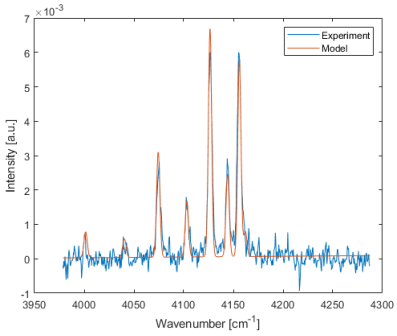

(a) $X_{H_2=}$ 0.1961 ± 0.0019 at h = 9.85 mm using T_{H_2} = 1009 K

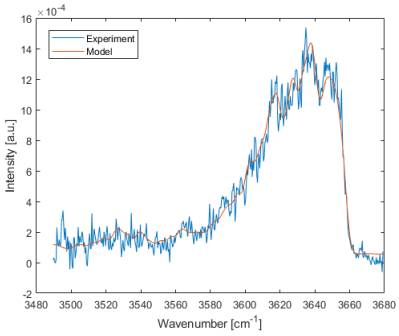

(b) X_{H_2O} = 0.1919 ± 0.0013 at h=30.49 mm using T_{N_2} = 1592 K

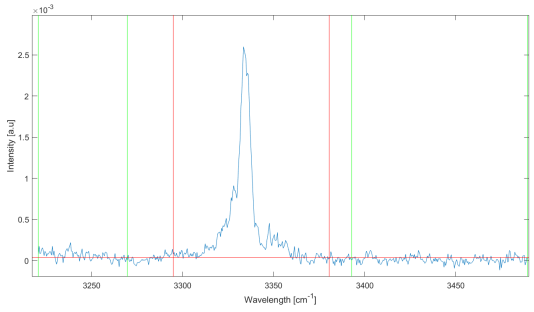

(c) X_{NH_3} = 0.0.0257 at h=5.02 mm using T_{H_2} = 592 K

Figure 7.12: The molar fraction determinations of NH_3, N_2 and H_2. Equation 4.29 is used to determine the molar fraction of NH_3. The background offset(red horizontal line) in the ammonia spectrum is determined by using the average of the mean of the signals in intervals bounded by green vertical lines (3393 - 3489 cm^{-1} and 3221 - 3270 cm^{-1}). The integration boundaries (red vertical lines) are in the wavenumber range of 3295 - 3381 cm^{-1}.

Using the N_2- and H_2-determined temperatures at their respective height intervals, the molar fractions of all the major species detected are computed and the results along the axis of symmetric of the diffusion flames are provided in Figure 7.13. As illustrated in Figure 7.13e, the combined determined temperatures and the molar fractions are plotted on the same abscissa. The ordinate of the molar fractions is on the left side, and that of the temperature is on the right side. From Figure 7.13e, we can see the H_2 and NH_3 fuel component decrease over the height of the diffusion flame, which is due to the oxidation. Moreover, the amount of NH_3 evaluated is small because the fuel blend contained low concentrations of NH_3. The height interval around the maximum temperature signifies the reaction zone at the top region of the diffusion flame, which is broad.

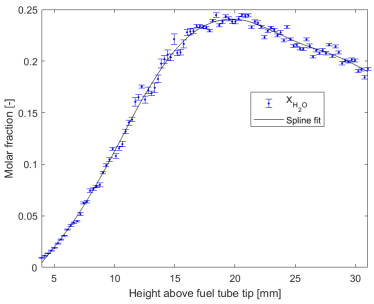

(a) Molar fractions of H_2O. maximum error $\Delta X_{H_2O} = 0.0049$

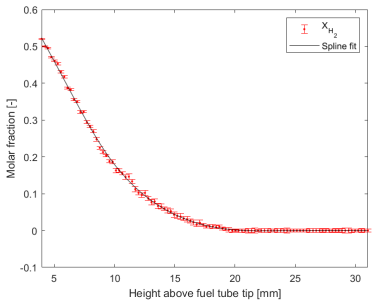

(b) Molar fractions of H_2. maximum error $\Delta X_{H_2} = 0.0054$

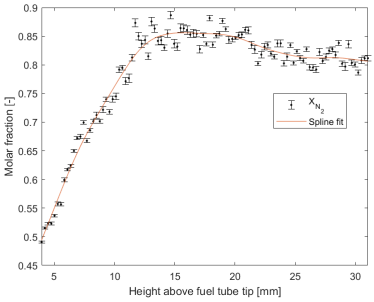

(c) Molar fractions of N_2. maximum error $\Delta X_{N_2} = 0.0078$

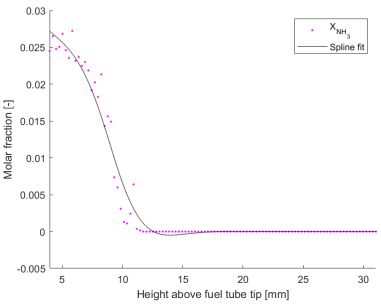

(d) Molar fractions of NH_3

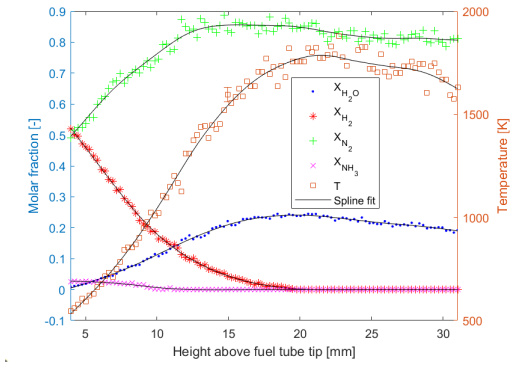

(e) The temperature profile and the molar fractions. maximum error in temperature $\Delta T = 35$ K

Figure 7.13: The molar fractions determined using H_2- and N_2-determined temperatures. The resulting temperature profile and molar fractions are plotted on the same abscissa but different ordinate.

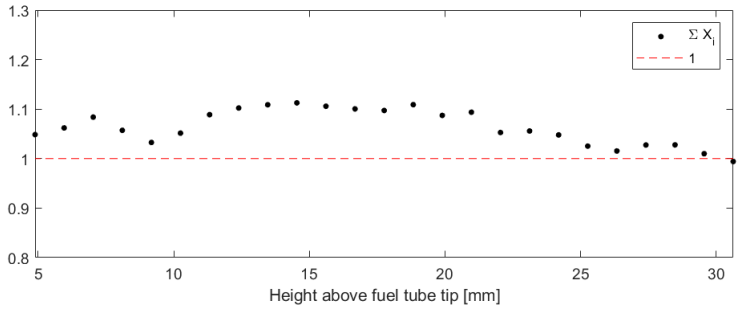

Figure 7.14: The sum of the determined molar fractions in Figure 7.13. The molar fractions are averaged over binned five heights. Since the sum of the molar fractions should equal one by definition, the blue dotted line serves as a reference line.

As mentioned in Appendix C, the noise in the measured Raman signals approximately had a normal distribution. Hence, the "true" values of the molar fractions are most likely the average of their fluctuating values [77]. For this reason, the molar fractions are averaged(binned) over five heights to get their "true" values. To check for the accuracy of the determined molar fractions, the sum of these values should be approximately equal to 1. This is because the addition of the molar fractions of the major species is equivalent to 1, which is following the species conservation principle($\Sigma X_i = 1$). Shown in Figure 7.14 is the comparison of the sum of the average molar fractions to the value of 1. This figure infers that the computed molar fractions are accurate at heights (from about 25 to 30 mm) above the reaction zone of the diffusion flame as their sum is roughly equal to 1. However, the computed molar fractions are inaccurate at other heights of the diffusion flame.

To investigate the inaccuracies of the molar fractions, the model fitted to the measured Raman spectra needs to be examined. As discussed in section 6.2, the shape of the simulated Raman spectra is determined by the calibration constant C and molar fraction X_i. Since the model fitting for molar fraction determined only corrects for the shape of the Raman spectra, the accuracy of the calculated molar fractions depends on the calibration constants. This means that the inaccuracies of the computed molar fractions are due to a systematic error in the calculated calibration constants of one or more species. One viable candidate is the molecular hydrogen calibration constant because it is calculated based on a molar fraction that is numerically estimated and not verified with experimental data, as discussed in Appendix A. As a result, the molar fractions of molecular hydrogen are overestimated because the sum, ΣX_i is greater than 1 at the heights where the molar fraction determinations are inaccurate. The calibration constants of N_2 and H_2O are not sources of the inaccurate nature of the computed molar fractions since they are computed in a gas mixture(air) of known composition. To improve the accuracy of the molar fraction determination, the calibration constant of H_2 needs to be calculated in a gas medium where the H_2 molar fraction is known.

Although the calibration constant of H_2 possesses systematic errors, an investigation into the influence of the concentration of the NH_3/N_2 and H_2 in the fuel blend is done. This investigation is possible because the temperature evaluated is not dependent on the calibration constant C, as outlined in section 6.2. The temperature profiles of two diffusion flames, ignited with two different flow rates of the NH_3/N_2 mixture and the same flow rate of H_2, are evaluated. As illustrated in Figure 7.15, the increase in the flow rate of the NH_3/N_2 mixture causes a decrease in the temperature at heights below 20 mm. This reduction is expected as the significant increase in N_2 in the mixture(containing 95.543% N_2) would reduce the concentration of O_2 needed for oxidation.

The flow rate of H_2 in the fuel blend is also increased and the result is visually represented in Figure 7.16. From this plot, we can see that the maximum temperature over the symmetry axis of the diffusion flame increases with an increase in the flow rate of H_2. Additionally, the height at maximum temperature(reaction zone) increases. This upward movement of the reaction zone

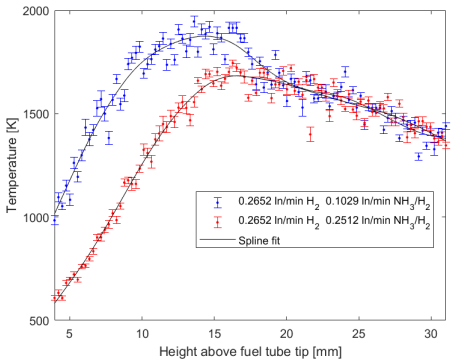

Figure 7.15: The temperature profiles for two different NH_3/N_2 flow rates. The temperature decreases with an increase in NH_3/N_2 flow rate at heights below 20 mm. The maximum error in both temperature profiles is $\Delta T_{max} = 41$ K.

was seen during the investigation as the size and height of the diffusion flames increased with the increase in the H_2 flow rate.

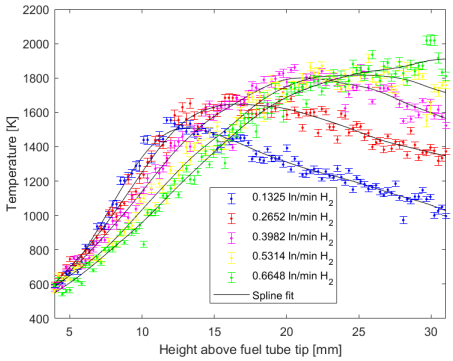

Figure 7.16: The temperature profiles for two different H_2 flow rates. The maximum temperature increases with an increase in H_2 flow and the height at maximum temperature increases. The maximum error in all the temperature profiles is $\Delta T_{max} = 37$ K.

To sum up, the random errors in the temperature measurements were found to be within ∓ 41 K in this project, which is comparable to the precisions found in literature [14, 53]. Additionally, the measured spectra of H_2 were found to be more effective at determining the temperatures at heights close to the fuel tube tip, as compared to that of N_2. However, the molar fractions determined were inaccurate due to a systematic error in the calibration constant of H_2.

Chapter 8

Conclusions and recommendations

The main objective of this project was acquiring and analyzing experimental data on the temperature and species concentration of NH_3/H_2 diffusion flames. However, this acquisition was not possible because the NH_3/H_2 fuel mixture needed to create the flames was unavailable. A solution to this setback was executed by studying diffusion flames lit using a fuel blend of pure H_2 and NH_3/N_2 mixture. As a result, the experimental data acquired in this project were on the temperature and species concentration of $NH_3/H_2/N_2$ diffusion flames.

To obtain the experimental data, a green(Nd:YLF) laser beam is passed through the symmetry axis of the diffusion flames. The Raman spectra from the laser-flame interaction are measured and analyzed. The measured Raman spectra identified contained light scattered by major species such as N_2, H_2O, H_2O and NH_3. After a thorough examination, the Raman spectra of H_2 are found to be most efficient in determining the temperatures of the diffusion flames at heights close to the fuel tube tip. Hence, it is used for temperature determination at heights where the H_2 Raman lines are detectable, whereas N_2 Raman spectra are utilized for evaluating the temperature at other heights over the symmetry axis of the flames. The maximum error in the temperature measurements is found to be within ± 41 K. On the other hand, the molar fractions evaluated are discovered to be inaccurate due to a systematic error in the calibration constant of H_2. For this reason, further research is required to improve how the calibration constant of H_2 is determined. Listed below are two recommendations for the improvement of the determination of the calibration constants.

- To lessen reflections of stray light at the fuel tube tip, the walls of the fuel tube can be painted black. By doing this, the wire mesh can be placed very close to the fuel tube tip, ensuring that the composition of the NH_3/H_2 mixture is constant and equal to that of the fuel tube tip. As a result, the calibration constant of H_2 can be evaluated using a molar fraction that is known, not numerically calculated.
- Mass flow meters designed for NH_3 and H_2 can be used to make certain that the flow rates delivered to the fuel tube are accurate.

References

[1] A. G. Gaydon, "Flame spectra in the photographic infra-red," *Proceedings of the Royal Society of London. Series A. Mathematical and Physical Sciences*, vol. 181, no. 985, pp. 197–209, 1942. DOI: 10.1098/rspa.1942.0071.

[2] G. Herzberg, *Molecular spectra and molecular structure. II, Infrared and Raman Spectra of Polyatomic Molecules*. New York: D. Van Nostrand Company, Inc, 1945.

[3] J. M. Hammersley and D. C. Handscomb, *Monte Carlo Methods*. Springer, 1964. DOI: 10.1007/978-94-009-5819-7.

[4] A. N. Zaidel', V. K. Prokof'ev, S. M. Raiskii, V. A. Slavnyi, and E. Y. Shreider, *Tables of Spectral Lines*. Boston, MA: Springer US, 1970, pp. 11–14, ISBN: 978-1-4757-1601-6. DOI: 10.1007/978-1-4757-1601-6.

[5] B. A. Lengyel, *Lasers*. New York, NY: Wiley-Interscience, 1971.

[6] K. Altmann and G. Strey, "Application of spherical tensors and wigner 3-j-symbols to the calculation of relative intensities of rotational lines in raman bands of molecular gases," *Journal of Molecular Spectroscopy*, vol. 44, pp. 571–577, 3 1972. DOI: 10.1016/0022-2852(72)90265-2.

[7] L. Landau and E. Lifshitz, *Mechanics and Electrodynamics*. Oxford: Permagon Press, 1972. DOI: 10.1016/C2009-0-06775-0.

[8] R. W. B. Pearse and A. G. Gaydon, *The identification of molecular spectra*. Chapman and Hall London, 1976, vol. 297.

[9] D. A. Long, *Raman spectroscopy*. McGraw-Hill, New York, 1977.

[10] V. Donnelly and F. Kaufman, "Fluorescence lifetime studies of NO_2. II. Dependence of the perturbed $^2B_2$ state lifetimes on excitation energy," *The Journal of Chemical Physics*, vol. 69, no. 4, pp. 1456–1460, 1978. DOI: 10.1063/1.436770.

[11] V. Zakaznov, L. Kursheva, and Z. Fedina, "Determination of normal flame velocity and critical diameter of flame extinction in ammonia-air mixture," *Combustion, Explosion and Shock Waves*, vol. 14, no. 6, pp. 710–713, 1978. DOI: 10.1007/BF00786097.

[12] A. G. Gaydon and H. G. Wolfhard, *Flames, their structure, radiation, and temperature*. Chapman & Hall, 1979.

[13] K. P. Huber and G. Herzberg, "Constants of diatomic molecules," in *Molecular Spectra and Molecular Structure: IV. Constants of Diatomic Molecules*. Boston, MA: Springer US, 1979, pp. 8–689, ISBN: 978-1-4757-0961-2. DOI: 10.1007/978-1-4757-0961-2_2.

[14] D. A. Stephenson and R. J. Blint, "Theoretical fitting of computer processed laser raman spectra from methane- and propane-air flames," *Applied spectroscopy*, vol. 33, no. 1, pp. 41–45, 1 Jan. 1979. [Online]. Available: https://opg.optica.org/as/abstract.cfm?URI=as-33-1-41.

[15] A. L. Buck, "New equations for computing vapor pressure and enhancement factor," *Proceedings of the Combustion Institute Journal of Applied Meteorology and Climatology*, 1981, ISSN: 1527–1532. DOI: 10.1175/1520-0450(1981)020%3C1527:NEFCVP%3E2.0.CO;2.

[16] H. G. M. Edwards, D. W. Farwell, A. C. Gorvin, and D. A. Long, "Pure rotational and vibration–rotational raman spectra of $^1H_2$, $^1H^2H$ and $^2H_2$," *Journal of Raman Spectroscopy*, vol. 17, no. 1, pp. 129–131, 1986. DOI: 10.1002/jrs.1250170126.

[17] P. D. Ronney, "Effect of chemistry and transport properties on near-limit flames at microgravity," *Combustion Science and Technology*, vol. 59, no. 1-3, pp. 123–141, 1988. DOI: 10.1080/00102208808947092.

[18] J. A. Miller and C. T. Bowman, *Mechanism and modeling of nitrogen chemistry in combustion*, 1989. DOI: 10.1016/0360-1285(89)90017-8.

[19] W. Fulkerson, R. R. Judkins, and M. K. Sanghvi, "Energy from fossil fuels," *Scientific American*, vol. 263, no. 3, pp. 128–135, 1990. [Online]. Available: http://www.jstor.org/stable/24996937.

[20] R. P. Lindstedt, F. C. Lockwood, and M. A. Selim, "Detailed kinetic modelling of chemistry and temperature effects on ammonia oxidation," *Combustion Science and Technology*, vol. 99, no. 4-6, pp. 253–276, 1994. DOI: 10.1080/00102209408935436.

[21] A. C. Eckbreth, *Laser diagnostics for combustion temperature and species*. CRC press, 1996, vol. 3. DOI: 10.1201/9781003077251.

[22] J. R. Taylor, *An introduction to error analysis*. University Science Books, Sausalito, CA, USA, 1997.

[23] M. Kotlarchyk, "Scattering theory," in *Encyclopedia of Spectroscopy and Spectrometry*, J. C. Lindon, Ed., Oxford: Elsevier, 1999, pp. 2074–2084, ISBN: 978-0-12-226680-5. DOI: 10.1006/rwsp.2000.0274.

[24] U. J. Pfahl, M. C. Ross, J. E. Shepherd, K. O. Pasamehmetoglu, and C. Unal, "Flammability limits, ignition energy, and flame speeds in H2–CH4–NH3–N2O–O2–N2 mixtures," *Combustion and Flame*, vol. 123, no. 1-2, pp. 140–158, 2000. DOI: 10.1016/S0010-2180(00)00152-8.

[25] A. R. Smith and J. Klosek, "A review of air separation technologies and their integration with energy conversion processes," *Fuel Processing Technology*, vol. 70, pp. 115–134, 2 2001. DOI: 10.1016/S0378-3820(01)00131-X.

[26] K. Kohse-Höinghaus and J. B. Jeffries, *Applied combustion diagnostics*. CRC, 2002. DOI: 10.1201/9781498719414.

[27] D. A. Long, *The Raman effect: a unified treatment of the theory of Raman scattering by molecules*. Wiley Chichester, 2002, vol. 8.

[28] Y. B. Zel'Dovich and Y. P. Raizer, *Physics of shock waves and high-temperature hydrodynamic phenomena*. Courier Corporation, 2002. DOI: 10.1016/B978-0-12-395672-9.X5001-2.

[29] G. Avila, G. Tejeda, J. M. Fernández, and S. Montero, "The rotational raman spectra and cross sections of h2o, d2o, and hdo," *Journal of Molecular Spectroscopy*, vol. 220, pp. 259–275, 2 2003. DOI: 10.1016/S0022-2852(03)00123-1.

[30] G. Avila, J. M. Fernández, G. Tejeda, and S. Montero, "The raman spectra and cross-sections of h2o, d2o, and hdo in the oh/od stretching regions," *Journal of Molecular Spectroscopy*, vol. 228, pp. 38–65, 1 2004. DOI: 10.1016/J.JMS.2004.06.012.

[31] E. Loewen, *Diffraction Grating Handbook*. C. Palmer. 6th. Newport Corporation, 2005.

[32] A. V. Mokhov, S. Gersen, and H. B. Levinsky, "Spontaneous raman measurements of acetylene in atmospheric-pressure methane/air flames," *Chemical Physics Letters*, vol. 403, pp. 233–237, 4-6 Feb. 2005. DOI: 10.1016/J.CPLETT.2005.01.021.

[33] M. L. Hause, Y. H. Yoon, and F. F. Crim, "NH_2 product distributions from the non-adiabatic photodissociation dynamics of ammonia," in *Abstracts of OSU International Symposium on Molecular Spectroscopy*, Ohio State University, 2006. [Online]. Available: http://hdl.handle.net/1811/31094.

[34] C. K. Law, *Combustion Physics*. Cambridge University Press, 2006. DOI: 10.1017/CBO9780511754517.

[35] W. Y. Huang, *Impact of rising natural gas prices on US ammonia supply*. DIANE Publishing, 2007.

[36] A. V. Mokhov, B. A. Bennett, H. B. Levinsky, and M. D. Smooke, "Experimental and computational study of c_2h_2 and co in a laminar axisymmetric methane–air diffusion flame," *Proceedings of the Combustion Institute*, vol. 31, pp. 997–1004, 1 2007. DOI: 10.1016/J.PROCI.2006.08.094.

[37] P. Dagaut, P. Glarborg, and M. U. Alzueta, "The oxidation of hydrogen cyanide and related chemistry," *Progress in Energy and Combustion Science*, vol. 34, no. 1, pp. 1–46, 2008. DOI: 10.1016/J.PECS.2007.02.004.

[38] K. Takizawa, A. Takahashi, K. Tokuhashi, S. Kondo, and A. Sekiya, "Burning velocity measurements of nitrogen-containing compounds," *Journal of Hazardous Materials*, vol. 155, no. 1-2, pp. 144–152, 2008. DOI: 10.1016/j.jhazmat.2007.11.089.

[39] A. A. Konnov, "Implementation of the NCN pathway of prompt-NO formation in the detailed reaction mechanism," *Combustion and Flame*, vol. 156, no. 11, pp. 2093–2105, 2009. DOI: 10.1016/J.COMBUSTFLAME.2009.03.016.

[40] T. Mendiara and P. Glarborg, "Ammonia chemistry in oxy-fuel combustion of methane," *Combustion and Flame*, vol. 156, no. 10, pp. 1937–1949, 2009. DOI: 10.1016/J.COMBUSTFLAME.2009.07.006.

[41] R. Schefer, W. Kulatilaka, B. Patterson, and T. Settersten, "Visible emission of hydrogen flames," *Combustion and Flame*, vol. 156, no. 6, pp. 1234–1241, 2009, ISSN: 0010-2180. DOI: https://doi.org/10.1016/j.combustflame.2009.01.011.

[42] T. J. Dijkman and R. M. Benders, "Comparison of renewable fuels based on their land use using energy densities," *Renewable and Sustainable Energy Reviews*, vol. 14, no. 9, pp. 3148–3155, 2010. DOI: 10.1016/J.RSER.2010.07.029.

[43] K. S. Lackner, "Comparative impacts of fossil fuels and alternative energy sources," *Issues in environmental science and technology*, vol. 29, p. 1, 2010. [Online]. Available: http://sutlib2.sut.ac.th/sut_contents/H131563.pdf.

[44] J. H. Lee, J. H. Kim, J. H. Park, and O. C. Kwon, "Studies on properties of laminar premixed hydrogen-added ammonia/air flames for hydrogen production," *International Journal of Hydrogen Energy*, vol. 35, no. 3, pp. 1054–1064, 2010. DOI: 10.1016/j.ijhydene.2009.11.071.

[45] I. A. Amar, R. Lan, C. T. Petit, and S. Tao, "Solid-state electrochemical synthesis of ammonia: A review," *Journal of Solid State Electrochemistry*, vol. 15, pp. 1845–1860, 9 2011. DOI: 10.1007/s10008-011-1376-x.

[46] S. J. Klippenstein, L. B. Harding, P. Glarborg, and J. A. Miller, "The role of NNH in NO formation and control," *Combustion and Flame*, vol. 158, no. 4, pp. 774–789, 2011. DOI: 10.1016/J.COMBUSTFLAME.2010.12.013.

[47] I. Dincer and C. Zamfirescu, *Apparatus for using ammonia as a sustainable fuel, refrigerant and nox reduction agent*, US Patent 8,272,353, 2012.

[48] C. Duynslaegher, F. Contino, J. Vandooren, and H. Jeanmart, "Modeling of ammonia combustion at low pressure," *Combustion and Flame*, vol. 159, no. 9, pp. 2799–2805, 2012. DOI: 10.1016/J.COMBUSTFLAME.2012.06.003.

[49] C. Hulteberg, "Sulphur-tolerant catalysts in small-scale hydrogen production, a review," *International Journal of Hydrogen Energy*, vol. 37, pp. 3978–3992, 5 2012. DOI: 10.1016/J.IJHYDENE.2011.12.001.

[50] M. Koike, H. Miyagawa, T. Suzuoki, K. Ogasawara, *et al.*, "Ammonia as a hydrogen energy carrier and its application to internal combustion engines," *Sustainable vehicle technologies*, pp. 61–70, 2012.

[51] D. A. Oliveira, "Development and application of a laminar coflow burner for combustion studies at high pressure development and application of a laminar coflow burner for combustion studies at high pressure," Ph.D. dissertation, 2012. DOI: 10.6100/IR732108.

[52] P. Kumar and T. R. Meyer, "Experimental and modeling study of chemical-kinetics mechanisms for H2–NH3–air mixtures in laminar premixed jet flames," *Fuel*, vol. 108, pp. 166–176, 2013. DOI: 10.1016/J.FUEL.2012.06.103.

[53] A. V. Sepman, V. V. Toro, A. V. Mokhov, and H. B. Levinsky, "Determination of temperature and concentrations of main components in flames by fitting measured Raman spectra," *Applied Physics B: Lasers and Optics*, vol. 112, no. 1, pp. 35–47, 2013. DOI: 10.1007/s00340-013-5389-2.

[54] J. Li, H. Huang, N. Kobayashi, Z. He, and Y. Nagai, "Study on using hydrogen and ammonia as fuels: Combustion characteristics and nox formation," *International Journal of Energy Research*, vol. 38, no. 9, pp. 1214–1223, 2014. DOI: https://doi.org/10.1002/er.3141.

[55] E. Morgan, J. Manwell, and J. McGowan, "Wind-powered ammonia fuel production for remote islands: A case study," *Renewable Energy*, vol. 72, pp. 51–61, 2014. DOI: 10.1016/J.RENENE.2014.06.034.

[56] S. Choi, S. Lee, and O. C. Kwon, "Extinction limits and structure of counterflow nonpremixed hydrogen-doped ammonia/air flames at elevated temperatures," *Energy*, vol. 85, pp. 503–510, 2015. DOI: 10.1016/j.energy.2015.03.061.

[57] F. Fuest, R. S. Barlow, G. Magnotti, A. Dreizler, I. W. Ekoto, and J. A. Sutton, "Quantitative acetylene measurements in laminar and turbulent flames using 1d raman/rayleigh scattering," *Combustion and Flame*, vol. 162, pp. 2248–2255, 5 2015. DOI: 10.1016/J.COMBUSTFLAME.2015.01.021.

[58] A. Hayakawa, T. Goto, R. Mimoto, Y. Arakawa, T. Kudo, and H. Kobayashi, "Laminar burning velocity and Markstein length of ammonia/air premixed flames at various pressures," *Fuel*, vol. 159, pp. 98–106, 2015. DOI: 10.1016/j.fuel.2015.06.070.

[59] A. Ichikawa, A. Hayakawa, Y. Kitagawa, K. D. Kunkuma Amila Somarathne, T. Kudo, and H. Kobayashi, "Laminar burning velocity and Markstein length of ammonia/hydrogen/air premixed flames at elevated pressures," *International Journal of Hydrogen Energy*, vol. 40, no. 30, pp. 9570–9578, 2015. DOI: 10.1016/j.ijhydene.2015.04.024.

[60] Y. Kojima, H. Miyaoka, and T. Ichikawa, "16 ammonia-based hydrogen storage materials," *Advanced materials for clean energy*, p. 497, 2015.

[61] O. Mathieu and E. L. Petersen, "Experimental and modeling study on the high-temperature oxidation of Ammonia and related NOx chemistry," *Combustion and Flame*, vol. 162, no. 3, pp. 554–570, 2015. DOI: 10.1016/J.COMBUSTFLAME.2014.08.022.

[62] R. K. Hanson, R. M. Spearrin, and C. S. Goldenstein, *Spectroscopy and optical diagnostics for gases*. Springer, 2016, vol. 1. DOI: 10.1007/978-3-319-23252-2.

[63] M. A. Linne, *Lecture notes in advanced laser diagnostics for combustion research*, Jun. 2016.

[64] R. K. Pearson, Y. Neuvo, J. Astola, and M. Gabbouj, "Generalized hampel filters," *EURASIP Journal on Advances in Signal Processing*, 1 2016. DOI: 10.1186/s13634-016-0383-6.

[65] Y. Song, H. Hashemi, J. M. Christensen, C. Zou, P. Marshall, and P. Glarborg, "Ammonia oxidation at high pressure and intermediate temperatures," *Fuel*, vol. 181, pp. 358–365, 2016. DOI: 10.1016/J.FUEL.2016.04.100.

[66] C.-P. I. Company, *Chemical compatibilty database, ammonia, anhydrous*, 2017. [Online]. Available: https://www.coleparmer.co.uk/Chemical-Resistance.

[67] C. J. M. Hessels, "Quantitative analysis of non-premixed flames using raman spectroscopy," M.S. thesis, 2017.

[68] Standford research systems, *DG535 Digital delay / Pulse Generator operation and service manual*. 2017. [Online]. Available: https://www.thinksrs.com/downloads/pdfs/manuals/DG535m.pdf.

[69] P. Glarborg, J. A. Miller, B. Ruscic, and S. J. Klippenstein, "Modeling nitrogen chemistry in combustion," *Progress in Energy and Combustion Science*, vol. 67, pp. 31–68, 2018. DOI: 10.1016/J.PECS.2018.01.002.

[70] E. C. Okafor *et al.*, "Experimental and numerical study of the laminar burning velocity of CH4–NH3–air premixed flames," *Combustion and Flame*, vol. 187, pp. 185–198, 2018. DOI: 10.1016/J.COMBUSTFLAME.2017.09.002.

[71] J. Otomo, M. Koshi, T. Mitsumori, H. Iwasaki, and K. Yamada, "Chemical kinetic modeling of ammonia oxidation with improved reaction mechanism for ammonia/air and ammonia/hydrogen/air combustion," *International Journal of Hydrogen Energy*, vol. 43, no. 5, pp. 3004–3014, 2018. DOI: 10.1016/J.IJHYDENE.2017.12.066.

[72] A. Valera-Medina, H. Xiao, M. Owen-Jones, W. I. David, and P. J. Bowen, "Ammonia for power," *Progress in Energy and Combustion Science*, vol. 69, pp. 63–102, 2018. DOI: 10.1016/j.pecs.2018.07.001.

[73] "Chemical kinetic modelling of ammonia/hydrogen/air ignition, premixed flame propagation and NO emission," *Fuel*, vol. 246, no. December 2018, pp. 24–33, 2019. DOI: 10.1016/j.fuel.2019.02.102.

[74] R. Doddema, N. J. Dam, and C. Hessels, "Raman spectroscopy on methane, ethylene and propane flames," in *Laser Diagnostics in Energy and Combustion Science*, Gordon Research Conference, 2019. [Online]. Available: https://pure.tue.nl/ws/portalfiles/portal/207364810/poster.pdf.

[75] H. Kobayashi, A. Hayakawa, K. K. A. Somarathne, and E. C. Okafor, "Science and technology of ammonia combustion," *Proceedings of the Combustion Institute*, vol. 37, no. 1, pp. 109–133, 2019. DOI: 10.1016/j.proci.2018.09.029.

[76] A. Yapicioglu and I. Dincer, "A review on clean ammonia as a potential fuel for power generators," *Renewable and sustainable energy reviews*, vol. 103, pp. 96–108, 2019. DOI: 10.1016/j.rser.2018.12.023.

[77] N. J. Dam, *Lecture notes in introduction to laser diagnostics*, Jun. 2020.

[78] M. Kögler and B. Heilala, "Time-gated raman spectroscopy – a review," *Measurement Science and Technology*, vol. 32, 1 Aug. 2020. DOI: 10.1088/1361-6501/abb044.

[79] J. A. Van Oijen, *Lecture notes in chemically reacting flows: Non-premixed flames*, May 2021.

[80] X. Zhu, W. L. Roberts, and T. F. Guiberti, "UV-visible chemiluminescence signature of laminar ammonia-hydrogen-air flames," *Proceedings of the Combustion Institute*, 2022, ISSN: 1540-7489. DOI: 10.1016/j.proci.2022.07.021.

[81] *[One extra reference NIST Chemistry WebBook, SRD 69, Thermophysical Properties of Fluid Systems*, National Institute of Standard and Technology.

[82] Andover Corporation, *LONG WAVE PASS EDGE FILTERS*. [Online]. Available: https://www.andovercorp.com/products/edge-filters/long-wave-pass/, (accessed: 20.01.2023).

[83] Andover Corporation, *SHORT WAVE PASS EDGE FILTERS*. [Online]. Available: https://www.andovercorp.com/products/edge-filters/short-wave-pass/, (accessed: 20.01.2023).

[84] Bronkhorst FLUIDAT®, *Determination of gas conversion factors using the physical properties of gases*. [Online]. Available: https://www.fluidat.com/default.asp, (accessed: 18.01.2023).

[85] Bronkhorst High-Tech B.V., *El-flow select - laboratory style gas mass flow meters / mass flow controllers*. [Online]. Available: https://www.bronkhorst.com/int/products/gas-flow/el-flow-select/, (accessed: 18.01.2023).

[86] Edmund Optics, *532 nm, 50 mm diameter, od 4 notch filter*. [Online]. Available: https://www.edmundoptics.com/p/532nm-50mm-diameter-od-4-notch-filter/21665/, (accessed: 18.01.2023).

[87] K. Kraus, *Wigner3j symbol*. [Online]. Available: https://nl.mathworks.com/matlabcentral/fileexchange/20619-wigner3j-symbol, (accessed: 18.01.2023).

[88] MathWorks, *Fmincon: Find minimum of constrained nonlinear multivariable function*. [Online]. Available: https://nl.mathworks.com/matlabcentral/fileexchange/20619-wigner3j-symbol, (accessed: 18.01.2023).

[89] Nikon Corporation, *AF DC-Nikkor 105mm f/2d*. [Online]. Available: https://www.nikon.nl/nl_NL/product/discontinued/nikkor-lenses/2021/af-dc-nikkor-105mm-f-2d#overview, (accessed: 18.01.2023).

[90] Nikon Corporation, *AF Nikkor 50mm f/1.4D*. [Online]. Available: https://www.nikon.nl/nl_NL/product/discontinued/nikkor-lenses/2021/af-nikkor-50mm-f-1-4d#tech_specs, (accessed: 20.01.2023).

[91] Nikon Corporation, *Nikon D7500 DSLR camera*. [Online]. Available: https://www.nikonusa.com/en/nikon-products/product/dslr-cameras/d7500.html#tab-ProductDetail-ProductTabs-Overview, (accessed: 20.01.2023).

[92] Photonic Industries, *Dm-527 series: High pulse energy green Nd:YLF lasers*. [Online]. Available: http://www.photonix.com/product/dm-ylf-green-series/, (accessed: 18.01.2023).

[93] Princeton Instruments, *Operating instructions acton sp-500i*. [Online]. Available: ftp://ftp.princetoninstruments.com/public/Manuals/Acton/Sp-500i.pdf, (accessed: 18.01.2023).

[94] Princeton Instruments, *Pi-max 3 iccd camera*. [Online]. Available: https://www.electrooptics.com/press-releases/pi-max-3-iccd-camera, (accessed: 18.01.2023).

[95] Thorlabs, Inc., *Polymer zero-order half-wave plates*. [Online]. Available: https://www.thorlabs.com/newgrouppage9.cfm?objectgroup_id=7054, (accessed: 18.01.2023).

[96] Thorlabs, Inc., *V-coated laser windows*. [Online]. Available: https://www.thorlabs.com/newgrouppage9.cfm?objectgroup_id=1121&pn=WL11050-C10, (accessed: 18.01.2023).

[97] D. Yan, *Guide to raman spectroscopy*. [Online]. Available: https://www.bruker.com/en/products-and-solutions/infrared-and-raman/raman-spectrometers/what-is-raman-spectroscopy.html, (accessed: 18.01.2023).

Appendix A

Calibration constants

This appendix outlines how the calibrations constants, C in Equation (4.27) are calculated. These calibration evaluations are executed for gases of known composition and at room temperature (294 K) and atmospheric pressure (1 bar). With the assumption that molecular and oxygen have molar fractions of 0.7810 and 0.2095, respectively, the calibration coefficients of N_2, O_2, and H_2O are calculated from the Raman spectra in air. This assumption is based on the atmospheric composition of gases in air. Using a hygrometer that measures relative humidity, the molar fraction of water is computed, and the resultant molar fraction is calculated to be 0.01342 for a relative humidity of 55 %. This molar fraction calculation is done using Buck's empirical correlations [15] for the temperature-dependent saturated vapor pressure and ideal gas law assumption. The calculated calibration coefficients are shown in Table A.1, which are normalized to the nitrogen calibration as determined by the perpendicular-perpendicular configuration his normalization is done to correct for daily changes in the calibration constants, as explained in section 5.4. Since the differential cross section for H_2O is derived from complied tables [16] rather than Equations eq. (4.17) and 4.17, it causes the calibration constant of H_2O to be substantially larger than those of N_2 and O_2.

For calibration of NH_3 and H_2, the Raman spectra in the mixture of these gases are measured at 294 K and 1 bar. This mixture contained a molar composition of $X_{H_2=}0.7258$, $X_{N_2=}0.2620$ and $X_{NH_3=}0.01222$. Since molecular hydrogen is explosive and ammonia causes irritation, the gas mixture is consumed at a certain height above the fuel tube tip to prevent hazards around the experimental setup. This consumption is executed by placing a wire mesh above the fuel tube and a flame is ignited above the mesh. Initially, it was planned to the wire mesh so close to the fuel tube tip that the molar composition of the gas mixture can be assumed to remain the same as that of the gas mixture entering the tube. However, the significant reflections of stray light coming from the green laser buried the Raman signal at the height positions close to the fuel tube tip. Hence, the wire mesh could not be placed close to the fuel tube tip as the Raman signals in this region were undetected. To solve this problem, the wire mesh is moved up to a height of 10 mm.

Another problem arose as the diffusion flame burnt the wire mesh due to its temperature. This also caused the flame to reattach itself to the fuel tube. To circumvent these issues, the co-flow of air is replaced with a pure N_2 co-flow to prevent combustion from occurring below the wire mesh. Unfortunately, this replacement caused the flame to go off once the chimney is placed on the burner. For this reason, the chimney is removed to allow enough oxygen to come from the top of the burner vessel. Now, the molar fraction of NH_3 and H_2 is required for calibration at the heights between the wire mesh and fuel tube tip. As a result, the molar fractions are computed numerically using CFD software package called ANSYS Fluent. For steady, laminar, ANSYS Fluent uses the following equations for continuity, species conservation, momentum, and energy:

$$\begin{aligned}
\nabla \cdot (\rho \mathbf{v}) &= 0 \\
\nabla \cdot (\rho \mathbf{v} Y_i) - \nabla \cdot \left(\frac{\lambda}{Le_i C_p} \cdot \nabla Y_i \right) &= 0 \\
\nabla \cdot (\rho \mathbf{v}\mathbf{v}) &= -\nabla p + \nabla \cdot \bar{\bar{\tau}} \\
\nabla \cdot ((\rho E + p)\mathbf{v}) &= \nabla \cdot (k \nabla T) - \nabla \cdot (\Sigma_i h_i \rho D_{i,m} \nabla Y_i)
\end{aligned} \tag{A.1}$$

where $\mathbf{v}$ is velocity vector, ρ is the density, Y_i are the species mass fractions,i are the species source terms, p is the pressure, k is the thermal conductivity, T is the temperature, and $D_{i,m}$ are diffusion constants for the species. The total energy E, enthalpy h, species enthalpy h_i, and molar fraction are given by:

$$\begin{aligned}
\bar{\bar{\tau}} &= \mu \left[\left(\nabla \mathbf{v} + \nabla \mathbf{v}^{\mathbf{T}} \right) - \frac{2}{3} \nabla \cdot \mathbf{v} I \right] \\
E &= h - \frac{p}{\rho} + \frac{v^2}{2} \\
h &= \Sigma_i Y_i h_i \\
h_i &= \int_{T_{ref}}^{T} C_{p,i} dT \\
X_i &= Y_i \frac{\overline{M}}{M_i}
\end{aligned} \tag{A.2}$$

where $\overline{M}$ and M_i are the molecular mass of species i and the mixture, respectively. Since the flow above the wire mesh is of little interest, the flame ignited above the mesh is considered in this CFD simulation. As a result, the computational complexity of the simulation is reduced and the assumption made is that the flow in the flame has a negligible influence on the fluid flow blow the wire mesh. The burner vessel is modeled as a 2D geometry and a mesh size of 1 mm is used for the computation. Shown in Figure A.1 is the computational domain of the numerical simulation and the molar fractions of N_2, H_2 and NH_3 at the fuel and co-flow inlets.

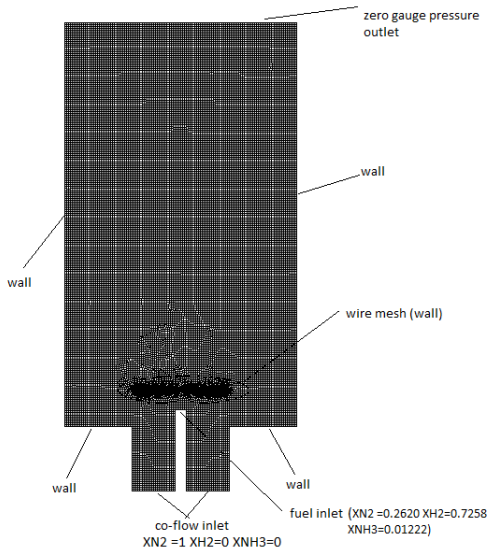

Figure A.1: Computational domain of the burner vessel. A mesh size of 1 mm is used. The wire mesh is modeled as an array of small circular walls with a 0.3-mm diameter, which is equivalent to the cross-sectional diameters of wires in the mesh.

The numerical results of the CFD simulation are illustrated in Figure A.2 for the velocity magnitude of the fluid flow and molar fractions of N_2, H_2 and NH_3. The molar fractions of species would be less accurate the closer one gets to the mesh since the assumption made is that the flame does not influence the fluid flow below the wire mesh. For this reason, only the calculated values of the molar fractions at the height $h = 3.95mm$ are used for the calibration. these values are: $X_{NH_3} = 0.01248$, $X_{H_2} = 0.7254$ and $X_{N_2} = 0.2621$.

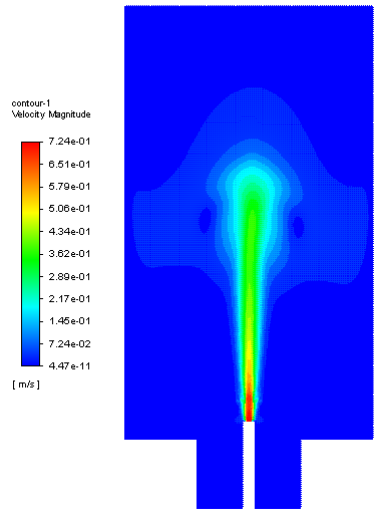

(a) Magnitude of velocity

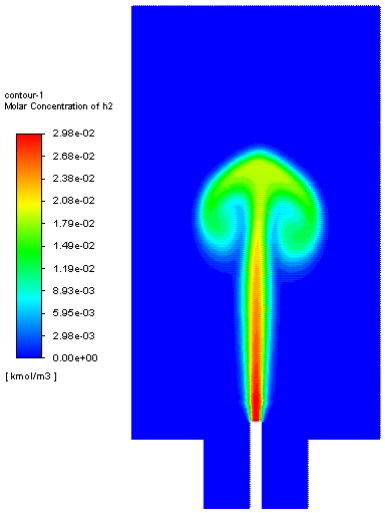

(b) molar fraction of molecular hydrogen X_{H_2}

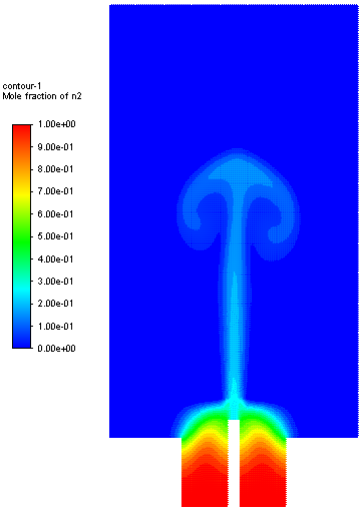

(c) molar fraction of molecular nitrogen X_{N_2}

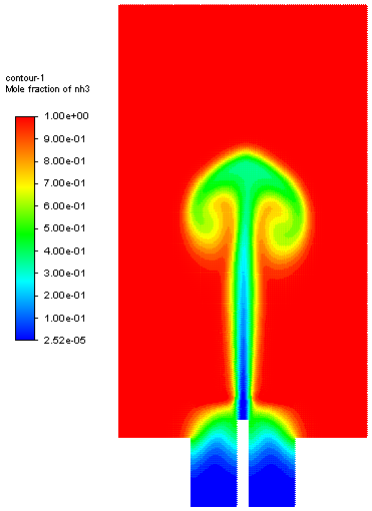

(d) molar fraction of ammonia X_{NH_3}

Figure A.2: Numerical results of the velocity magnitude of the fluid flow and molar fractions of the species in the burner vessel.

Using the molar fractions of N_2, O_2 and H_2O in air and the numerically evaluated molar fraction of NH_3 and H_2, the calibration constants of all the species are determined and normalized with respect to the calibration constant of N_2 in the perpendicular-perpendicular configuration. This normalization is done with aim to correct for the daily changes in the calibration constants, as explained in section 5.4. The calculated calibration constants are listed in Table A.1.

Species	$C^{\perp\perp} - C^{\parallel\perp}$	$\bar{\nu}_{\text{min}}\,[\text{cm}^{-1}]$	$\bar{\nu}_{\text{max}}\,[\text{cm}^{-1}]$	Raman shift $[\text{cm}^{-1}]$
N_2	0.9546			2331
O_2	0.8483			1556
H_2	2.0043			1285
H_2O	512.3993			3654
NH_3	$2.9233 \cdot 10^{-3}$	3295	3381	3334

Table A.1: The calibration constants of the species with respect to the calibration constant of N_2 in the perpendicular-perpendicular configuration.

Appendix B

Molecular constants for Diatomics

For the molecules N_2 and O_2, the constants used to determine the vibrational and rotational energy levels (in the electronic ground state) are obtained from [13]. In Equation 4.5, the higher order contributions of the $\omega_e y_e$ are neglected in the spectral simulations employed in this project. The hydrogen rotational and vibrational constants are taken from [16].

Species	ω_e	$\omega_e x_e$	B_e	α_e	D_e	β_e	H_e
N_2	2358.57	14.324	1.99824	0.0173	$5.76 \cdot 10^{-6}$		
O_2	1580.193	11.981	1.43768	0.0159	$4.84 \cdot 10^{-6}$		
H_2	4401.21	121.33	60.84	2.98	$4.74 \cdot 10^{-2}$	$-2.7 \cdot 10^{-3}$	$52 \cdot 10^{-6}$

Table B.1: Constants of diatomic molecules. All constants are in wavenumbers [cm^{-1}]

The polarizability constants as provided by Sepman et al. in [53] are used for the Placzek approximation of the differential scattering cross-sections expressed in Equations (4.17) and (4.18). The parity of the rotational quantum number determines the effective spin degeneracies, which are calculated from Hanson et al. [62].

Species	g_{nuc} (J_{odd})	g_{nuc} (J_{even})	α_0^2	γ_0^2	$\frac{h}{8\pi\mu v_k}\alpha'$	$\frac{h}{8\pi\mu v_k}\alpha'$
N_2	3	6	$3.13 \cdot 10^{-48}$	$0.509 \cdot 10^{-48}$	$3.09 \cdot 10^{-51}$	$4.20 \cdot 10^{-51}$
O_2	1	0	$2.59 \cdot 10^{-48}$	$1.170 \cdot 10^{-48}$	$2.99 \cdot 10^{-51}$	$9.00 \cdot 10^{-51}$
H_2	3	1	$0.677 \cdot 10^{-48}$	$0.096 \cdot 10^{-48}$	$13.0 \cdot 10^{-51}$	$10.1 \cdot 10^{-51}$

Table B.2: Nuclear degeneracies and polarizability constants. The polarizability constants are in wavenumbers to the sixth power [cm^6]

Appendix C

Error Analysis

In this appendix, the estimation of the random errors in the temperature and molar fraction determinations is discussed and the random errors in the evaluation of the calibration constants are given.

The random errors in the temperature determination are assumed to be entirely determined by the temperatures obtained from Monte-Carlo simulations described in section 6.3. This assumption is used because almost all the Raman spectra measured in this project roughly had a normally distributed noise. Hence, the mathematical expression of the random error in the temperature results is given in Kelvin(K) as:

$$\Delta T(T) \approx \pm \sigma_{\text{Monte-Carlo}}(T) \tag{C.1}$$

where $\sigma_{\text{Monte-Carlo}}(T)$ denotes the standard deviation of the Monte-Carlo simulated temperature. A similar assumption is used for the random error in the molar fraction determined but with additional error components. Since the temperature and calibration results are used to evaluate the molar fractions, their random errors are contributors to the overall error in the molar fraction determination. Thus, the total error in the molar fraction results is a combination of the error associated with their evaluation and the errors in the temperature and calibration results, which is expressed in the equation below:

$$\Delta X(X,T) \approx \pm \left[\sigma_{\text{Monte-Carlo}}(X) + \left(\frac{\Delta T(T)}{T} + \frac{\Delta C}{C} \right) \cdot X \right] \tag{C.2}$$

in which $\sigma_{\text{Monte-Carlo}}(X)$ denotes the standard deviation of the Monte-Carlo simulated molar fractions and ΔC is the error in the calibration constants. Similar to the error estimation of the temperature results, the random errors in the calibration constants determination are approximately equal to the standard deviation of its Monte-Carlo simulated molar fractions. These errors are listed in the table below.

Species	$\Delta C(\perp\perp - \parallel \perp)$
N_2	± 0.0101
O_2	± 0.0095
H_2	± 0.0101
H_2O	$\pm 3.0746 \cdot 10^{-4}$

Table C.1: Errors in calibration constants.

The random errors on the evaluation of the ammonia molar fractions are neglected since they are averaged out during the integration of signals of the Raman spectra of ammonia, which is used in Equation (4.29).

Appendix D

MATLAB code

```
clearvars; close all; clc
%
    ------------------------------------------------------------------------

% Script used to calculate the voigt parameters, temperature and
% concentrations.
% Determine least square fit by optimizing the concentration of the
    species
% and comparing the intensity plot with those of the experiments
% Function fmincon is used to determine the minimum of the least
    square
% https://se.mathworks.com/help/optim/ug/fmincon.html
% fmincon is used instead of lsqcurvefit because equalities and
% inequalities need to be passed for the concentrations.
% Author: Conrad Hessels                              c.j.m.hessels@
    tue.nl
% modified by raheem
%
    ------------------------------------------------------------------------

date='20221012\'; %date of the height calibration
try addpath('Functions'); catch; errordlg('Matlab could not add
    Function folder'); end

%% Optimisation Options of the fminconc function
% http://se.mathworks.com/help/optim/ug/fmincon.html#
    inputarg_options
options = optimoptions('fmincon','Algorithm','interior-point',...
                                 'ConstraintTolerance',1e-1,...
                                 'Diagnostics','off',...
                                 'DiffMaxChange',Inf,...
                                 'DiffMinChange',0,...
                                 'Display','iter-detailed',...
                                 'FunValCheck','off',...
                                 'MaxFunctionEvaluations',3000,...
                                 'MaxIterations',1000,...
                                 'OutputFcn',[],...
                                 'PlotFcn',[],...
                                 'StepTolerance',1e-13);%%
    Optimisation Parameters
% To give extra inputs into a function you want to optimise, you
    can create
```

```
% an anonymous function in the following form:
% http://se.mathworks.com/help/optim/ug/passing-extra-parameters.html

ipix = 1;      % lowest valued vertical pixel to contain results
fpix = 1024;     % highest valued vertical pixel to contain results
bin = 10;       % amount of rows to bin

[image,wavelengthdata,ngrooves] = loadexperiment(ipix,fpix,bin,'true','true','hampel');     % loadexperment is a pre-processing script, that opens a file selector and can perform binning, flatfield correction, background removal and filtering.

spec = {'H2'}; % Choose which species you want to simulate/fit. spec must be a cell array containing strings
X    = 1;% Molar fractions (needs to be 1 for temperature determination)
polarisation = 'experiment';% Polarisation (choose: 'experiment', 'parallelperpendicular' or 'perpendicularperpendicular')
%experiment= perpendicularperpendicular - parallelperpendicular
instrum = 'gaussian';%%'voigt1';%%'voigt2';% ;%chose the instumental broadening profile

% Crop image to selected regions only (can improve simulation speed as well
% as least square fitting procedure
if strcmp(spec,'H2O')
i1 = find(wavelengthdata > 645,1,'first');
i2 = find(wavelengthdata < 655,1,'last');
image = image(:,i1:i2,:);                       %H2O
wavelengthdata = wavelengthdata(i1:i2);
elseif strcmp(spec,'N2')
i1 = find(wavelengthdata > 596,1,'first');
i2 = find(wavelengthdata < 602,1,'last');
image = image(:,i1:i2,:);                       %N2
wavelengthdata = wavelengthdata(i1:i2);
elseif strcmp(spec,'CO')
i1 = find(wavelengthdata > 590,1,'first');
i2 = find(wavelengthdata < 596,1,'last');
image = image(:,i1:i2,:);                       %CO
wavelengthdata = wavelengthdata(i1:i2);
elseif strcmp(spec,'O2')
i1 = find(wavelengthdata > 573,1,'first');
i2 = find(wavelengthdata < 578,1,'last');
image = image(:,i1:i2,:);                       %O2
wavelengthdata = wavelengthdata(i1:i2);
elseif strcmp(spec,'H2')
i1 = find(wavelengthdata > 666,1,'first');
i2 = find(wavelengthdata < 680,1,'last');
image = image(:,i1:i2,:);                       %O2
wavelengthdata = wavelengthdata(i1:i2);
end

%% The bounds of the least-square fitting
```

```
77  var0     = [293 0 0 0];% Starting values (what the different vector
        elements mean can be sound in simulate.m)
78  A        = []; % Function is limited to A*x <= b
79  b        = [];% Function is limited to A*x <= b
80  Aeq      = [];% Equalities ([] if non exist) Aeq*x = beq
81  beq      = [];% Equalities ([] if non exist) Aeq*x = beq
82  lb       = [273 0 0 -0.05];% Lower bound of x (concentration can not
        be smaller than 0)
83  ub       = [2500 10 0 0.05];% Upper bound of x (concentration cannot
        be bigger than 1)
84  nonlcon = [];% Subjects the minimization to the nonlinear
        inequalities c(x) or equalities ceq(x) defined in nonlcon.
85
86  %% Run fmincon (optimisation procedure) it will optimize for 1
        height in steps of 10 each iteration
87  var = zeros(size(Im,1),size(var0,2),1); % Preallocation
88  I = zeros(size(Im));                    % Simulated intensity
        matrix
89  int = zeros(1,size(Im,1));
90
91  tic; wait = waitbar(0,'Please Wait...');
92  for i = 1:size(Im,1)
93  fun = @(var)simulate_temperaturevariableheight(var,spec,X,Im(i,:),
        lambdam,ngrooves,polarisation,instrum,i);  % Create an anonymous
         function that is only dependent on var (so that fmincon will
        only vary that value)
94  [varfit,fval,exitflag,output,lambda,grad,hessian] = fmincon(fun,
        var0,A,b,Aeq,beq,lb,ub,nonlcon,options); % Actual optimisation
        program
95  var0 = varfit;                    % Update the starting values
96  var(i,:) = varfit;                 % Store found values in matrix
97
98  disp(['Fitted temperature = ',num2str(var(i,1)),' Offset in
        intensity = ',num2str(var(i,2))]) % display found value
99
100 [res(i,:),I(i,:),int(i),v0(i,:),phi,x,vimn,vr,Ibg,Iwbg] =
        simulate_temperaturevariableheight(var(i,:),spec,X,Im(i,:),
        lambdam,ngrooves,polarisation,instrum,i);   % Calculate the
        simulated spectrum with the found optimised parameters
101
102 perc = (i/size(Im,1))*100; time = (toc/perc)*(100-perc);         %
        Update the waitbar
103 hour = floor(time/3600); min = floor((time-hour*3600)/60); sec =
        round((time-hour*3600-min*60));
104 waitbar(perc/100,wait,sprintf('Please Wait...  %d%%     %d:%d:%d to
         go',round(perc),hour,min,sec));
105 set(wait,'Name',sprintf('%d%%',round(perc)));
106 end
107 simtijd = toc; toc
108 close(wait);
109 Tave=mean(var(:,1));
110 diff=sum((I-Im),2);
111
112 %% Plotting the calculated temperature along the height
```

```
113 plot(height,var(:,1),'b*')
114 xlabel('Height above the burner [mm]')
115 ylabel('Fitted Temperature [K]')
116
117 %% Plotting the measured and fitted spectra for each height
118 WN = (1/526.5e-7)-((lambdam*1e-7).^-1);
119 figure
120 % Plot examples
121 for i = 1:size(Im,1)
122 plot(WN,Im(i,:)./max(Im(i,int-15:int+15)),WN,I(i,:)./I(i,int(i)));
123 %xlabel('Wavelength [nm]');
124 xlabel('Raman shift [cm^{-1}]');
125 ylabel('Normalised Intensity [a.u.]')
126 title(['Fitted T = ',num2str(round(var(i,1))),'K, at ',num2str(
       round(height(i),2)),' mm above the inlet. Press to go to next
       height data....'])
127 legend({'Experiment','Model'})
128 %waitforbuttonpress
129 pause(0.1)
130 end
```